Semi-Analytical Model of Ionization Oscillations in Hall Thrusters

ARCHIVES
MASSACHUSETTS INSTITUTE
OF TECHNOLOLGY
JUN 23 2015
LIBRARIES

By

Jeffrey A. Mockelman

B.S. Aeronautical Engineering
Rensselaer Polytechnic Institute, 2013

SUBMITTED TO THE
DEPARTMENT OF AERONAUTICS AND ASTRONAUTICS
IN PARTIAL FULFILLMENT OF THE REQUIREMENTS OF THE DEGREE OF

MASTER OF SCIENCE IN AERONAUTICS AND ASTRONAUTICS

AT THE

MASSACHUSETTS INSTITUTE OF TECHNOLOGY

JUNE 2015

© 2015 Massachusetts Institute of Technology, All rights reserved

Signature redacted

Author ....
Department of Aeronautics and Astronautics
May 21, 2015

Signature redacted

Certified by ....
Manuel Martinez-Sanchez
Professor
Thesis Supervisor

Signature redacted

Accepted by ....
Paulo C. Lozano
Associate Professor of Aeronautics and Astronautics
Chair, Graduate Program Committee

Semi-Analytical Model of Ionization Oscillations in Hall Thrusters

By

Jeffrey A. Mockelman

Submitted to the Department of Aeronautics and Astronautics
On May 21, 2015, in partial fulfillment of the
requirements for the degree of
Master of Science in Aeronautics and Astronautics

Abstract

This thesis presents efforts to better understand the breathing-mode oscillation within Hall thrusters. These oscillations have been present and accepted within Hall thrusters for decades, but recent interest in the oscillation has occurred partly due to a possible connection between wall erosion and the oscillations. The first part of this thesis details a steady model of the ionization region in a Hall thruster that finds existence criteria for the steady solution under the hypothesis that the steady limits match the smooth sonic passage limits. Operation outside these limits would correspond to unsteady behavior which could result in either a periodic oscillatory behavior or plume extinguishment. To distinguish between periodic behavior and thruster extinguishment, an unsteady model of the ionization region is developed, but this model falls short of its goal. The transient model, however, is still useful for observation of the periodic nature of an oscillating Hall thruster. Next, an anode depletion model for Hall thrusters is formulated. This model explores one of the causes of thruster extinguishment, when the plasma cannot reach the anode. Finally, a new method for performing Boron Nitride erosion measurements is discussed and preliminary results are presented. This method imbeds Lithium ions into Boron Nitride. The depth of the Lithium can be measured before and after erosion or deposition to give a net erosion or accumulation measurement.

Thesis Supervisor: Manuel Martínez-Sánchez
Title: Professor

Acknowledgments

First I give my thanks to my advisor, Professor Martínez-Sánchez, for all his help, knowledge, assistance, and for making these 2 years very enjoyable. This thesis would not exist without him and the many other people at SPL and the Aero-Astro department. First, Louis Boulanger, who welcomed me to the lab, taught me how to use Astrovac, helped me learn the many concepts in electric propulsion, and continued answering my questions even after he graduated and moved back to France; Tom Coles, who always provided assistance on SPL's computing cluster; Professor Lozano, who offered his expertise to help keep Astrovac running; Todd Billings, who helped me out in the machine shop; and Graham Wright and Spenser Guerin who both took care of the nuclear physics side of the Boron Nitride depth marker experiments. A special thanks to Ewan Kay for helping with experiments and for having a great attention to detail, catching some things that I would have missed. Thanks to everyone at SPL for the two great years we had together.

Finally, I would like to express a special thanks to my parents Guy and Ernene Mockelman for all the support they have given me my whole life and for always pushing me to achieve more. Another special thanks to Hannah Sheldon for all the support she has given me over the last several years.

This material is based upon work supported by the National Science Foundation under Grant No. 1122374. Any opinion, findings, and conclusions or recommendations expressed in this material are those of the author and do not necessarily reflect the views of the National Science Foundation.

Table of Contents

1. Introduction 15
    1.1. Motivation 16
    1.2. Contributions and Thesis Overview 17
2. Background 19
    2.1. Electric Propulsion 19
        2.1.1. Ion Thruster 21
        2.1.2. Hall Thruster 22
    2.2. Plasma Physics 24
        2.2.1. Kinetic Theory and the Boltzmann Equation 24
        2.2.2. Plasma Fluid Equations 25
        2.2.3. 1-D Plasma Fluid Equations 27
        2.2.4. Electron Cross-Field Diffusion 28
        2.2.5. Plasma Wall Sheath 29
3. Steady Model of the Ionization Region 33
    3.1. Derivation 41
        3.1.1. General Approach 41
        3.1.2. Normalization 43
        3.1.3. Steady Model Derivation 46
    3.2. Smooth Sonic Passage 48
    3.3. Existence Conditions 52

3.4. Numerical Example 55

3.5. Steady State Results – Data Comparison 57

3.5.1. SPT-100 with Varying Discharge Potential 58

3.5.2. SPT-100 with Varying Magnetic Field Strength 61

3.5.3. TAL with Varying Magnetic Field Strength 62

3.6. Steady State Model Discussion 63

4. Transient Model of the Ionization Region 65

4.1. Plasma Expansion Phase 66

4.1.1. Solution for the Expanding Plasmoid 66

4.1.2. Neutral Re-fill Profile During Early Ionization 72

4.1.3. Sample Calculations 75

4.2. Rapid Ionization Phase 78

4.3. Selection of Parameters 79

4.3.1. Choice of $\boldsymbol{b10}$ 80

4.3.2. Choice of $\boldsymbol{t}*$, $\boldsymbol{\chi 0}$ and w 80

4.3.3. Choice of $\boldsymbol{\zeta a}$ 81

4.4. Solution Method 81

4.5. Example of Transient Model Application 84

4.6. Transient Model Discussion 89

5. Anode Depletion Model 91

5.1. Simple Diffusion Model 92

5.2. Diffusion Region Model 93

6. Boron Nitride Depth Markers 97

6.1. Background 97

6.2. Sample Testing 98

6.3. Results 99

7. Recommendations for Future Work 105
    7.1. Temperature Model 105
    7.2. Conceptual Difficulties of the Transient Model 105
    7.3. Thruster Controller 106

List of Figures

Figure 2-1: Ion thruster schematic 21

Figure 2-2: Hall thruster schematic 22

Figure 3-1: The neutral-refilling phase of a predator-prey oscillation 35

Figure 3-2: The transition to the ionization phase 37

Figure 3-3: The peak ionization phase. 39

Figure 3-4: Isocline of Eq. 3-37 near (0,0). Isocline corresponds to $\rho = 2,\ \chi = 1.2245$, and $\delta = \infty$. 48

Figure 3-5: Isocline of Eq. 3-37 with the trajectory from the upper γs to (0,0) in thick black. The light green are approximate lines of constant slope for slopes of zero and infinity. Isocline corresponds to $\rho = 2,\ \chi = 1.2245$, and $\delta = \infty$ (no wall losses). The large red dots are the upper and lower γs. A higher resolution isocline map of near a critical point is shown in Figure 3-6. 51

Figure 3-6: Isoclines in the vicinity of the upper γs and a qualitative sketch of the region. Isoclines correspond to $\rho = 2,\ \chi = 1.2245$, and $\delta = \infty$ (no wall losses). 51

Figure 3-7: Max χ existence limits for different δ. 53

Figure 3-8: (a) Smooth Sonic passage existence limits for Eqs. 3-46, 3-48, and 3-49. The vertical solid line is the minimum ρ in Eq. 3-49. The horizontal dashed line is the minimum χ from Eq. 3-49. The curved dashed line is the minimum χ from 3-48. The curved solid line is the maximum χ from Eq. 3-46. (b) Steady Sonic passage existence limits for $\delta = \infty$. The shaded portion is the existence region of smooth sonic passage. 53

Figure 3-9: Smooth Sonic Passage existence region in variables X and Y. 54

Figure 3-10: Critical phase plane trajectory from $\mathrm{M} = 0, \gamma = 0$ to $(\mathrm{M} = 1, \gamma = \gamma s \approx \eta \mathrm{u})$. For $\chi = 1.2245, \rho = 2, \delta = \infty$ case. 55

Figure 3-11: Steady profiles for $\rho = 2, \chi = 1.2245$, and $\delta = \infty$ 56

Figure 3-12: Steady profiles for $\chi = 1.2245$, $\delta = \infty$, and (a) $\rho = 2.5$, (b) $\rho = 3$. 56

Figure 3-13: Assumed relation between discharge voltage and electron temperature in the ionization region of the SPT-100. 58

Figure 3-14: Discharge current and oscillation amplitude vs. discharge potential for SPT-100 from Gascon et al. $\mathrm{ma} = 5\ \mathrm{mg/s}$ Xenon. B=200 Gauss^3 59
Figure 3-15: Experimental X and Y over stability limits for SPT-100 with varying discharge voltage 60
Figure 3-16: Experimental X and Y over stability limits for SPT-100 with varying discharge voltage, zoomed in. This region is for the highest voltages. 60
Figure 3-17: Discharge current and oscillation amplitude vs. coil current for SPT-100 from Gascon et al. $\mathrm{ma} = 5\ \mathrm{mg/s}$ Xenon V = 300 V^3. 61
Figure 3-18: Experimental X and Y over stability limits for SPT-100 with varying magnetic field 62
Figure 3-19: Experimental X and Y over stability limits for a TAL with varying magnetic field 63
Figure 4-1: Variation of $\mathrm{b1}$ for various anode-ionization layer distances, $\mathrm{b10} = 1$ 71
Figure 4-2: The un-depleted neutral profiles at various times 74
Figure 4-3: Calculations for one case. The quantity int(I) is the integral in Eqs. 4-54 to 4-56 and χ is χt', as calculated from Eq. 4-40. 76
Figure 4-4: Ion Mach numbers vs. distance at various times. The top/fastest profile is at t' $= 0$. 77
Figure 4-5: Plasma density vs. distance for various times. t' $= 0$ is the 'curvy' profile in the middle. The density dies off and then builds back up to the highest profile 77
Figure 4-6: Comparison of density profiles after an ionization flash at t* $= 16.2$ and at the initial time (which is also the start of the next period) 79
Figure 4-7: Plasma density profile match for case 1. 88
Figure 4-8: (a) Plasma density profile match for case 5 with χavg predicting a steady solution in steady model limits. (b) Marginally worse profile match for case 5 resulting in a χavg that predicts non-steady in the steady model limits. 88
Figure 6-1: Temperature of Lithium implanted Boron Nitride during exposures 100
Figure 6-2: BHT-200 and rotary stage in Astrovac. No sample mounted 101
Figure 6-3: Lithium implanted Boron Nitride sample mounted 101
Figure 6-4: Lithium implanted Boron Nitride sample close-up 103
Figure 6-5: Lithium implanted Boron Nitride sample (right) in BHT-200 (left) plume 103

List of Tables

Table 4-1: Transient Model Results for the SPT-100 Varying Discharge Potential Cases with $\beta = 16.$ 86

Table 4-2: Transient Model Results for the SPT-100 Varying Magnetic Field Cases with $\beta = 65$ 87

Chapter 1

Introduction

Electric propulsion devices have the ability to obtain very high exhaust speeds, resulting in favorable propellant efficiencies (specific impulse). These devices, however, only produce very low levels of thrust, requiring long firing times to produce a mission's required changes in velocity. When operating, today's electric thrusters slowly cannibalize themselves, resulting in a finite thruster lifetime which translates to a maximum obtainable total velocity change (total impulse) for a given thruster.

Recently, there has been concern of a link between ionization oscillations and enhanced wall erosion in Hall thrusters[1,2]. These ionization oscillations can be observed both experimentally[3,4] and numerically[5] and have been accepted within magnetized thrusters for a few decades. Much work has been accomplished on the study of these oscillations, in particularly the "breathing mode" which has a frequency of 10-30 kHz and is characterized by neutrals refilling an ionization region between bursts of ionization.

Research into the breathing mode had an early, but limited, success with the introduction of a zero dimensional predator-prey style model[6,7]. This model was able to predict the oscillation frequency, but fell short in predicting the onset of instability. Through using particle-in-cell computational methods, the breathing mode has been simulated[8], but the complexity of computing the trajectories of all the super-particles has not allowed a qualitative understanding of what physical properties are driving the oscillation or how to suppress the oscillation. There has been a number of 1D models[9–11] and extensions of the predator prey model[12] constructed. Some of these numerous models have been studied for active control of Hall thruster discharges[13–16]. Lately, the prediction of oscillation onset has been a large interest[17]. A model to predict the threshold conditions for the onset of the breathing mode oscillation and to describe general thruster operation is presented in this thesis.

For Hall thrusters, a kind of electric propulsion device, thruster lifetime is largely limited due to erosion of the discharge chamber walls. In stationary plasma thruster (SPT) type Hall thrusters, the discharge chamber walls are generally made of Boron Nitride, a ceramic. Experimental measurements of the erosion rate is difficult due to the slow rate of erosion. Part of this thesis explains a contribution to the development of a very new way of measuring Boron Nitride which involves implanting a layer of Lithium within Boron Nitride at a depth that can be measured before and after eroding the Boron Nitride.

1.1. Motivation

This research is motivated by an interest in enabling space missions that require higher performance propulsion. Keeping a Hall thruster in a steady operational mode results in an overall better thruster performance and possibly a slower wall erosion rate when compared to an oscillating thruster. This causes a longer thruster lifetime and higher total impulse. The overall better thruster performance results in a higher specific impulse (less propellant needed) and/or higher thrust (shorter firing time needed).

A typical Hall thruster currently has a lifetime of to over 10,000 hours, depending on size and design. NASA's NEXT thruster, the state-of-the-art ion thruster, has a lifetime of over 5.5 years (48,212+ hours). Due to the physics involved in ion and Hall thrusters, a Hall thruster can achieve a thrust density that is much larger than what an ion thruster can achieve. Maximum thruster densities for Hall and ion thrusters are about 8000 N/m^2 and 20 N/m^2, respectively. More typical values of thrust density are 20 and 2 N/m^2, respectively.

Even with higher performing Hall thrusters, it is unlikely that Hall thrusters will replace ion thrusters in the high performance robotic exploration missions to the outer solar system because ion thrusters can achieve a specific impulse of 3,000+ seconds where Hall thrusters can achieve only 1,000 to 2,500+ seconds. Hall thrusters, however, fill a niche that make them highly attractive for missions that optimize at moderate I_{sp}, such as LEO-GEO transfers, station keeping, and lunar trajectory missions. Increasing thruster performance and lifetime, decreases station keeping fuel cost and increases station lifetime. Additionally Hall thrusters beat out ion thrusters if time is an issue (when the area of the thruster is held constant). The order of magnitude increase in thrust density allows Hall thrusters to get to the destination long before an ion thruster arrives, as long as the Hall thruster doesn't surpass its lifetime on the trip.

1.2. Contributions and Thesis Overview

The thesis starts by giving a background on electric propulsion and plasma fluid modeling in Chapter 2. Special attention is given to the 1-D plasma fluid model because it is used extensively in the models this thesis.

The main focus of the worked presented in this thesis is the prediction of threshold conditions for the onset of the breathing mode oscillation, in Chapter 3. This theory, deemed the steady model of the ionization region, starts with the steady 1D fluid equations for a plasma and employs a diffusion treatment for electrons, free-streaming ions, and a constant electron temperature within the ionization region. Justification for the constant electron temperature is provided by the numerical results in T. Matlock's PhD thesis[5] and is explained later. This theory then identifies the existence criteria for a smooth sonic passage, the threshold for steady operation. It was hypothesized that the operation outside the smooth sonic passage criteria results in unsteady operation which could be either periodic oscillations or divergence followed by plume extinguishment. Comparison to experimental results showed the model gives the correct trends. Although uncertainties in the value of the anomalous diffusion parameter (a long-standing problem due to plasma turbulence) and the ionization region's electron temperature prevent knowing the exact placement of the smooth sonic passage limits, the trends uncovered are still valuable.

Chapter 4 presents an unsteady model of the ionization region that assumes a periodic oscillation and two distinct portions of thruster operation within a period, plasma decay with neutral refill and an ionization flash. It was hypothesized that if thruster conditions are not in the steady solution regime or the periodic solution regime, the thruster will extinguish. The original intent of this model was to distinguish between periodic behavior and thruster extinguishment when the steady model is not satisfied. Currently, this model requires an exhaustive search of many parameters to determine if there is no periodic solution. So, more work is needed before this model can distinguish between the periodic oscillations and thruster extinguishment. Currently, this model illustrates the dynamics of the strong relaxation oscillations caused under some conditions by the ionization process. With some streamlining, it is hoped that this model will be able to identify conditions under which no periodic solution can be found; in combination with the steady state model that gives bounds for steady operation, this would provide a complete tool for evaluation of ionization instabilities in Hall and related thrusters.

In Chapter 5, a model exploring a Hall thruster anode depletion instability is presented. This model looks into the area between the anode and the ionization region, the diffusion region, and finds limits on the diffusion coefficient imposed by the need for the plasma density to be greater than zero at the entry to the anode sheath.

Chapter 6 explains the author's contribution to a new method for measuring erosion of Boron Nitride. This method implants Lithium into Boron Nitride at a known depth by shooting a mono-energetic Lithium ion beam at the Boron Nitride. Then, by firing a mono-energetic Hydrogen ion beam at the Boron Nitride to produce alpha decay in the Lithium and varying the beam energy, the depth of the Lithium layer can be determined via Rutherford backscattering analysis (RBS) and nuclear reaction analysis (NRA). This step is repeated after eroding the Boron Nitride. The difference in the depth of the Lithium layer gives the net erosion.

Chapter 7, the final chapter, gives recommendations on future work, based upon the conclusions drawn throughout the thesis.

Chapter 2

Background

2.1. Electric Propulsion

In space travel, propulsion is often needed to get to where you want to go or even just to stay in your desired orbit (because Jupiter will push you around). To provide this necessary propulsion, normally mass is ejected out of the spacecraft in order to cause a force in the opposite direction due to conservation of momentum. The reaction to the forces that eject the mass is called the thrust. According to Newton's Second Law, the larger the thrust, the higher the acceleration, resulting in less firing time needed to produce a desired change in velocity (impulse). Since the mass aboard any spacecraft is limited, the amount of mass that must be ejected to produce that thrust is another important metric; this is called the specific impulse, synonymous with fuel efficiency. Eq. 2-1 shows the formula for the specific impulse where $g = 9.81\, m/s^2$, $\dot{m}$ is the rate that mass is ejected from the spacecraft or thruster, and *F* is thrust.

$$I_{sp} = \frac{F}{\dot{m}g} \qquad 2\text{-}1$$

Specific impulse is commonly expressed in seconds. If a thruster were to theoretically create thrust equal to the starting mass of its propellant multiplied by Earth's gravitational acceleration (g), the specific impulse is how many seconds the thruster would be able to fire. As can be seen, more seconds of specific impulse refers to higher fuel efficiency.

Physically, to achieve a higher fuel efficiency, conservation of momentum says the ejected mass just be ejected from the spacecraft at higher velocities. Specific impulse and thrust are related to the exhaust velocity, *c*, as follows. Note that *c* is the average exhaust velocity.

$$I_{sp} = \frac{c}{g} \tag{2-2}$$

$$F = \dot{m}c \tag{2-3}$$

Today, there are two main categories for propulsion; chemical and electric. Chemical propulsion offers high thrust (the Saturn V produced over 34 million Newtons of thrust), but relatively low specific impulse (upwards of 400 to 500 s). Electric propulsion offers high specific impulse (1000 to 5000 s), but only very small values of thrust (much less than 1 N in most cases). Electric propulsion, as the name implies, also requires electricity, giving an additional design consideration. Chemical propulsion produces enough thrust to take spacecraft from Earth's surface and place them in orbit, but it uses a lot of fuel to do so. Electric propulsion is able to use a small amount of fuel and give a spacecraft a large increase in velocity, allowing it to reach the outer solar system, but the thruster must fire for a long time.

The total impulse delivered by a chemical rocket is normally limited by how much fuel it carries. Electric thrusters are instead limited by the lifetime of the thruster. Electric thrusters slowly erode themselves due to ions impacting their walls, causing wall material to sputter and get ejected. This gives a finite thruster lifetime, which gives a finite total impulse an electric thruster can deliver. To achieve a total impulse greater than what a given thruster can provide, a spacecraft must have multiple thrusters. NASA's Dawn spacecraft has 3 ion thrusters but only fires one at a time to achieve its desired total impulse.

There are many types of electric propulsion devices. This section will introduce ion thrusters and Hall thrusters, but the rest of the report will focus on Hall thrusters. For more details on electric propulsion, please see reference 18.

2.1.1. Ion Thruster

Ion thrusters are, perhaps, conceptually the easiest to understand electric thruster besides the resistojet. As can be seen in Figure 2-1, an ion thruster has an internal ionization region, acceleration grids, and an external plasma plume. The internal ionization region operates by voltage difference between an internal anode and an electron emitting cathode. The anode is generally shielded by a magnetic field to increase electron resonance time. For the most part, the internal ionization region can be optimized independently from the rest of the thruster.

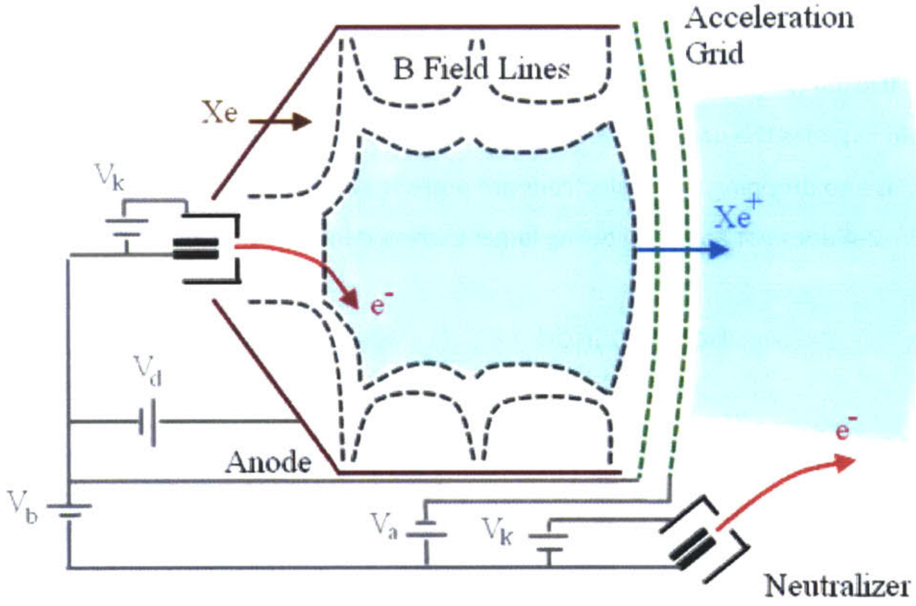

Figure 2-1: Ion thruster schematic

The acceleration grids are a series of grids that accelerate ions into the plume. In the simplest case of two grids, the first grid repels electrons (confining electrons to the internal ionization region), and the second grid accelerates the ions that make their way past the first grid. This causes a nearly monoenergetic beam. The area between the grids is space-charge limited because no/few electrons are present to neutralize the region. This limits the current according to the Child-Langmuir law, Eq. 2-4. The electrostatic pressure is shown in Eq. 2-5 which gives the attainable thrust per unit area in thrusters where the thrust is transferred to the thruster electrostatically. E is the electric field, ε_0 is the permittivity of free space, ϕ_D is the discharge voltage between the two grids, δ is the grid space, m_i is the ion mass, e is the elementary charge, and j_i is the ion current area density.

$$j_i = \frac{4}{9}\varepsilon_0 \sqrt{2\frac{e}{m_i}\frac{\phi_D^{3/2}}{\delta^2}} \qquad 2\text{-}4$$

$$P_E = \frac{1}{2}\varepsilon_0 E^2 \qquad 2\text{-}5$$

2.1.2. Hall Thruster

Hall thrusters are another commonly used electric thruster. As can be seen in Figure 2-2, there is no clear distinction between an ionization region and an acceleration region. This makes the optimization of a Hall thruster more difficult because ionization and acceleration are inherently coupled. Instead of having a grid like ion thrusters, Hall thrusters have a radial magnetic field and an annular channel. This magnetic field impedes the upstream movement of the electrons, creating an area of ionization where the potential is also dropping. Since electrons are present everywhere, there is no space charge limitation (Eq. 2-4 does not apply), allowing larger current densities than an ion thruster.

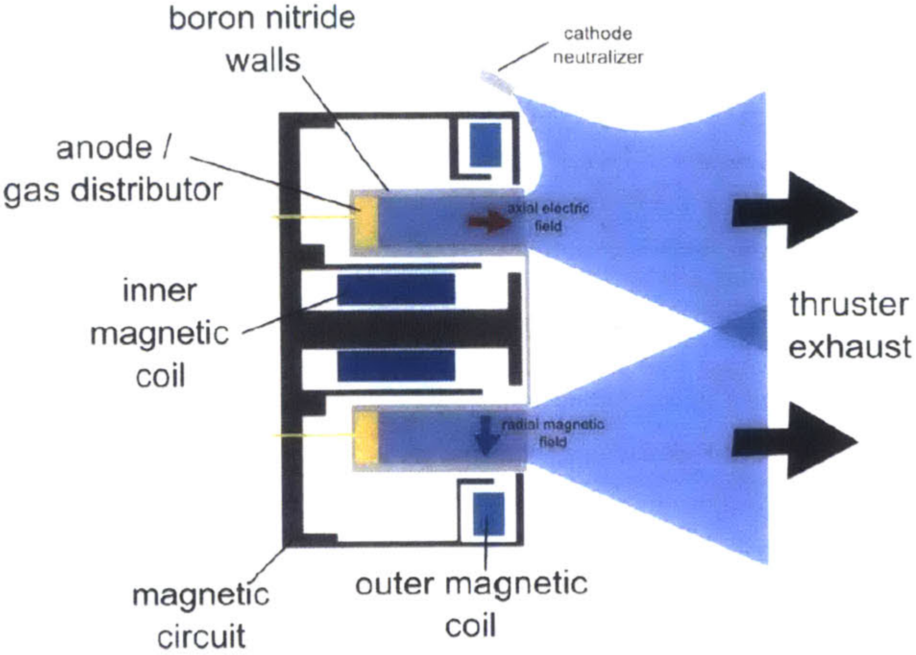
boron nitride walls
cathode neutralizer
anode / gas distributor
axial electric field
inner magnetic coil
thruster exhaust
radial magnetic field
magnetic circuit
outer magnetic coil

Figure 2-2: Hall thruster schematic

Since electrons and ions are both present everywhere, the bulk of the plasma is quasineutral, meaning approximately the same number of ions and electrons are everywhere resulting in no net charge. This means that electric fields don't transmit much force to the thruster. Instead the thrust is transmitted to the structure by the electrons pushing against the magnetic fields, creating a magnetic pressure as shown in Eq. 2-6 where B is the magnetic field strength and μ_0 is the permeability of vacuum. This is why Hall thrusters are correctly designated as electromagnetic thrusters. Under normal circumstances, this allows Hall thrusters to achieve a thrust density about an order of magnitude greater than ion thrusters (although much more is possible).

$$P_B = \frac{1}{2}\mu_0 B^2 \qquad \text{2-6}$$

There are two main types of Hall thrusters, SPT and TAL type thrusters. SPT (Stationary Plasma Thruster) type thrusters have ceramic channel walls and is depicted in Figure 2-2. TAL (Thruster with Anode Layer) type thrusters have channel walls held at the cathode potential to repel the electrons away from the walls to limit losses. TAL thrusters generally have a shorter channel. Both types are prone to numerous oscillations, such as the rotating spoke and breathing mode oscillations. The rotating spoke instability is an ionization wave that travels azimuthally around the annular discharge channel and has been extensively studied[19–21]. The breathing mode is an oscillation where a strong ionization event depletes neutrals from an ionization region, while the neutrals refill, the plasma decays, and eventually another ionization spike depletes the neutrals again. Lately, the breathing mode has received much attention, but what causes the onset of this oscillation is not yet well understood[9,10,22,23]. The bulk of this thesis will explore the onset of the breathing mode.

Xenon is commonly the propellant gas of choice for Hall thrusters (and ion thrusters). Noble gases are preferred because they are chemically inert and monatomic. Of the noble gases, Xenon is preferred because its diameter is so large that the required energy to ionize is relatively low, 12.13 electron Volts (eV). Historically, gasified mercury was used because of its low ionization energy, but it would often coat the outside of the space craft and cause short circuits because of its conductivity.

2.2. Plasma Physics

A plasma is simply a gas where enough particles are ionized that electromagnetic forces cause collective effects to dominate. Plasmas generally maintain a balance between positive and negative charges, resulting in quasineutrality. The section will present some topics in plasma physics that are relevant to the rest of the thesis. Plasmas in this section will be restricted to plasmas consisting of singly charged ions, neutrals, and electrons. For a more complete description of plasma physics, see Ref. 24.

2.2.1. Kinetic Theory and the Boltzmann Equation

Kinetic theory tracks the position and location of many particles. To facilitate this, particles are tracked through 6 dimensional phase space and a distribution function, *f*, gives the density across the 6-D volume. If *f* is known, everything about the gas is known. To translate *f* back into normal 3-D quantities, the three velocity directions must be integrated across. Eq. 2-7 gives this for the density and Eq. 2-8 gives this for any average quantity. d^3w is short for $dw_x dw_y dw_z$ where w is the velocity directions in phase space.

$$n = \int_{-\infty}^{\infty}\int_{-\infty}^{\infty}\int_{-\infty}^{\infty} f \, d^3w \qquad 2\text{-}7$$

$$\langle F(\overline{w})\rangle = \frac{1}{n}\int_{-\infty}^{\infty}\int_{-\infty}^{\infty}\int_{-\infty}^{\infty} F(\overline{w}) f \, d^3w \qquad 2\text{-}8$$

The Boltzmann equation is a 6-D equation for the evolution of a distribution function and can be derived from statistical mechanics. Eq. 2-9 gives the Boltzmann equation. The subscript *s* is for the species of gas and the matching subscripts *i* imply dot products. F_i is any force acting on the gas. For a plasma the force is the Lorentz force, given in Eq. 2-10.

$$\frac{\partial f_s}{\partial t} + w_i \frac{\partial f_s}{\partial x_i} + \frac{F_i}{m_s}\frac{\partial f_s}{\partial w_i} = \left(\frac{df_s}{dt}\right)_{coll} \qquad 2\text{-}9$$

$$F_i = e(\overline{E} + \overline{w} \times \overline{B})_i \qquad 2\text{-}10$$

The right hand side of the Boltzmann equation is the collisional term. This term provides the main complications to the Boltzmann equation. By limiting collisions to binary collisions, Eq. 2-11 gives the collisional term. r is the species that the species s is colliding with. w_1 is the velocity of the particle of species r. The primed distribution functions are the distribution functions in the particles new phase space, to account for reverse collisions. g is the relative velocity between the particles. $d\Omega$ is a range of solid angles that a particle can be deflected into. σ_{rs} is the differential cross section that scatters particles into $d\Omega$.

$$\left(\frac{df_s}{dt}\right)_{coll} = \sum_r \int_{w_1} \int_{\Omega} (f_s' f_{r_1}' - f_s f_{r_1}) g \sigma_{rs} d^3 w_1 d\Omega \qquad 2\text{-}11$$

2.2.2. Plasma Fluid Equations

The Boltzmann equation can be integrated to obtain fluid equations. This is called taking moments in which the Boltzmann equation is multiplied by a general function ϕ and then integrated across d^3w. Different functions ϕ result in different fluid equations. This won't include any sources or sinks, such as ionization, but these can be added in easily later. $\phi = 1$ results in the conservation of mass, given in Eq. 2-12.

$$\frac{\partial n_s}{\partial t} + \nabla \cdot (n_s \overline{u_s}) = 0 \qquad 2\text{-}12$$

$\phi = m_s \overline{w}$ results in the momentum equation. $\overline{\overline{P}}_s'$ is the pressure tensor and will be simplified later for the purpose of this thesis. $\overline{M_{rs}}$ is the momentum transfer from collisions with species r. μ_{rs} is the reduced mass.

$$m_s \frac{\partial n_s \overline{u_s}}{\partial t} + m_s \nabla \cdot (n_s \overline{u_s}\, \overline{u_s}) + \nabla \cdot \overline{\overline{P}}_s' - n_s q_s (\overline{E} + \overline{u_s} \times \overline{B}) = \sum_r \overline{M_{rs}} \qquad 2\text{-}13$$

$$\overline{M_{rs}} = \mu_{rs} \int_{w_1} \int_{w} f_s f_{r_1} g \bar{g} Q_{rs}^{(1)}(g) d^3 w_1 d^3 w \qquad 2\text{-}14$$

Setting ϕ equal to the kinetic energy, $\frac{1}{2} m_s w^2$ results in the energy equation.

$$\frac{\partial}{\partial t}\left[n_s \left(\frac{1}{2} m_s u_s^2 + \frac{3}{2} kT'\right)\right] + \nabla \cdot \left[n_s \bar{u}_s \left(\frac{1}{2} m_s u_s^2 + \frac{3}{2} kT'\right)\right] + \nabla \cdot \left[\bar{q}_s' + \overline{\overline{P}}_s' \bar{u}_s\right] = \bar{E} \cdot \bar{j}_s + \sum_r E_{rs} \qquad 2\text{-}15$$

$$E_{rs} = \mu_{rs} \int_{w_1} \int_{w} f_s f_{r_1} g \bar{G} \cdot \bar{g} Q_{rs}^{(1)}(g) d^3 w_1 d^3 w \qquad 2\text{-}16$$

By assuming that all collisions are Maxwellian collisions, the collisional operators become manageable. This just assumes that the force distribution around a charge is $F \approx q/r^5$. This results in the collision frequency, $\nu_{sr} = n_r g Q^*_{rs}(g)$, being constant, giving:

$$\overline{M_{rs}} = \mu_{rs} n_s \nu_{sr} (\bar{u}_r - \bar{u}_s) \tag{2-17}$$

$$E'_{rs} = E_{rs} - \bar{u}_s \cdot \overline{M_{rs}} = \frac{\mu_{rs}}{m_r + m_s} n_s \nu_{sr} [m_r (\bar{u}_r - \bar{u}_s)^2 + 3k(T'_r - T'_s)] \tag{2-18}$$

$$E_{rs} = \mu_{rs} n_s \nu_{sr} \left[\frac{m_r \bar{u}_r + m_s \bar{u}_s}{m_r + m_s} \cdot (\bar{u}_r - \bar{u}_s) + \frac{3k}{m_r + m_s} (T'_r - T'_s) \right] \tag{2-19}$$

These equations are further simplified by considering that the energy transfer between collisions is inefficient due to the large mass disparity, pressure is assumed to be isotropic, ionization is added, ions are considered cold, quasineutrality is imposed, ions are unmagnetized, and electrons are considered much faster than the other species. $\nu_{eT} = (\nu_{en} + \nu_{ei} + \nu_{ion} + \alpha_B \omega_{ce})$. ε_i is the ionization cost and α_i is the excitation losses (2 to 3). The neutral velocity can often be taken as a constant.

$$\frac{\partial n_e}{\partial t} + \nabla \cdot (n_e \overline{u_e}) = \nu_{ion} n_e \tag{2-20}$$

$$\frac{\partial n_e}{\partial t} + \nabla \cdot (n_e \bar{u}_\iota) = \nu_{ion} n_e \tag{2-21}$$

$$\frac{\partial n_n}{\partial t} + \nabla \cdot (n_n \overline{u_n}) = -\nu_{ion} n_e \tag{2-22}$$

$$\frac{\partial m_e n_e \overline{u_e}}{\partial t} + \nabla \cdot (m_e n_e \overline{u_e}\, \overline{u_e}) = -\nabla P_e - e n_e (\bar{E} + \overline{u_e} \times \bar{B}) + m_e n_e \bar{u}_e \nu_{eT} \tag{2-23}$$

$$\frac{\partial m_i n_e \bar{u}_\iota}{\partial t} + \nabla \cdot (m_i n_e \bar{u}_\iota\, \bar{u}_\iota) = e n_e \bar{E} + m_i n_e \nu_{ion} \upsilon_n \tag{2-24}$$

$$\frac{\partial m_n n_n \overline{u_n}}{\partial t} + \nabla \cdot (m_n n_n \overline{u_n}\, \overline{u_n}) = -m_i n_e \nu_{ion} \upsilon_n \tag{2-25}$$

$$\begin{aligned} \frac{\partial}{\partial t} \left[n_e \left(\frac{1}{2} m_e u_e^2 + \frac{3}{2} k T_e \right) \right] + \nabla \cdot \left[n_e \overline{u_e} \left(\frac{1}{2} m_e u_e^2 + \frac{5}{2} k T_e \right) \right] + \nabla \cdot \overline{q_e} \\ = -e n_e u_e \cdot \bar{E} - \nu_{ion} n_e \alpha_i \varepsilon_i \end{aligned} \tag{2-26}$$

2.2.3. 1-D Plasma Fluid Equations

The fluid equations can be radially averaged to create 1-D plasma fluid equations. This is performed in detail in Matlock's PhD thesis[5]. For a straight channel, constant neutral velocity, radial B field, and axial electric field, the results are:

$$\frac{\partial n_e}{\partial t} + \frac{\partial n_e v_{ex}}{\partial x} = \nu_{ion} n_e - \nu_{iw} n_e \tag{2-27}$$

$$\frac{\partial n_e}{\partial t} + \frac{\partial n_e v_{ix}}{\partial x} = \nu_{ion} n_e - \nu_{iw} n_e \tag{2-28}$$

$$\frac{\partial n_n}{\partial t} + v_n \frac{\partial n_n}{\partial x} = -\nu_{ion} n_e + \nu_{iw} n_e \tag{2-29}$$

$$\frac{\partial m_e n_e v_{ex}}{\partial t} + \frac{\partial m_e n_e v_{ex}^2}{\partial x} = -\frac{\partial P_e}{\partial x} - e n_e E_x - m_e n_e \omega_{ce} v_{e\theta} - m_e n_e v_{ex} \nu_e \tag{2-30}$$

$$\frac{\partial m_e n_e v_{e\theta}}{\partial t} + \frac{\partial m_e n_e v_{ex} v_{e\theta}}{\partial x} = m_e n_e \omega_{ce} v_{ex} - m_e n_e v_{e\theta} \nu_e \tag{2-31}$$

$$\frac{\partial m_i n_e v_{ix}}{\partial t} + \nabla \cdot \left(m_i n_e v_{ix}^2\right) = e n_e E_x - m_i n_e v_{ix} \nu_{iw} + m_i n_e \nu_{ion} v_n \tag{2-32}$$

$$\frac{\partial}{\partial t}\left[n_e\left(\frac{1}{2} m_e\left(v_{ex}^2 + v_{e\theta}^2\right) + \frac{3}{2} k T_e\right)\right] + \frac{\partial}{\partial x}\left[n_e v_{ex}\left(\frac{1}{2} m_e\left(v_{ex}^2 + v_{e\theta}^2\right) + \frac{5}{2} k T_e\right)\right] + \frac{\partial q_{ex}}{\partial x} = -e n_e v_{ex} E_x - \nu_{ion} n_e \alpha_i \varepsilon_i - n_e \nu_{ew} \varepsilon_w \tag{2-33}$$

ν_{iw} is the ion collision rate with the walls, ν_{ew} is the electron collision rate with the walls, and ε_w is the energy lost when an electron collides with the walls. $\omega_{ce} = eB/m_e$ is the electron cyclotron frequency. In these equations, electron inertia is often neglected. Other terms in the equations are generally as follows where σ accounts for secondary electron emission at the walls and ε^* is the electron energy corresponding to unity secondary yield of the wall material.

$$\nu_{iw} = \frac{4}{3} \frac{1}{R_{c2} - R_{c1}} \sqrt{\frac{kT_e}{m_i}} \tag{2-34}$$

$$\nu_{ew} = \frac{\nu_{iw}}{1 - \sigma} \tag{2-35}$$

$$\varepsilon_w = 2kT_e + \frac{1}{2}m_e\left(v_{ex}^2 + v_{e\theta}^2\right) + (1-\sigma)kT_e \ln\left[(1-\sigma)\sqrt{\frac{m_i}{2\pi m_e}}\right] \qquad 2\text{-}36$$

$$\sigma = \min\left(\frac{2kT_e}{\varepsilon^*},\ 0.986\right) \qquad 2\text{-}37$$

For the rate of ionization, $v_{ion} = R_i n_n$ is commonly used where R_i is as follows. $\bar{c_e} = \sqrt{\frac{8kT_e}{\pi m_e}}$, σ_0 is about $3.6 \times 10^{-20}\ m^2$ for Xenon, and $E_i$is about $12.13\ eV$ for Xenon.

$$R_i \approx \sigma_0 \bar{c_e}\left(1 + 2\frac{kT_e}{E_i}\right)\exp\left(\frac{E_i}{kT_e}\right) \qquad 2\text{-}38$$

2.2.4. Electron Cross-Field Diffusion

The models in this thesis commonly assume diffusive electrons. This section will derive the diffusive electron equation. The derivation starts with the electron momentum equation split into the x and θ components, neglecting inertia and only considering a radial magnetic field.

$$-eE_x - \frac{1}{n_e}\frac{dP_e}{dx} - ev_{e\theta}B - m_e v_{ex}\nu_e = 0 \qquad 2\text{-}39$$

$$ev_{ex}B - m_e v_{e\theta}\nu_e = 0 \qquad 2\text{-}40$$

Eq. 2-40 solves to give

$$v_{e\theta} = \frac{eB}{m_e \nu_e}v_{ex} = \frac{\omega_{ce}}{\nu_e}v_{ex} = \beta v_{ex} \qquad 2\text{-}41$$

where $\beta = \omega_{ce}/\nu_e$ is the Hall parameter. Generally, an effective Hall parameter will have to be used to take into account the anomalous diffusion from plasma turbulence. The effective Hall parameter can range from 16 to 100.

Eq. 2-41 is now plugged into Eq. 2-39 and rearranged to give:

$$m_e\left(\frac{\omega_{ce}^2+\nu_e^2}{\nu_e}\right)v_{ex}=-eE_x-\frac{1}{n_e}\frac{dP_e}{dx} \qquad 2\text{-}42$$

In Hall thrusters $\omega_{ce} \gg \nu_e$, allowing ν_e^2 to be neglected. This gives the desired equation for diffusive electrons, Eq. 2-43.

$$v_{ex}=-\frac{1}{eB\beta}\left[eE_x+\frac{1}{n_e}\frac{dP_e}{dx}\right] \qquad 2\text{-}43$$

Another interesting result is what diffusive electrons gives for the azimuthal electron velocity. As expected, the θ velocity has a dependence on E/B from the $E \times B$ drift, but also depends on the pressure gradient in the x direction. This is a result of conservation of momentum.

$$v_{e\theta}=-\frac{1}{eB}\left[eE_x+\frac{1}{n_e}\frac{dP_e}{dx}\right] \qquad 2\text{-}44$$

2.2.5. Plasma Wall Sheath

When a plasma is in contact with an insulative wall, a plasma sheath quickly forms against the wall where the potential drops to force an equal number of electrons and ions to reach the wall. In most cases, this sheath is electron repelling. The sheath consists of two parts, the sheath and the pre-sheath. Quasineutrality is preserved in the pre-sheath, but breaks down in the sheath.

In the sheath, the low energy electrons have been repelled, but can still be assumed to have a Maxwellian distribution. The ions in the sheath are in free-fall. This gives the following current densities where n_{ew} is the electron density at the wall and $\bar{c_e}=\sqrt{8kT_e/\pi m_e}$ is mean electron thermal speed.

$$j_i=en_iv_i \qquad j_e=en_{ew}\frac{\bar{c_e}}{4} \qquad 2\text{-}45$$

To find n_{ew} we can derive the Boltzmann equilibrium relation from the electron momentum equation. The 1-D electron momentum equation after neglecting inertia and collisions is:

$$\frac{1}{n_e}\frac{dP_e}{dx}=\frac{d(e\phi)}{dx} \qquad 2\text{-}46$$

$P_e = n_e kT_e$ is the electron pressure. By assuming constant temperature, this integrates to the Boltzmann equilibrium relation, Eq. 2-47 where the potential at infinity is taken to be zero and $n_{e\infty}$ is the far away plasma density.

$$n_{ew} = n_{e\infty} \exp\left(\frac{e\phi_w}{kT_e}\right) \tag{2-47}$$

Entering the sheath, the ions enter at the Bohm velocity, v_B. The easiest way to show this is by adding the ion and electron steady momentum equations and to assume cold ions to get:

$$\frac{dG}{dx} = -F \qquad G = m_i v_i \Gamma_i + \frac{\Gamma_i}{v_i} kT_e \tag{2-48}$$

$\Gamma_i = n_e v_i$ is the ion flux, a constant. As can be seen, G will decrease with respect to x. It actually reaches a minimum value, the Bohm velocity:

$$v_B = \sqrt{\frac{kT_e}{m_i}} \tag{2-49}$$

Following a non-colliding ion through the pre-sheath to the sheath boundary gives the following:

$$e\phi_{ps} = -\frac{1}{2} m_i v_B^2 = -\frac{1}{2} kT_e \tag{2-50}$$

To find the ion density at the pre-sheath boundary, quasineutrality is used to equate the ion density to the electron density, then the Boltzmann equilibrium relation is used. This gives:

$$n_{i,ps} \approx n_{e\infty} \exp\left(\frac{e\phi_{ps}}{kT_e}\right) = n_{e\infty} \exp\left(-\frac{1}{2}\right) \tag{2-51}$$

By equating the current densities and solving for the wall potential difference, Eq. 2-52 is found which is commonly simplified to Eq. 2-53.

$$-\phi_w = \frac{kT_e}{e}\left[\frac{1}{2} + \ln\sqrt{\frac{m_i}{2\pi m_e}}\right] \qquad 2\text{-}52$$

$$-\phi_w \approx \frac{kT_e}{e}\ln\sqrt{\frac{m_i}{m_e}} \qquad 2\text{-}53$$

An important result is the ion flux to the wall.

$$\Gamma_{iw} = n_{e\infty}\exp\left(-\frac{1}{2}\right)\sqrt{\frac{kT_e}{m_i}} \qquad 2\text{-}54$$

Chapter 3

Steady Model of the Ionization Region

This chapter presents a model to predict the threshold conditions for the onset of the breathing mode oscillation. This model is deemed the steady model because it assumes a steady state solution and finds the limits of existence of that solution. The limits will be seen to correspond to those for existence of a smooth sonic passage at the end of the ionization region. When the steady limits are not satisfied, the thruster will operate in an unsteady mode, either periodic oscillations or thruster extinguishment. This theory starts with the steady 1-D fluid equations for a plasma and employs a diffusion treatment for electrons, free-streaming ions, and a constant electron temperature within the ionization region. Justification for the constant electron temperature is provided by the numerical results in T. Matlock's PhD thesis[5], using a 1-D plus time fluid model, similar to Barral and Ahedo's model[9–11]. Constant temperature is also supported physically by the self-correcting nature of the energy balance in regions with a high endothermic rate of some process, ionization in this case. Other examples include the boiling transition of a liquid or the dissociation region of a molecular gas.

The conditions modeled by Matlock in his 1D unsteady computations were 7 mg/s, 180 Volt discharge potential, 0.02 Tesla maximum magnetic field, and $1.9\text{x}10^{19}$ m^{-3} neutral density at the anode. We present here a discussion of Matlock's results because they provide useful guidance for the development of our own simplified model. Figure 3-1 through Figure 3-3 (Taylor's Figures 5 through 7) show the initial phase of development of various quantities, starting at the peak of one of the strong ionization bursts. Several observations are important for this phase:

- The plasma density decays in this phase, as the plasmoid generated in the last ionization burst expands and convects downstream.
- As shown by the plot of ionization frequency, the ionization zone remains more or less in place, between about x = 5 and 20 mm from the origin.
- The electric field has also a roughly stationary structure, being strongest between 15 and 25 mm, although it does vary in strength over time; it weakens during the phase when the neutrals are re-filling the depleted zone.
- The neutrals, that were quickly depleted during the burst, then re-fill as a front that advances at $v_n = 200$ m/s. This feature shows that ionization is not important during this phase. The front thickness is about 5 mm, smaller than the ionization zone width.
- The electron temperature peaks downstream (cathode side) of this advancing front. It remains fairly constant in the ionization band, around $x = 12$ mm.

The transition to the ionization phase is displayed in Figure 3-2. Here we notice:

- The ionization band and the electric field band remain anchored in the same locations as in the re-fill phase. The electric field **E** remains steady.
- The advance of the neutral front is arrested by the onset of ionization, at about $t = 415$ μs, after which n_n begins to decay throughout the ionization zone. At the time when neutrals begin to deplete, their advancing front has already covered most of the ionization layer.
- Simultaneous with this decay, n_e starts to climb rapidly in the ionization zone. The enhanced ion density is shown to be convected rapidly downstream, at what appears to be several km/s. The time constant for the rise of n_e and decay of n_n is about 20 μs, compared to about 90 μs for the re-fill phase.
- T_e remains about constant, only rising from 7 to 9 eV in the ionization layer during the ionization burst.

The peak of the ionization phase is more clearly shown in Figure 3-3. Here, the localization of the electric field and the ionization frequency is confirmed again, and we see the dramatic collapse of n_n and the corresponding rise of n_e. The temperature in the ionization band still remains fairly constant.

It is clear from these results that the two phases (plasma expansion with neutral re-fill and rapid ionization) can be modeled separately, with attention paid to the transition between both.

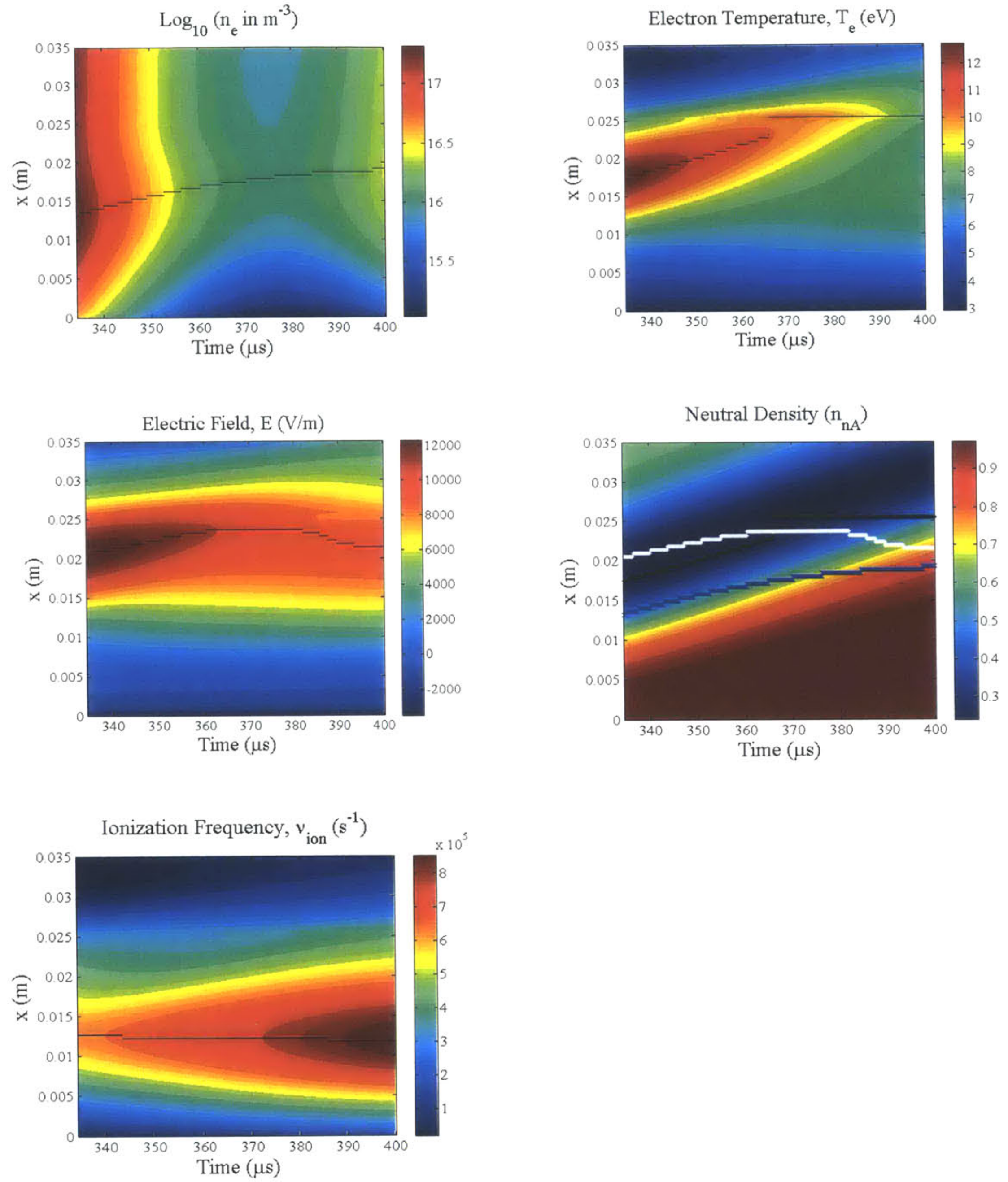

Log_{10} (n_e in m^{-3})

Electron Temperature, T_e (eV)

Electric Field, E (V/m)

Neutral Density (n_{nA})

Ionization Frequency, ν_{ion} (s^{-1})

Figure 3-1: The neutral-refilling phase of a predator-prey oscillation.

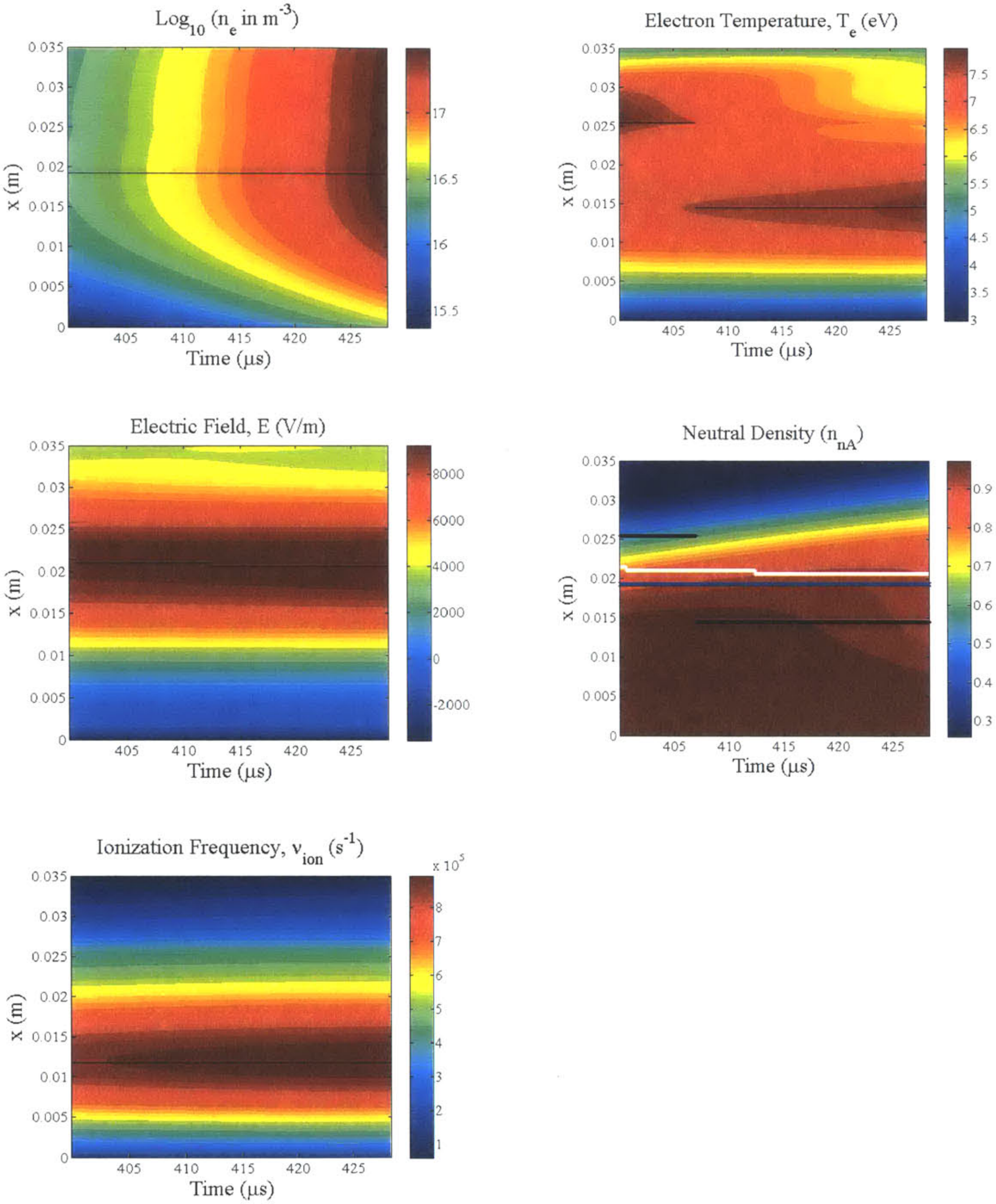

Figure 3-2: The transition to the ionization phase.

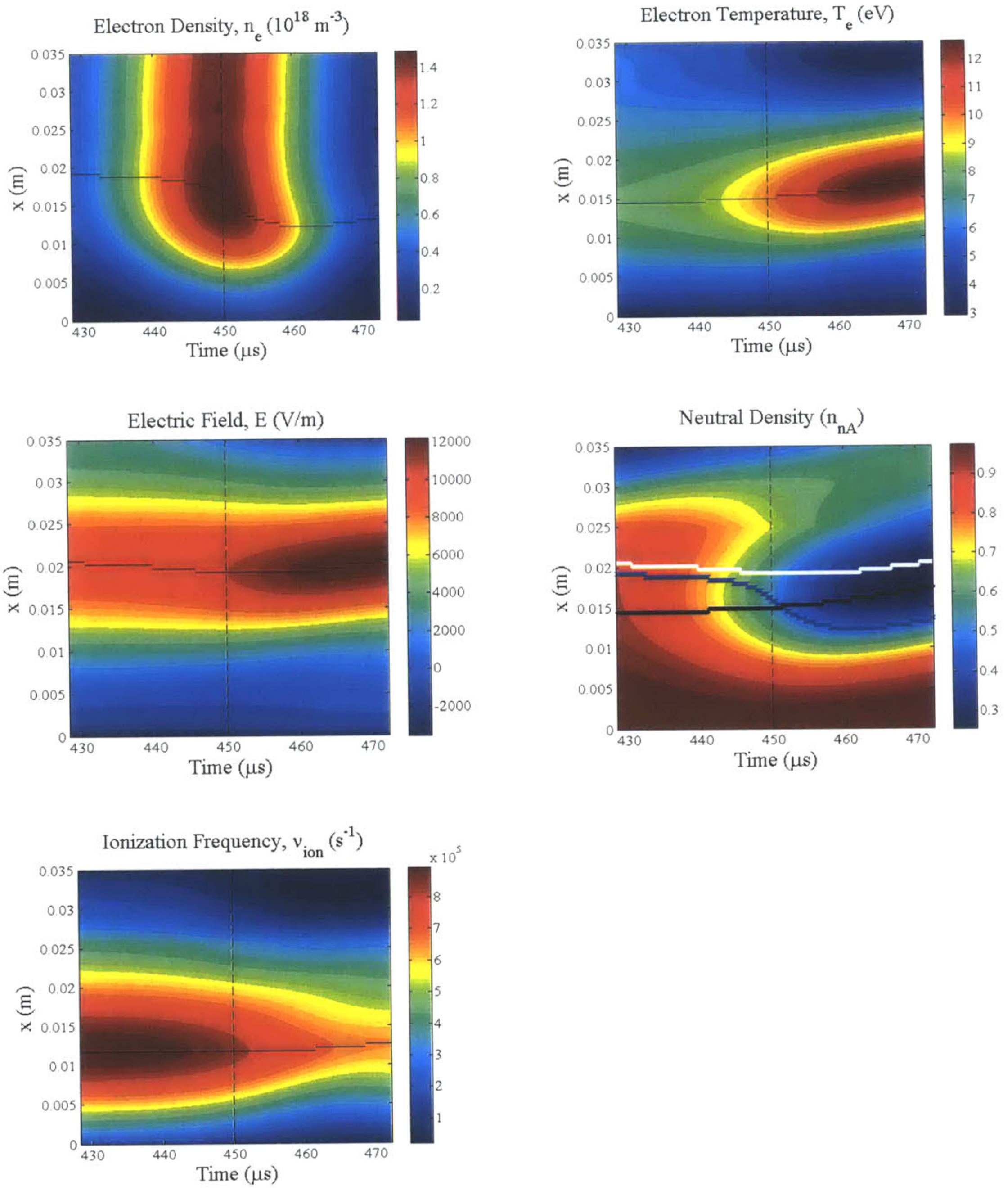

Electron Density, n_e (10^{18} m^{-3})

Electron Temperature, T_e (eV)

Electric Field, E (V/m)

Neutral Density (n_{nA})

Ionization Frequency, ν_{ion} (s^{-1})

Figure 3-3: The peak ionization phase.

3.1. Derivation

3.1.1. General Approach

We start with the fluid equations for a one-dimensional, quasi-neutral plasma flow through an annular chamber in a crossed magnetic field, as is typical for Hall thrusters. These equations are derived from the more general 3-dimensional formulation. Only singly charged, cold, collisionless, non-magnetized ions are considered and the neutrals are assumed to have constant velocity of the order of their speed of sound and thermalized with the wall. The electron energy equation will be obviated by adopting the isothermal approximation, which appears justifiable for the ionization layer on the basis of the numerical results of Matlock, as well as the physical arguments advanced above. For now, the temporal derivative is left in the equations, but will be removed for the steady model after normalization. The rate that ions collide with the walls is ν_{iw} and the total electron collision rate is ν_e. x is the axial direction.

$$\frac{\partial n_e}{\partial t}+\frac{\partial(n_e v_{ex})}{\partial x}=R_i n_n n_e-n_e\nu_{iw} \qquad \text{3-1A}$$

$$\frac{\partial n_e}{\partial t}+\frac{\partial(n_e v_{ix})}{\partial x}=R_i n_n n_e-n_e\nu_{iw} \qquad \text{3-1B}$$

$$\frac{\partial n_n}{\partial t}+\frac{\partial(n_n v_{nx})}{\partial x}=-R_i n_n n_e+n_e\nu_{iw} \qquad \text{3-1C}$$

$$\frac{\partial(m_e n_e v_{ex})}{\partial t}+\frac{\partial(m_e n_e v_{ex}^2)}{\partial x}=-en_eE_x-en_ev_{e\theta}B_r-m_en_e\nu_e v_{ex} \qquad \text{3-1D}$$

$$\frac{\partial(m_i v_{ix})}{\partial t}+v_{ix}\frac{\partial(m_i v_{ix})}{\partial x}=eE_x \qquad \text{3-1E}$$

The notation will be simplified so all velocities are taken to be in the axial direction

The electrons are assumed to be highly magnetized, with an axial (cross-field) mobility $\mu_e=1/(\beta B)$, where β is the effective Hall parameter, taking into account anomalous diffusion from plasma turbulence, of order 16-100, taken as a constant. B is the magnetic field strength. The axial diffusivity is then $D_e = \frac{kT_e}{e\beta B}$, and for an axial electric field E_x, their axial mean velocity is given by equation 3-2, replacing 3-1D.

$$v_e = -\frac{1}{\beta B}\left(E_x + \frac{kT_e}{e}\frac{d\ln n_e}{dz}\right) \qquad 3\text{-}2$$

For a simplified representation, the dynamic effects of $\frac{\partial\phi}{\partial t}$ are neglected in equation 3-1E. This assumption will need to be justified a-posteriori. The maximum potential is taken to be zero. This simplifies the ion momentum equation to the form:

$$\frac{d}{dx}\left(\frac{1}{2}m_i v_i^2\right) = \frac{d}{dx}(-e\phi) \qquad \frac{1}{2}m_i v_i^2 = -e\phi \qquad 3\text{-}3$$

The ion-wall collisional term is taken from the simplified sheath-pre-sheath model. Ions are assumed to enter the wall sheath at the Bohm velocity and the losses to the wall are averaged over the volume, neglecting the pre-sheath, $n_e v_B 2\pi(r_1 + r_2)/\pi(r_2^2 - r_1^2)$. Calling $h = r_2 - r_1$, the channel width, this loss rate reduces to $2n_e v_B/h$. Of course, for every ion lost to the insulating wall, an electron is also lost, and a new neutral atom is returned to the plasma. This modifies the continuity equations, 3-1 A-C, to the following.

$$\frac{\partial n_e}{\partial t} + \frac{\partial(n_e v_e)}{\partial x} = R_i n_n n_e - 2\frac{v_B}{h}n_e \qquad 3\text{-}4A$$

$$\frac{\partial n_e}{\partial t} + \frac{\partial(n_e v_i)}{\partial x} = R_i n_n n_e - 2\frac{v_B}{h}n_e \qquad 3\text{-}4B$$

$$\frac{\partial n_n}{\partial t} + \frac{\partial(n_n v_n)}{\partial x} = -R_i n_n n_e + 2\frac{v_B}{h}n_e \qquad 3\text{-}4C$$

Current conservation follows, where $j = I_a/A$ is the current density.

$$n_e(v_i - v_e) = \frac{j(t)}{e} \qquad 3\text{-}5$$

Similarly, the atom conservation law:

$$\frac{\partial}{\partial t}(n_e + n_n) + \frac{\partial}{\partial x}(n_e v_i + n_n v_n) = 0 \qquad 3\text{-}6$$

The ionization rate coefficient, R_i, depends only on the electron temperature allowing R_i to be taken as a constant as well. For moderate temperature levels, R_i can be represented as:

$$R_i = \sigma_0 \bar{c}_e \left(1 + 2\frac{kT_e}{E_i}\right) e^{-\frac{E_i}{kT_e}} \qquad \text{3-7}$$

where $\bar{c}_e = \sqrt{\frac{8}{\pi}\frac{kT_e}{m_e}}$ and E_i is the ionization potential of the gas. The cross-section σ_0 is of the order of $3.6 \times 10^{-20}\ m^2$ for Xenon.

3.1.2. Normalization

The natural unit for particle densities is Γ_{m}/v_n, where Γ_m is the heavy particle flux, defined be $\Gamma_m = \frac{\dot{m}}{m_i A} = n_{na} v_n$, taken as a prescribed quantity. n_{na} is the neutral density at the anode. We define non-dimensional densities as

$$N_e = \frac{n_e v_B}{\Gamma_m} \qquad N_n = \frac{n_n v_B}{\Gamma_m} \qquad \text{3-8}$$

The unit for velocity is the Bohm velocity (isothermal plasma speed of sound), $v_B = \sqrt{kT_e/m_i}$, and we therefore introduce an "ion Mach number," "electron quasi Mach number," and "neutral quasi Mach number."

$$M = \frac{v_i}{v_B} \qquad M_e = \frac{v_e}{v_B} \qquad M_n = \frac{v_n}{v_B} \qquad \text{3-9}$$

Notice that M_n is not a true Mach number for the neutrals, and is in fact a small number, of the order $\sqrt{T_n/T_e} \approx 0.07$. Notice also that the anode limit of N_n is $N_{na} = 1/M_n$, and is therefore relatively large.

A useful alternative to N_e as a dependent variable is the non-dimensional ion flux

$$\gamma = MN_e = \frac{v_i}{v_B}\frac{n_e v_B}{\Gamma_m} = \frac{n_e v_i}{\Gamma_m} \qquad \text{3-10}$$

The logical length scale is the ratio of electron diffusivity to Bohm velocity, which we use to normalize axial distances:

$$l_{diff} = \frac{kT_e}{\beta B e v_B} \qquad \zeta = \frac{x}{l_{diff}} \tag{3-11}$$

A second meaningful length scale is that for ionization. Since the ionization frequency per ion is $R_i n_n$, and the typical ion velocity is v_B. This ionization distance is

$$l_{ioniz} = \frac{v_B}{R_i n_{n0}} = \frac{v_B v_n}{R_i \Gamma_m} \tag{3-12}$$

The ratio of these two distances must then be a controlling parameter in this problem:

$$\rho = \frac{l_{diff}}{l_{ioniz}} = \frac{m_i R_i \Gamma_m}{e\beta B v_n} \tag{3-13}$$

This parameter is seen to be proportional to neutral density and an increasing function of electron temperature. For normal conditions, it ranges from about 0.5 to 4.

A second non-dimensional parameter is the ratio of charge to mass fluxes:

$$\chi = \frac{j}{e\Gamma_m} \tag{3-14}$$

Remembering the definitions of "utilization factor", $\eta_u = \frac{I_{Beam}}{(e/m_i)\dot{m}}$ and "current efficiency", $\eta_I = \frac{I_{Beam}}{I_{Anode}}$, it can be seen that $\chi = \eta_u/\eta_I$. For efficient operating conditions, this ratio is typically somewhat greater than unity, such as between 1 and 1.4.

The non-dimensional channel width is taken to be

$$\delta = \frac{1}{2}\frac{h}{l_{diff}} \tag{3-15}$$

Time is non-dimensionalized as follows

$$t' = \frac{v_B}{l_{diff}} t \tag{3-16}$$

The non-dimensionalized electric field and potential are related as follows:

$$\hat{E}_z = \frac{E_x}{\beta B v_B} = -\frac{\partial \Phi}{\partial \zeta} \tag{3-17}$$

After some algebra, we can now write the non-dimensional governing equations as:

$$\frac{\partial N_e}{\partial t'} + \frac{\partial (N_e M_e)}{\partial \zeta} = \rho M_n N_n N_e - \frac{N_e}{\delta} \tag{3-18}$$

$$\frac{\partial N_e}{\partial t'} + \frac{\partial (N_e M)}{\partial \zeta} = \rho M_n N_n N_e - \frac{N_e}{\delta} \tag{3-19}$$

$$\frac{\partial N_n}{\partial t'} + M_n \frac{\partial (N_n)}{\partial \zeta} = -\rho M_n N_n N_e + \frac{N_e}{\delta} \tag{3-20}$$

$$M_e = -\left(\hat{E}_z + \frac{\partial \ln N_e}{\partial \zeta}\right) \tag{3-21}$$

$$\Phi = -\frac{1}{2} M^2 = \frac{e\phi}{T_e} \qquad \hat{E}_z = M \frac{\partial M}{\partial \zeta} \tag{3-22}$$

$$N_e (M - M_e) = \chi(t') \tag{3-23}$$

3.1.3. Steady Model Derivation

At this point, the model will be simplified to look at the steady state by neglecting the temporal derivatives. The steady state equations are as follows. Equation 3-30 comes from steady state atom conservation.

$$\frac{\partial (N_e M_e)}{\partial \zeta} = \rho M_n N_n N_e - \frac{N_e}{\delta} \qquad 3\text{-}24$$

$$\frac{\partial (N_e M)}{\partial \zeta} = \rho M_n N_n N_e - \frac{N_e}{\delta} \qquad 3\text{-}25$$

$$M_n \frac{\partial (N_n)}{\partial \zeta} = -\rho M_n N_n N_e + \frac{N_e}{\delta} \qquad 3\text{-}26$$

$$M_e = -\left(\hat{E}_z + \frac{\partial \ln N_e}{\partial \zeta}\right) \qquad 3\text{-}27$$

$$\hat{E}_z = M \frac{\partial M}{\partial \zeta} \qquad 3\text{-}28$$

$$N_e (M - M_e) = \chi \qquad 3\text{-}29$$

$$N_e M + N_n M_n = 1 \qquad 3\text{-}30$$

We now substitute equation 3-28 into 3-27 and plug the result into 3-29 to obtain one differential equation relating N_e and M:

$$\chi = N_e M + \left(N_e M \frac{\partial M}{\partial \zeta} + \frac{\partial N_e}{\partial \zeta}\right) \qquad 3\text{-}31$$

In addition, we can express N_n in terms of N_e and M from equation 3-30, and substitute into 3-25 to obtain a second differential equation:

$$\frac{\partial (N_e M)}{\partial \zeta} = \rho (1 - N_e M) N_e - \frac{N_e}{\delta} \qquad 3\text{-}32$$

The pair of equations 3-31 and 3-32 are highly non-linear and no analytical solution appears to exist. For numerical integration, the standard preliminary step is to isolate the derivatives in terms of the variables themselves. We omit the algebra and quote the results:

$$(1-M^2)\frac{dM}{d\zeta} = M\left(M-\frac{\chi}{N_e}\right) + \rho(1-N_eM) - \frac{1}{\delta} \tag{3-33}$$

$$(1-M^2)\frac{dN_e}{d\zeta} = -N_e\left(M-\frac{\chi}{N_e}\right) - N_eM\left[\rho(1-N_eM) - \frac{1}{\delta}\right] \tag{3-34}$$

The most important observation here is the presence of the factor $(1-M^2)$ in both equations, indicating the existence of a sonic passage. When this factor crosses through zero, both right hand sides of 3-33 and 3-34 must also cross through zero; in fact, both do if one of them does. It can be shown that this sonic point is also approximately the downstream end of the ionization zone, although this cannot be taken as a literal end, only a strong reduction from its peak.

Now, using the alternative variable $\gamma = MN_e$ and a little manipulation, simpler equations are found.

$$(1-M^2)\frac{dM}{d\zeta} = M^2\left(1-\frac{\chi}{\gamma}\right) + \rho(1-\gamma) - \frac{1}{\delta} \tag{3-35}$$

$$\frac{d\gamma}{d\zeta} = -\frac{\gamma}{M}\left[\rho(1-\gamma) - \frac{1}{\delta}\right] \tag{3-36}$$

If we assume B, β, T_e and other parameters to be independent of *x*, the pair of equations 3-35 and 3-36 contain *x* only as the independent variable, and their ratio will be an autonomous single equation relating M and γ:

$$\frac{d\gamma}{dM} = \gamma\left[\rho(1-\gamma) - \frac{1}{\delta}\right]\frac{1-M^2}{M}\frac{1}{M^2\left(1-\frac{\chi}{\gamma}\right) + \rho(1-\gamma) - \frac{1}{\delta}} \tag{3-37}$$

3.2. Smooth Sonic Passage

Much information can be gathered by examining the isocline map of Eq. 3-37, i.e. marking up the slopes at various points in the (M,γ) plane, as given by 3-37. The first question is that of the existence of singularities, or points where both the numerator and denominator of 3-37 are zero, so that trajectories may pass through smoothly. We can see at least two such points:

(a) At $M = \gamma = 0$, we have locally

$$\frac{d\gamma}{dM} = \frac{\gamma}{M} \qquad 3\text{-}38$$

which indicates a linear approach to the origin, although the slope is not defined by this alone. An isocline map of this region is shown in Figure 3-4. Two crossings of (0,0) are observed, one from quadrant 3 to 1 and one from quadrant 2 to 4. The crossing from quadrant 2 to 4 corresponds to negative plasma densities, a non-physical result.

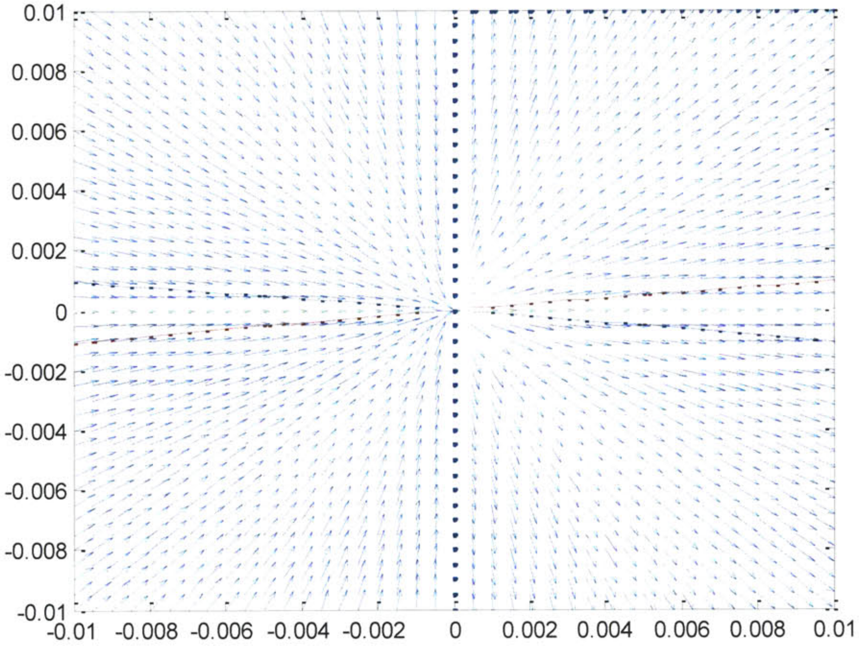

Figure 3-4: Isocline of Eq. 3-37 near (0,0). Isocline corresponds to $\rho = 2,\ \chi = 1.2245$, and $\delta = \infty$.

(b) More importantly, when M=1 and

$$\left(1 - \frac{\chi}{\gamma}\right) + \rho(1 - \gamma) - \frac{1}{\delta} = 0 \qquad 3\text{-}39$$

we have a smooth sonic passage, which is a necessary condition for acceleration to high ion velocities in a constant-area portion of the channel. Notice that one could also pass through M=1 with infinities in the gradients, at the end of the channel, but it can be shown that this mode of operation is less efficient.

The condition 3-39 yields a quadratic equation for $\gamma = \gamma_s$, the sonic ion flux. If we disregard the residual ionization beyond the sonic point, this quantity is also the utilization factor, η_u. The formal solution of 3-39 is given by Eq. 3-40.

$$\gamma_s = \frac{1 + \left(1 - \frac{1}{\delta}\right)/\rho}{2} \pm \sqrt{\left(\frac{1 + \left(1 - \frac{1}{\delta}\right)/\rho}{2}\right)^2 - \frac{\chi}{\rho}} \qquad \text{3-40}$$

We can immediately see that a solution would exist for the smooth sonic passage only if

$$\chi < \frac{\left(1 - \frac{1}{\delta} + \rho\right)^2}{4\rho} \qquad \text{3-41}$$

If χ is lower than the limit given in Eq. 3-41, two solutions exist for $\gamma_s = \eta_u$. Of these, the higher value approaches unity as $\rho \rightarrow \infty$, while the lower one approaches 0. This suggests the upper root as the physically important one, and this is confirmed by examining the behavior of trajectories in the vicinity of the two critical points: those crossing the lower critical point towards M<1 turn around and do not approach M=0. We therefore select the positive sign in Eq. 3-40. For justification, Figure 3-5 shows an isocline of Eq. 3-37 with the trajectory from the upper γ_s to (0,0) shown in thick black. Further, Figure 3-4 only shows one physical crossing of (0,0) which means the trajectory shown in Figure 3-5 must be the only physical trajectory for the smooth sonic passage criterion.

The slope with which a trajectory can cross this sonic singularity can be calculated by using L'Hopital's rule to resolve the 0/0 situation in Eq. 3-37. A short derivation with the derivative of the numerator of 3-37 with respect to M, the derivative of the denominator, and the quadratic equation for the critical slope are shown below. The critical slope is renamed as $d_s = \left.\frac{d\gamma}{dM}\right|_s$.

$$f(M) = \gamma\left[\rho(1-\gamma) - \frac{1}{\delta}\right]\frac{1-M^2}{M} \qquad f'(M=1) = -2\gamma_s\left[\rho(1-\gamma_s) - \frac{1}{\delta}\right] \tag{3-42}$$

$$g(M) = M^2\left(1 - \frac{\chi}{\gamma}\right) + \rho(1-\gamma) - \frac{1}{\delta} \qquad g'(M=1) = 2\left(1 - \frac{\chi}{\gamma_s}\right) + \left(\frac{\chi}{\gamma_s^2} - \rho\right)d_s \tag{3-43}$$

$$\left.\frac{d\gamma}{dM}\right|_s = d_s = \frac{f(M=1)}{g(M=1)} = \frac{f'(M=1)}{g'(M=1)} = \frac{-2\gamma_s\left[\rho(1-\gamma_s) - \frac{1}{\delta}\right]}{2\left(1 - \frac{\chi}{\gamma_s}\right) + \left(\frac{\chi}{\gamma_s^2} - \rho\right)d_s} \tag{3-44}$$

$$\left(\frac{\chi}{\gamma_s^2} - \rho\right)d_s^2 - 2\left(\frac{\chi}{\gamma_s} - 1\right)d_s + 2\gamma_s\left[\rho(1-\gamma_s) - \frac{1}{\delta}\right] = 0 \tag{3-45}$$

Eq. 3-45 is to be solved for the two possible crossing slopes at each of the two critical crossings, of which we have selected the one with the higher γ_s. Selecting between the two crossing slopes at this critical point is again not easy without examining the isocline map (M, γ). The isocline in the vicinity of the upper critical point is shown in Figure 3-6:

The rest of the map indicates that the line with a positive slope of order unity can connect to the origin, and the pattern of nearby trajectories indicate that integration backwards from the critical point is stable, as can be observed by the thick black line in Figure 3-5. To verify that the upper sonic flux with the positive slope is the only real solution, all four combinations of sonic flux and slope were examined numerically. Only the chosen case was able to integrate to (0,0).

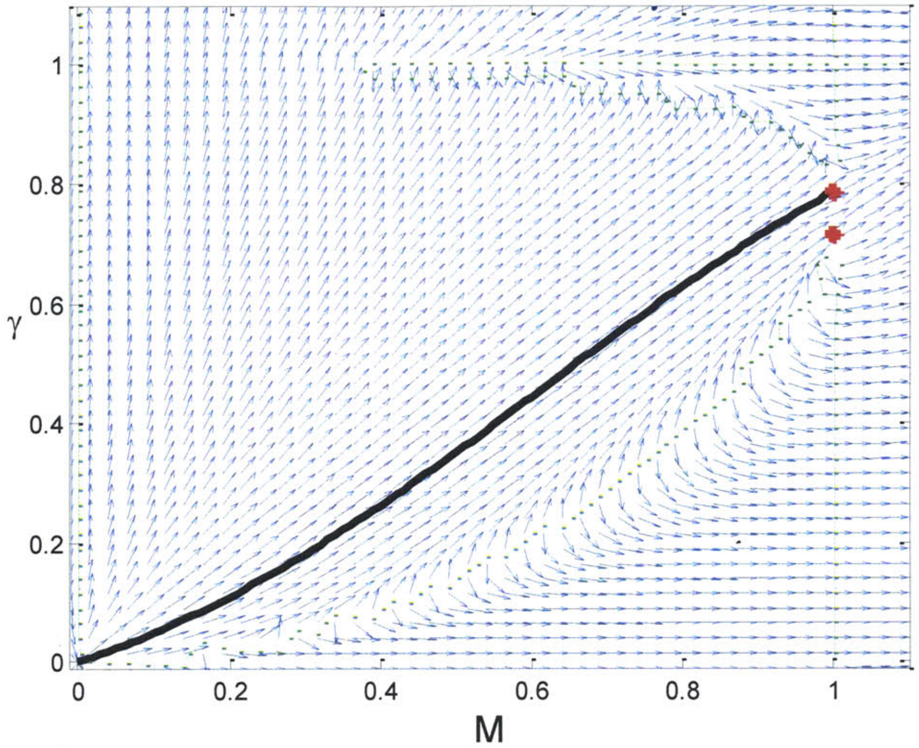

Figure 3-5: Isocline of Eq. 3-37 with the trajectory from the upper γ_s to (0,0) in thick black. The light green are approximate lines of constant slope for slopes of zero and infinity. Isocline corresponds to $\rho = 2,\ \chi = 1.2245$, and $\delta = \infty$ (no wall losses). The large red dots are the upper and lower γ_s. A higher resolution isocline map of near a critical point is shown in Figure 3-6.

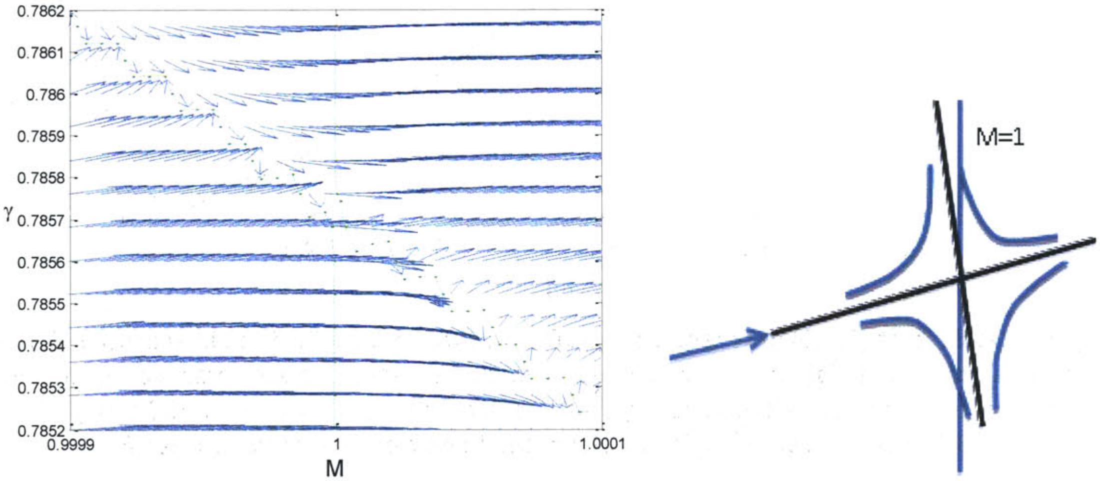

Figure 3-6: Isoclines in the vicinity of the upper γ_s and a qualitative sketch of the region. Isoclines correspond to $\rho = 2,\ \chi = 1.2245$, and $\delta = \infty$ (no wall losses).

3.3. Existence Conditions

It was found that the existence of a smooth sonic passage requires the condition of Eq. 3-41 between χ, ρ, and δ, repeated here as Eq. 3-46. A similar condition can be found by requiring that the quadratic equation for the critical slope d_s, Eq. 3-45, have real roots. After some algebra, this is found to be the condition 3-47.

$$\chi < \frac{\left(1 - \frac{1}{\delta} + \rho\right)^2}{4\rho} \tag{3-46}$$

$$\chi < \frac{2\left(\rho - \frac{1}{\delta}\right)^2 + 5\left(\rho - \frac{1}{\delta}\right) + 2}{9\rho} \tag{3-47}$$

but only if $\rho - \frac{1}{\delta} < 1$. If the reverse is true, Eq. 3-47 poses no restrictions. In addition, one also finds a limiting line for real d_s which corresponds to the condition $\gamma_s = \chi$, and which resolves to

$$\chi > 1 - \frac{1}{\rho\delta} \tag{3-48}$$

Finally, from Eq. 3-30 the ionization fraction at the sonic point should not exceed unity, so we need to impose $\gamma_s < 1$ on the solution 3-40. This yields, after simplification, the following two results

$$\chi > 1 - \frac{1}{\delta} \qquad\qquad \rho > 1 - \frac{1}{\delta} \tag{3-49}$$

The limits 3-46 and 3-47 are shown in Figure 3-7. The solid lines are the real γ_s limit (Eq. 3-46) and the dashed lines are the real d_s limit (Eq. 3-47). It can be seen that the two limits are about equally restrictive. Moving forward, the real γ_s limit will be used (Eq. 3-46).

Figure 3-8(a) shows the remaining smooth sonic passage existence limits, Eqs. 3-46, 3-48, and 3-49. The existence region for γ_s is the wedge for $\rho > 1 - \frac{1}{\delta}$ bounded above by the condition that γ_s be real and bounded below by the condition that γ_s be less than unity. Notice that within this existence region one could be below the line 3-48, the low efficiency case, so that no real trajectories would go through the sonic point. Presumably this is then the case when the sonic point moves to the channel exit and becomes singular, with infinite slopes in the 1-D approximation. Figure 3-8(b) shows the wedge (shaded) for $\delta = \infty$ case, or no wall losses.

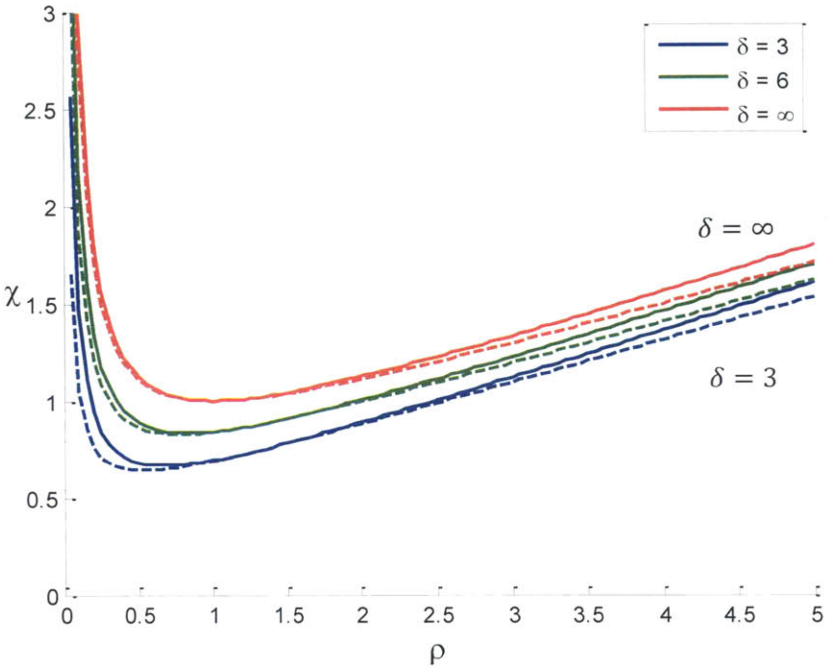

Figure 3-7: Max χ existence limits for different δ.

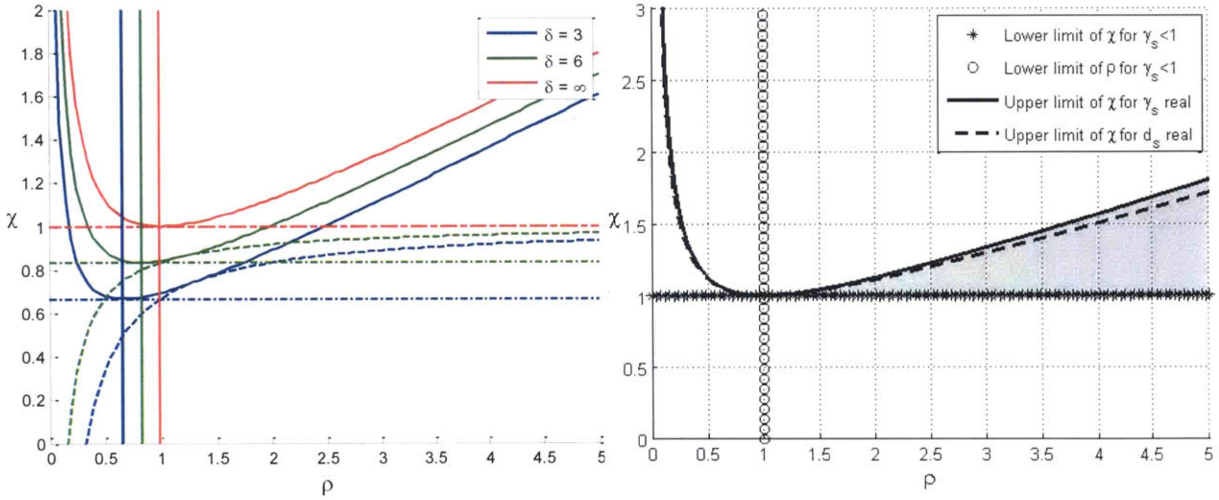

(a) (b)

Figure 3-8: (a) Smooth Sonic passage existence limits for Eqs. 3-46, 3-48, and 3-49. The vertical solid line is the minimum ρ in Eq. 3-49. The horizontal dashed line is the minimum χ from Eq. 3-49. The curved dashed line is the minimum χ from 3-48. The curved solid line is the maximum χ from Eq. 3-46. (b) Steady Sonic passage existence limits for $\delta = \infty$. The shaded portion is the existence region of smooth sonic passage.

In practice, the most important limit is Eq. 3-46, the real sonic ion flux condition. As written, Eq. 3-46 depends on three variables. This can be reduced to 2 variables, as follows, where Eq. 3-51 replaces 3-46.

$$X = 1 + \frac{1 - 1/\delta}{\rho} \qquad\qquad Y = \frac{\chi}{\rho} \tag{3-50}$$

$$Y \le \frac{X^2}{4} \tag{3-51}$$

This modifies Eq. 3-49 to:

$$Y > X - 1 \qquad\qquad X < 2 \tag{3-52}$$

Figure 3-9 shows the region of steady sonic passage in terms of the X and Y variables. For completeness, the physical meaning of X and Y are explored. X is a combination of the different characteristic lengths of the thruster and Y is the product of the ratio of charged mass to total mass times the ratio of ionization to diffusion length.

$$X = 1 + \frac{1 - 1/\delta}{\rho} = 1 + \left(\frac{l_{ioniz}}{l_{diff}} - 2\frac{l_{ioniz}}{h}\right) = 1 + \left(\frac{e\beta B v_n}{m_i R_i \Gamma_m} - 2\,\frac{v_B v_n}{R_i \Gamma_m h}\right) \tag{3-53}$$

$$Y = \frac{\chi}{\rho} = \frac{j}{e\Gamma_m}\frac{l_{ioniz}}{l_{diff}} = \frac{j}{e\Gamma_m}\frac{e\beta B v_n}{m_i R_i \Gamma_m} \tag{3-54}$$

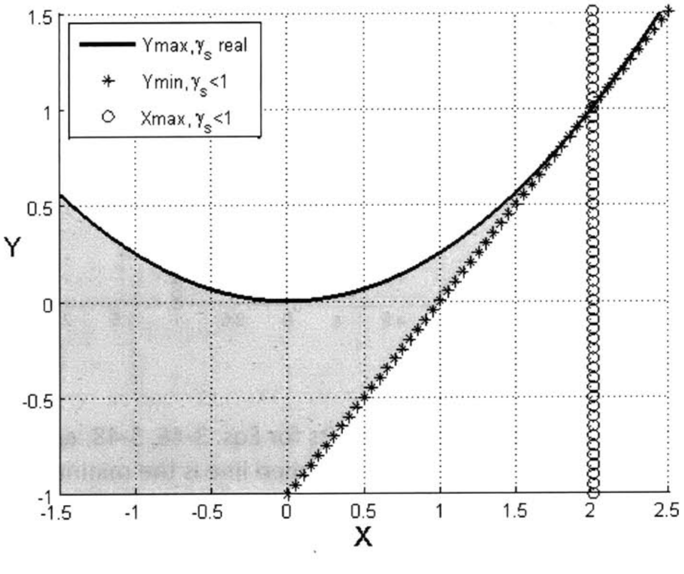

Figure 3-9: Smooth Sonic Passage existence region in variables X and Y.

3.4. Numerical Example

An example will be presented with $\rho = 2$, $\chi = 1.2245$, and $\delta = \infty$ which is slightly less than the maximum χ value indicated by 3-46. Solving the equation 3-40 gives the two possible critical fluxes:

$$\gamma_{s,lower} = 0.71429, \ \gamma_{s,upper} = 0.78571$$

The corresponding critical slopes are then, from 3-45

$$For\ \gamma_{s,lower},\ d_s = 0.83683 \ \ and \ \ d_s = 4.87824$$

$$For\ \gamma_{s,upper},\ d_s = 0.68592 \ \ and \ \ d_s = -5.40077$$

We use the rules for selection by starting from $\gamma_{s,upper} = 0.78571$ with the slope $d_s = 0.68592$ and marching backwards numerically with Eq. 3-37. The resulting trajectory is shown in Figure 3-10. Using the (M, γ) trajectory and Eqs. 3-10, 3-30, and 3-35, the profiles of *M*, N_e, and $N_n M_n$ can now be calculated and are shown in Figure 3-11.

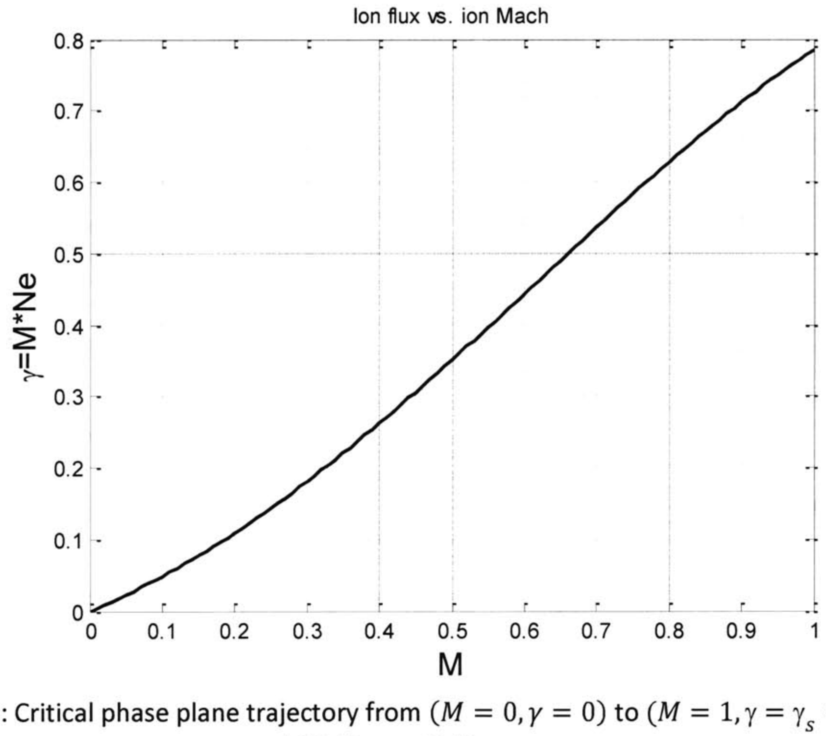

Figure 3-10: Critical phase plane trajectory from $(M = 0, \gamma = 0)$ to $(M = 1, \gamma = \gamma_s \approx \eta_u)$. For $\chi = 1.2245, \rho = 2, \delta = \infty$ case.

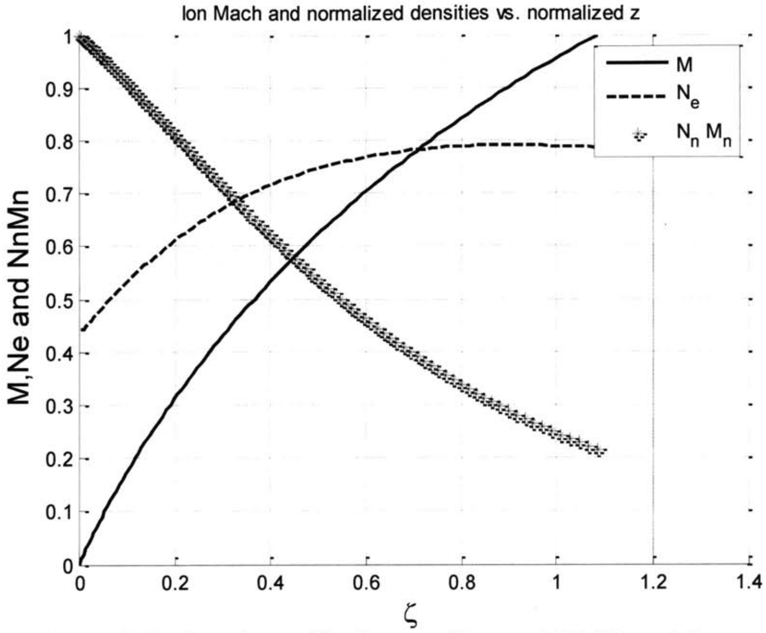

Figure 3-11: Steady profiles for $\rho = 2$, $\chi = 1.2245$, and $\delta = \infty$

As noted, the above example corresponds to a condition close to the limit for steady solution. The calculation for conditions gradually farther from this limit give similar results, but there are noticeable changes in the profile shapes. This is displayed in Figure 3-12, for the same χ but progressively larger ρ. The ion velocity (Mach number) profile becomes more convex, denoting a departure from a parabolic potential profile, and the electron density profile approaches a constant, except for a mild intermediate maximum. Also, the utilization efficiency $\eta_u = 1 - \gamma_s$ approaches unity as ρ increases.

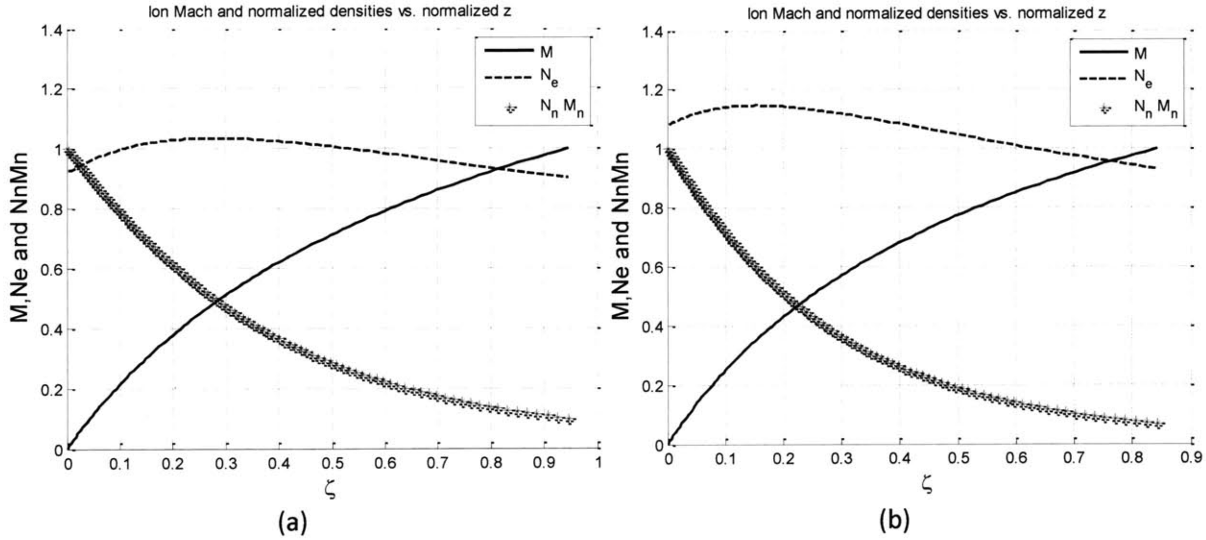

(a) (b)

Figure 3-12: Steady profiles for $\chi = 1.2245$, $\delta = \infty$, and (a) $\rho = 2.5$, (b) $\rho = 3$.

3.5. Steady State Results – Data Comparison

It was hypothesized that the smooth sonic passage limits correspond to limits where the thruster would operate in unstable modes. Existing SPT-100 data, compiled by Gascon et al., were compared to the limits[3]. Additionally, experimental data from a TAL, constructed by Yamamoto et al., were compared to the limits[4]. The SPT-100 data provide comparison across both a varying discharge potential and magnetic field. The TAL data provide comparison across a varying magnetic field.

For this preliminary comparison, several assumptions had to be made. The neutral velocity was assumed to be 252 m/s (corresponding to 600 K) and constant for all the data. The background pressure was ignored. For the SPT-100, the discharge current and coil current had to be converted to electron temperature and magnetic field, respectively. The TAL data directly provided the magnetic field. Additionally, the data will be presented for different anomalous diffusion coefficients since this coefficient is hard to predict even in ideal circumstances.

It is known that under normal operating conditions of 300 V, the maximum temperature in the SPT-100 on the cathode side of the ionization layer is about 24 eV. The SPT data considered below are for a thruster with boron-nitride walls. Separately, it is known that due to secondary emission, boron nitride will limit the maximum electron temperature to about 33 eV[25]. As the discharge voltage in the SPT-100 is increased, the maximum electron temperature should increase as well, until being limited by the wall material. The temperature in the ionization region, however, is below the maximum electron temperature for a given condition. It is assumed that the electron temperature in the ionization region is about 15 eV and 25 eV when the maximum temperature is 24 eV and 33 eV respectively. Equation 3-55 shows a fitting law created and used to convert from discharge voltage to electron temperature in the ionization region. This equation is only valid up to about 600 Volts. Figure 3-13 shows this equation graphically.

$$T_e(U_d) = 0.0467\, U_d + (20 - 0.0467\, U_d) \exp\left(-\frac{538}{U_d}\right) \qquad \text{3-55}$$

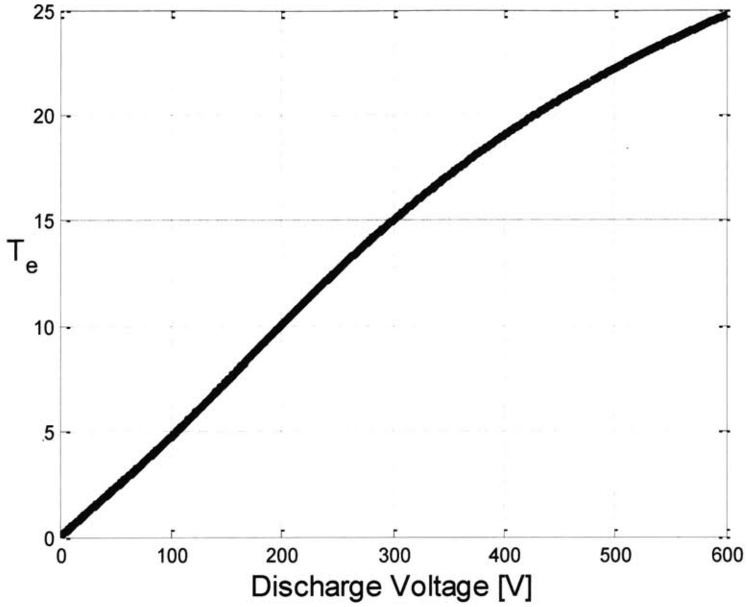

Figure 3-13: Assumed relation between discharge voltage and electron temperature in the ionization region of the SPT-100.

Gascon states the magnetic field of the SPT-100 is 200 Gauss at 4.5 A current, increases linearly until 5 A, and is constant above 5 A [3]. Equation 3-56 estimates this description of the magnetic field and is used to convert from coil current to magnetic field for the SPT-100 data.

$$B(I_C) = \min\left(\frac{0.02}{4.5} I_C, \frac{0.02}{4.5} 5\right) \quad 3\text{-}56$$

3.5.1. SPT-100 with Varying Discharge Potential

Data reduction for the SPT-100 with varying discharge potential uses Eq. 3-55 to estimate the electron temperature in the ionization region. The oscillation amplitude data can be viewed in Figure 3-14. In these experiments, the anode flow rate is kept at 5 mg/s and the discharge potential was varied from 70 to 350 V. The coil current is held at 4.5 Amps, corresponding to a 200 Gauss magnetic field. Data with anomalous diffusion parameters of 16 and 40 are shown. By looking at the data, the region below 100 V looks like it may be a glow discharge. The data points between 89 and 134 V appear to be unstable and oscillatory. The remaining points appear weakly stable, with the exception of the 350 V point.

For the X and Y data presented in Figure 3-15 and Figure 3-16, the discharge potential increases as Y decreases. Although not perfect, the transition between steady and periodic operation at 150 V is roughly captured by the max X line for both values of beta (in fact, the calculation would put the transition at around 200-225 V). It is interesting to note that the increasing oscillations at the 350 V data point corresponds to an X-Y coordinate that is approaching the lower X limit.

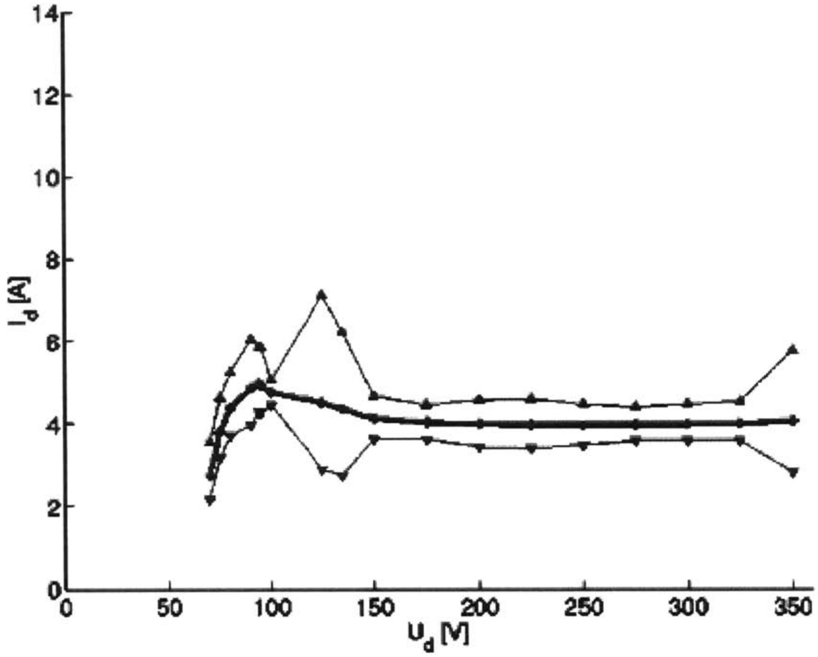

Figure 3-14: Discharge current and oscillation amplitude vs. discharge potential for SPT-100 from Gascon et al. $\dot{m}_a = 5\, mg/s$ Xenon. B=200 Gauss[3].

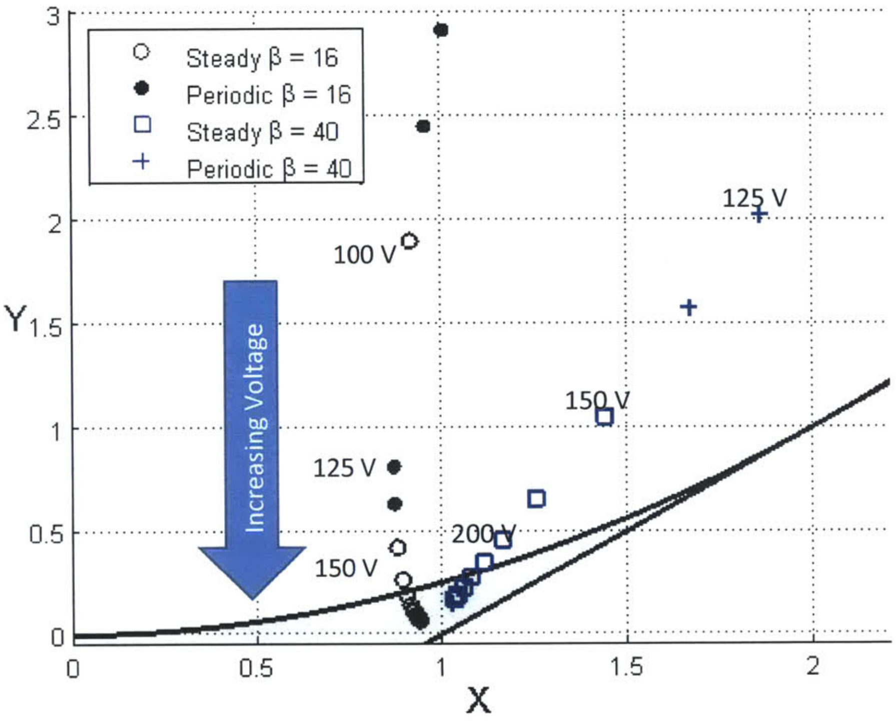

Figure 3-15: Experimental X and Y over stability limits for SPT-100 with varying discharge voltage

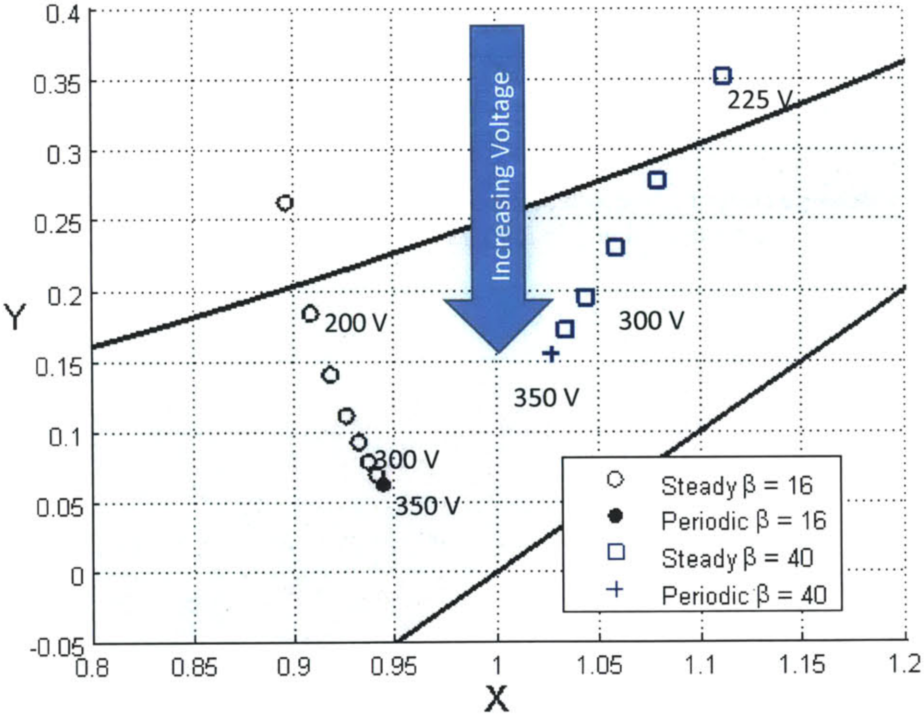

Figure 3-16: Experimental X and Y over stability limits for SPT-100 with varying discharge voltage, zoomed in. This region is for the highest voltages.

3.5.2. SPT-100 with Varying Magnetic Field Strength

For the SPT-100 data with varying magnetic field Eq. 3-56 is used to estimate the magnetic field strength in the ionization region. The oscillation data can be viewed in Figure 3-17. In these experiments, the anode flow rate is kept at 5 mg/s and the coil current was varied from 2.7 to 6.7 A. The discharge voltage was kept at 300 V, corresponding to an assumed 15 eV electron temperature in the ionization region. Anomalous diffusion parameters of 40 and 65 were used. By looking at the data, the region below a coil current of 3.5 A can be seen to be highly oscillatory. The data points above 3.5 A are steady. Keep in mind that the magnetic field does not vary much above a coil current of 5 A. In agreement with this, the oscillation data points above 5 A do not vary much either.

For the X and Y data presented in Figure 3-18, the magnetic field increases as X increases. The model correctly places the periodic data points on the unsteady side of the limit for $\beta = 65$. Most of the steady points are on the steady side of the limit. However, the larger values of magnetic field cross the limit back into the unsteady regime; this is not unambiguously observed experimentally, although the oscillation amplitude does pick up there. This may just be an artifact of inaccurate magnetic field values but in any case, these X-Y points are close to the limit line. For beta = 40, the data have the same trends, but placement on the correct side of the limit is not maintained.

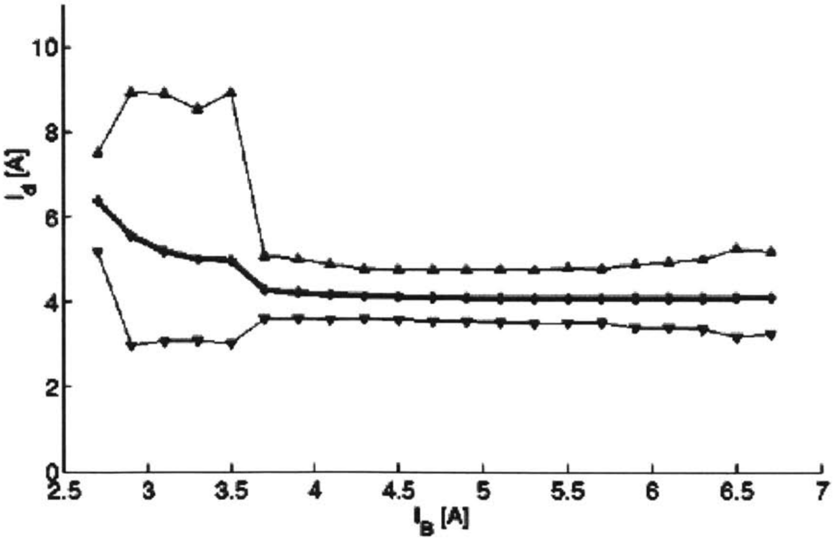

Figure 3-17: Discharge current and oscillation amplitude vs. coil current for SPT-100 from Gascon et al. $\dot{m}_a = 5\ mg/s$ Xenon V = 300 V[3].

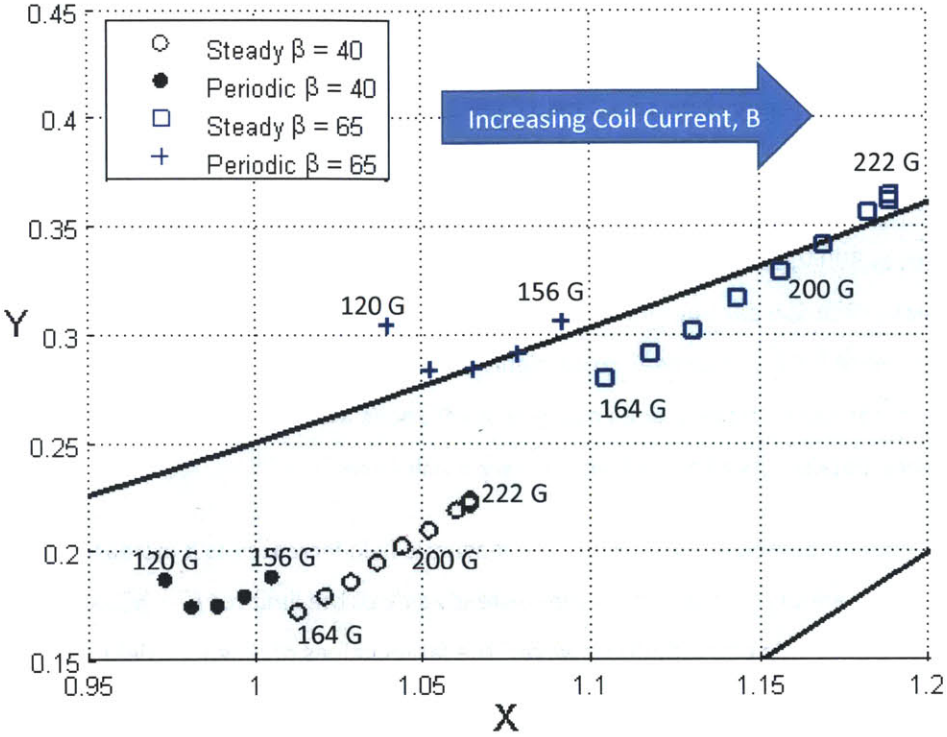

Figure 3-18: Experimental X and Y over stability limits for SPT-100 with varying magnetic field

3.5.3. TAL with Varying Magnetic Field Strength

The TAL data with varying magnetic field directly include the magnetic field. The electron temperature, however, is assumed to be 25 eV. In these experiments, the anode flow rate is kept at 2.72 mg/s and the magnetic field was varied from 140 and 740 Gauss. Anomalous diffusion parameters of 16 and 40 are shown.

For the X and Y data presented in Figure 3-19, the magnetic field increases as X increases. For beta = 40, the model correctly places all the periodic data points on the unsteady side of the limit and all of the steady points are on the steady side of the limit. For beta= 16, the data still have the correct trends, but the placement is skewed with respect to the upper X limit.

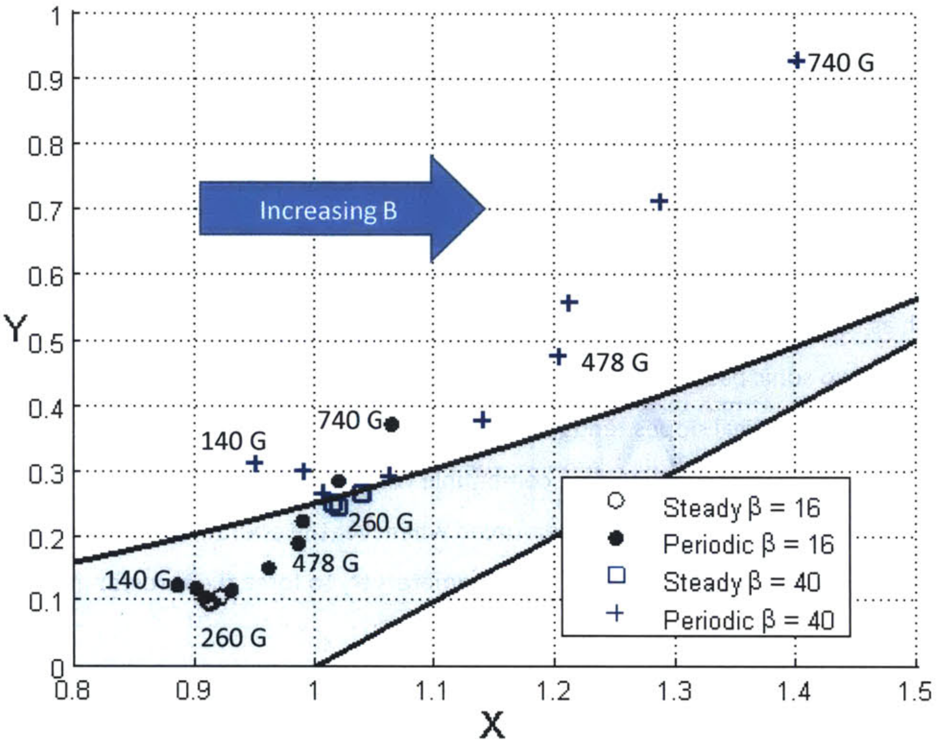

Figure 3-19: Experimental X and Y over stability limits for a TAL with varying magnetic field

The 3 datasets presented show that the steady model predicts the correct trends towards steady or unsteady behavior, although precise prediction is not quite achieved. As will be discussed later, refinements needed to improve these predictions are a method to estimate the electron temperature and the anomalous diffusion coefficient in the ionization region. Although improvements to the electron temperature estimation are plausible, modeling of the anomalous Hall parameter is likely to remain problematic, reflecting deficient understanding of cross-field electron diffusion and plasma turbulence in general.

3.6. Steady State Model Discussion

So far we have assumed a sonic point that is smooth and happens inside the constant-area part of the channel. There is, however, an alternative in which M=1 is reached at the channel exit, with the denominator in Eq. 3-37 not being simultaneously zero. Just upstream of the channel exit then, we expect $\frac{dM}{d\zeta}$ to be positive (tending to $+\infty$), and M to still be just below unity. From Eq. 3-35 then, the quantity $M^2(1-\chi/\gamma)+\rho(1-\gamma)-1/\delta$ should be positive, which can be verified to imply that γ

should be between the two smooth sonic passage fluxes. At the crossing through $M = 1$, then, these fluxes must exist, even though the trajectory actually crosses between them. It then seems as though the non-existence of smooth sonic passages, i.e., the inverse condition of Eq. 3-41, $\chi > \frac{1}{4\rho}\left(1 - \frac{1}{\delta} + \rho\right)^2$, must imply unsteady behavior, not merely a choked channel exit.

There remains, however, the possibility that the thruster, through the rest of its physics, would modify conditions such as to operate steadily at exactly $\chi = (1 - (1/\delta) + \rho)^2/4\rho$ or below, never above. For this condition, the two sonic passage fluxes merge into one, with $\gamma_s = (1 + (1 - 1/\delta)/\rho)/2$. Also, for this condition one of the critical slopes tends to this same limit and the other one tends to negative infinity. This second critical slope is therefore compatible with operation with the exit choked, but it is not clear by what mechanisms this would be enforced whenever the operating parameters approach the non-existence limit, or what would happen if the parameters try to force the thruster into the non-existence region.

If we accept Eq. 3-41 as the limit for steady operation, there is still the related question of whether this steady solution is stable. A stability analysis of this model, even when linearized, is fairly complex analytically (see Ref. 17), and it may be more productive to attack this issue through the use of a fully non-linear 1D plus time numerical model, essentially the same as Matlock's[5], but simplified possibly through the neglect of wall effects and other secondary issues.

Given these uncertainties, it seems best at this point to hypothesize that unsteadiness would start whenever 3-41 is not satisfied. This has been tested by comparison to experimental data and the results look promising. Due to uncertainties of some quantities such as the effective Hall parameter, the correct trends is the best that a model such as this can hope to achieve, but these trends are still very useful when examining a thruster.

Chapter 4

Transient Model of the Ionization Region

When the thruster does not meet the criteria for steady operation, it is predicted to operate in an unsteady manner and either oscillate or extinguish. The original intent of the model formulated in this section was to investigate the unsteady behavior. Although, as it will be seen, more work is needed to reveal the unsteady behavior, this model still reveals the nature of the oscillations in the thruster. This transient model starts with many of the same assumptions as the steady model, but also assumes periodicity. For a thruster that does not meet the steady criterion, it was intended that finding a solution to this transient model would clarify whether the thruster oscillates or extinguishes. The transient model considers two distinct phases in the cycle. The first phase is plasma expansion with neutral re-fill and the second phase is rapid ionization.

The plasma expansion phase follows the latest ionization flash. During this period, neutrals are greatly depleted causing ionization to be initially negligible. The plasma expands as ions accelerate out of the ionization region and wall losses accrue. The neutral gas steadily returns and re-fills the ionization region, eventually causing ionization to pick up. Although this initial ionization is clearly not uniform in space, during the plasma expansion phase it is analytically useful to treat ionization and wall loss as an average over the ionization thickness (justifiable in part from Figure 3-1 to Figure 3-3). Once ionization accelerates, this assumption breaks down and the model is switched to the rapid ionization phase in which ionization rapidly depletes all the neutrals. The non-dimensionalized governing equations are repeated below (originally Eqs. 3-18 to 3-23).

For clarity, the expansion phase assumes wall losses and ionization are dependent upon the spatially averaged neutral density, but the wall losses and ionization do not affect the neutral profile. Instead, neutrals are assumed to be a simple advancing front that only depends on time. The rapid ionization phase freezes the advancing neutral front and neglects the convective term because ionization occurs over a much shorter time scale.

$$\frac{\partial N_e}{\partial t'}+\frac{\partial (N_e M_e)}{\partial \zeta}=\rho M_n N_n N_e-\frac{N_e}{\delta} \qquad \text{4-1}$$

$$\frac{\partial N_e}{\partial t'}+\frac{\partial (N_e M)}{\partial \zeta}=\rho M_n N_n N_e-\frac{N_e}{\delta} \qquad \text{4-2}$$

$$\frac{\partial N_n}{\partial t'}+M_n\frac{\partial (N_n)}{\partial \zeta}=-\rho M_n N_n N_e+\frac{N_e}{\delta} \qquad \text{4-3}$$

$$M_e=-\left(\hat{E}_z+\frac{\partial \ln N_e}{\partial \zeta}\right) \qquad \text{4-4}$$

$$\Phi=-\frac{1}{2}M^2=\frac{e\phi}{T_e} \qquad \hat{E}_z=M\frac{\partial M}{\partial \zeta} \qquad \text{4-5}$$

$$N_e(M-M_e)=\chi(t') \qquad \text{4-6}$$

4.1. Plasma Expansion Phase

4.1.1. Solution for the Expanding Plasmoid

As mentioned, it is analytically useful to treat the ionization and wall loss as an average over the ionization thickness during the plasma expansion phase. Accepting this, we define through Eq. 4-7 an effective ionization frequency, I, which is a function of time only, and the ion conservation Eq. 4-2 becomes Eq. 4-8. By combining Eqs. 4-4 and 4-5 into Eq. 4-6 the current conservation law becomes Eq. 4-9.

$$I = \rho M_n N_n - \frac{1}{\delta} \tag{4-7}$$

$$\frac{1}{N_e}\frac{\partial N_e}{\partial t'} + \frac{1}{N_e}\frac{\partial N_e M}{\partial \zeta} = \frac{\partial \ln N_e}{\partial t'} + M\frac{\partial \ln N_e}{\partial \zeta} + \frac{\partial M}{\partial \zeta} = I(t') \tag{4-8}$$

$$\chi(t') = N_e M\left(1 + \frac{\partial M}{\partial \zeta}\right) + \frac{\partial N_e}{\partial \zeta} \tag{4-9}$$

If the ion Mach number spatial variation were known at some time t', Eq. 4-9 could be regarded as a linear, first order differential equation for the plasma density, N_e. For short, the following quantity $f(\zeta, t')$ is defined and the formal solution of Eq. 4-9 is given in Eq. 4-11, where $N_{e0}(t') = N_e(\zeta = 0, t')$ is the density at the entry to the ionization layer. This gives the plasma density spatial profile for a given ion Mach number spatial profile.

$$f(\zeta, t') = M\left(1 + \frac{\partial M}{\partial \zeta}\right) \tag{4-10}$$

$$N_e = \frac{1}{\mu(\zeta)}\left[N_{e0} + \chi \int_0^{\zeta} \mu(\zeta')d\zeta'\right] \tag{4-11}$$

$$\mu(\zeta) = \exp\left(\int_0^{\zeta} f(\zeta')d\zeta'\right) \tag{4-12}$$

The ion Mach number variation with space and time ($M(\zeta, t')$) will now be determined by invoking the ion conservation law, Eq. 4-8. Substitution of Eq. 4-11 into Eq. 4-8 gives the desired equation for *M*. This is a complex integro-differential equation that will not be written here. Instead, it will be assumed that $M(\zeta, t')$ can be expanded at a given t' as a power series in ζ. This expansion is truncated at the second order. This gives Eqs. 4-13 through 4-15.

$$M(\zeta, t') \approx b_1(t')\zeta + b_2(t')\zeta^2 \tag{4-13}$$

$$f \approx b_1(1 + b_1)\zeta + b_2(1 + 3b_1)\zeta^2 + 2b_2^2\zeta^3 \tag{4-14}$$

$$\ln \mu(\zeta) \approx \frac{b_1}{2}(1 + b_1)\zeta^2 + \frac{b_2}{3}(1 + 3b_1)\zeta^3 + \frac{1}{2}b_2^2\zeta^4 \tag{4-15}$$

These terms resulting from the expansion of $M(\zeta, t')$ will be plugged into Eq. 4-11. First, the term in the integral is found by using the power series for the exponential $\exp(\ln \mu)$ truncated after the ζ^4 term to give Eq. 4-16 through 4-18.

$$\mu(\zeta) = \exp(\pm \ln \mu) \approx 1 \pm \ln \mu + \frac{1}{2}(\ln \mu)^2 \tag{4-16}$$

$$\mu(\zeta) \approx 1 + \frac{b_1}{2}(1+b_1)\zeta^2 + \frac{b_2}{3}(1+3b_1)\zeta^3 + \left(\frac{b_1^2}{8}(1+b_1)^2 + \frac{1}{2}b_2^2\right)\zeta^4 \tag{4-17}$$

$$\frac{1}{\mu(\zeta)} = 1 - \frac{b_1}{2}(1+b_1)\zeta^2 - \frac{b_2}{3}(1+3b_1)\zeta^3 + \left(\frac{b_1^2}{8}(1+b_1)^2 - \frac{1}{2}b_2^2\right)\zeta^4 \tag{4-18}$$

Eqs. 4-16 through 4-18 are plugged into 4-11 and the following is obtained.

$$\begin{aligned} N_e \approx N_{e0}&\left[1 - \frac{b_1}{2}(1+b_1)\zeta^2 - \frac{b_2}{3}(1+3b_1)\zeta^3 + \left(\frac{b_1^2}{8}(1+b_1)^2 - \frac{1}{2}b_2^2\right)\zeta^4\right] \\ &+ \chi\left[\zeta - \frac{b_1}{3}(1+b_1)\zeta^3 - \frac{b_2}{4}(1+3b_1)\zeta^4\right] \end{aligned} \tag{4-19}$$

Next, Eq. 4-19 is substituted into 4-8. This is expanded and terms of like order in ζ are collected. We will only require terms up to ζ^2. These equations contain mixed time derivatives of the quantities N_{e0}, χ, b_1 and b_2 which are algebraically separated to yield a system. We start by dropping all terms in Eq. 4-19 above ζ^2 to give Eq. 4-20. Eq. 4-8 is then modified to give Eq. 4-21. Eqs. 4-22 and 4-23 are then plugged into Eq. 4-21 to obtain Eq. 4-24 where only terms up to ζ^2 have been retained.

$$N_e \approx N_{e0}\left[1 - \frac{b_1}{2}(1+b_1)\zeta^2\right] + \chi\zeta \tag{4-20}$$

$$\frac{\partial N_e}{\partial t'} + M\frac{\partial N_e}{\partial \zeta} + N_e\frac{\partial M}{\partial \zeta} = N_e I(t') \tag{4-21}$$

$$\frac{\partial N_e}{\partial t'} \approx N_{e0}\left[-\frac{1}{2}\frac{db_1}{dt'}(1+2b_1)\zeta^2\right] + \frac{dN_{e0}}{dt'}\left[1 - \frac{b_1}{2}(1+b_1)\zeta^2\right] + \frac{d\chi}{dt'}\zeta \tag{4-22}$$

$$\frac{\partial N_e}{\partial \zeta} \approx N_{e0}[-(b_1 + b_1^2)\zeta] + \chi \tag{4-23}$$

$$\left[\frac{dN_{e0}}{dt'} - N_{e0}(I - b_1)\right] + \left[\frac{d\chi}{dt'} - \chi\left(I - 2b_1 - 2b_2\frac{N_{e0}}{\chi}\right)\right]\zeta$$
$$+ \left[\frac{b_1}{2}(1 + b_1)\left(N_{e0}I - 3b_1N_{e0} - \frac{dN_{e0}}{dt'}\right) + 3b_2\chi - \frac{(1 + 2b_1)}{2}\frac{db_1}{dt'}N_{e0}\right]\zeta^2 = 0 \qquad \text{4-24}$$

Next, the quantities in Eq. 4-24 are algebraically separated by equating separately to zero each of the coefficients of the powers of ζ to obtain the following system of Eqs. 4-25 to 4-27. This system can be solved to give N_{e0}, χ, and b_1 as functions of time provided a relationship between b_2 and b_1 can be found. N_{e0} and b_1 can then be used to used to solve Eq. 4-11.

$$\frac{d\ln N_{e0}}{dt'} = I - b_1 \qquad \text{4-25}$$

$$\frac{d\ln\chi}{dt'} = I - 2b_1 - 2b_2\frac{N_{e0}}{\chi} \qquad \text{4-26}$$

$$\frac{1 + 2b_1}{2}\frac{db_1}{dt'} = -b_1^2(1 + b_1) + 3b_2\frac{\chi}{N_{e0}} \qquad \text{4-27}$$

To find a relation between b_1 and b_2, the diffusion region is given a brief look. Since this region is itself prone to a different kind of limitation (anode deletion), it is examined in more detail in Chapter 5, and only a simplified version is included here. This extends the model into negative ζ values from ζ_a to 0, where ζ_a is the position of the anode from the start of the ionization zone, a negative distance. ζ_a is taken as a constant with respect to time. In this region we can consistently take the ion velocity to be zero ($M = 0$), which makes Eq. 4-9 imply a spatially linear variation of N_e.

$$\int_{N_{ea}}^{N_e} dN_e = \chi(t')\int_{\zeta_a}^{\zeta} d\zeta \qquad \text{4-28}$$

$$N_e = N_{ea} + \chi(t')(\zeta - \zeta_a) \qquad \text{4-29}$$

For simplicity, we now make the further approximation that the operating point is such that the plasma density is near zero close to the anode. This is often chosen for efficient operation. Particularizing Eq. 4-29 at $\zeta = 0$ (i.e. the start of the ionization layer), where $N_e = N_{e0}$, we obtain the useful relationship, Eq. 4-30, valid at all times.

$$N_{e0}(t') = (-\zeta_a)\chi(t') \tag{4-30}$$

An immediate consequence of Eq. 4-30 can be seen by subtracting Eq. 4-26 from 4-25 to give 4-31. Since Eq. 4-30 states the ratio of N_{e0} and χ is constant at all times, the derivative in Eq. 4-31 is zero. This results in the relation shown in Eq. 4-32 which, with addition to Eq. 4-30, can be substituted into 4-27 to obtain an equation for $b_1(t')$, shown in Eq. 4-33. The quantity A is defined for convenience.

$$\frac{d\ln(N_{e0}/\chi)}{dt'} = b_1 + 2b_2\frac{N_{e0}}{\chi} \tag{4-31}$$

$$b_2 = \frac{-b_1}{2(-\zeta_a)} = \frac{-b_1}{2}\frac{\chi}{N_{e0}} \tag{4-32}$$

$$\frac{db_1}{dt'} = \frac{-2b_1\left(b_1^2 + b_1 + \frac{3/2}{\zeta_a^2}\right)}{1 + 2b_1} \tag{4-33}$$

$$A \equiv \frac{\zeta_a^2}{3/2} \tag{4-34}$$

Eq. 4-33 can be integrated via separation of variables to give Eq. 4-35. Here b_{10} is the initial value of b_1. Eq. 4-36 gives r^+ and r^-.

$$t' = \frac{A}{4}\ln\left(\frac{r^+r^-}{b_1^2}\frac{b_{10}^2}{r_0^+r_0^-}\right) + 2\frac{(A/4+1)}{\sqrt{4/A-1}}\left[\arctan\left(\frac{1+2b_1}{\sqrt{(4/A)-1}}\right) - \arctan\left(\frac{1+2b_{10}}{\sqrt{(4/A)-1}}\right)\right] \tag{4-35}$$

$$r^+ = b_1 + \frac{1}{2} + \sqrt{\frac{1}{4} - \frac{1}{A}} \qquad r^- = b_1 + \frac{1}{2} - \sqrt{\frac{1}{4} - \frac{1}{A}} \tag{4-36}$$

The type of time dependence of b₁ is illustrated in Figure 4-1 for various values of ζ_a, for $b_{10} = 1$. The decrease of b₁ with time is steeper for the shorter channels, and tends to an asymptotic limit when the anode position moves an infinite distance away, $\zeta_a \to -\infty$. This limit is shown in Eq. 4-37 and Figure 4-1.

$$\lim_{\zeta_a \to -\infty} t' = \frac{1}{2}\left[\frac{1}{b_1} - \frac{1}{b_{10}} + \ln\left(\frac{b_{10}}{1+b_{10}}\frac{1+b_1}{b_1}\right)\right] \qquad 4\text{-}37$$

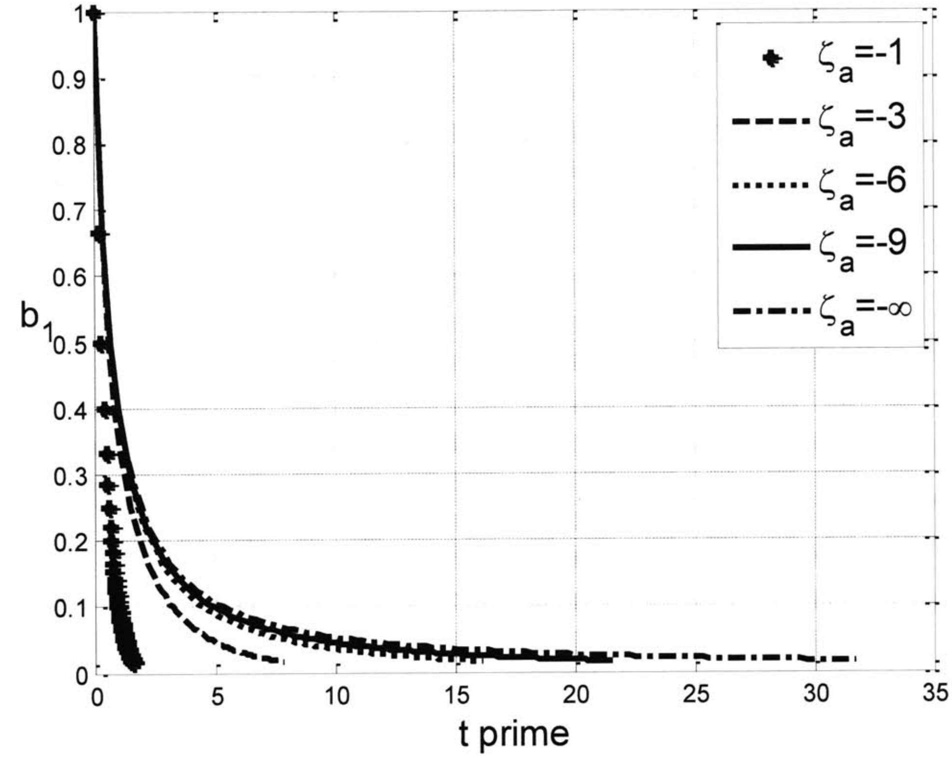

Figure 4-1: Variation of b_1 for various anode-ionization layer distances, $b_{10} = 1$

The variation of b_2 is simply proportional to that of b_1, according to Eq. 4-32. The variations of N_{e0} and χ follow from Eqs. 4-25 and 4-26, with b_2 from Eq. 4-32:

$$\frac{d\ln N_{e0}}{dt'} = \frac{d\ln\chi}{dt'} = I(t') - b_1(t') \qquad 4\text{-}38$$

This integration is best performed with respect to b_1. To change the base, Eq. 4-33 is used to modify Eq. 4-38 which is shown below in Eq. 4-39 and integrated in Eq. 4-40. Recalling from Eq. 4-7, $I = \rho M_n N_n - 1/\delta$, and the fact that $N_{na}M_n = 1$, we have Eq. 4-41, where the neutral profile is spatially averaged. Once the neutral profile is spatially averaged in the next section, Eq. 4-40 can be solved to provide N_{e0}

as a function of time. This can then be plugged into Eq. 4-11 to obtain the plasma density profile as a function of time. Recall that the Eq. 4-35 gives the relation between time and b_1.

$$\int_{\ln N_{e0,0}}^{\ln N_{e0}} d\ln N'_{e0} = \int_{\ln \chi_0}^{\ln \chi} d\ln \chi' = \int_0^{t'} I(t'')dt'' + \frac{1}{2}\int_{b_{10}}^{b_1} \frac{1+2b'_1}{b'^2_1 + b'_1 + \frac{1}{A}} db'_1 \qquad 4\text{-}39$$

$$\ln\left(\frac{N_{e0}}{N_{e0,0}}\right) = \ln\left(\frac{\chi}{\chi_0}\right) = \int_0^{t'} I(t'')dt'' + \ln\left(\frac{b_1^2 + b_1 + \frac{1}{A}}{b_{10}^2 + b_{10} + \frac{1}{A}}\right) \qquad 4\text{-}40$$

$$\int_0^{t'} I\, dt'' = \rho \int_0^{t'} \frac{\langle N_n \rangle}{N_{na}} dt' - \frac{1}{\delta} t' \qquad 4\text{-}41$$

4.1.2. Neutral Re-fill Profile During Early Ionization

This section specifies a neutral profile, N_n/N_{na} and spatially averages it over the ionization distance. This will allow the explicit calculation of the integral of I in Eq. 4-41. Before ionization strongly depletes the neutrals, their profile is simply advancing at a speed v_n and we have Eq. 4-42 where G is a shape function depending upon the previous ionization "bite", and tending to unity when its argument tends to $-\infty$.

$$\frac{N_n}{N_{na}} \approx G(\zeta - M_n t') \qquad 4\text{-}42$$

The width of the front must be of the order of the ionization distance l_{ion}, which is a factor $1/\rho$ times the reference distance l_{diff}. Thus, the width of the front will be set to a multiple of the ionization thickness, w. In terms of ζ, this means the neutral front has a thickness of w/ρ, where $w = 1$ corresponds to the width of the front being equal to the width of the ionization thickness. Physically, the "bite" out of the neutrals should be at least the size of the ionization region, corresponding to $w \geq 1$. Mathematically, by limiting the model to $w \geq 1$, the spline is simplified to fewer pieces.

Its upstream edge must be located some distance λl_{ion} ahead of the start ($\zeta = 0$) of the ionization layer, with λ being some number of the order of $w/2$. A convenient form for this kind of profile is a cubic spline, such that, in terms of a normalized travelling distance, u, gives Eq. 4-43. Note that $t'_n = \rho M_n t'$.

$$u = \rho(\zeta - M_n t') + \lambda = \rho\zeta - t'_n + \lambda \qquad 4\text{-}43$$

(a) For $t'_n < -(w - \lambda)$

$$\frac{N_n}{N_{na}} = 0 \qquad 4\text{-}44$$

(b) For - $(w - \lambda) < t'_n < \lambda + 1 - w$

$$\frac{N_n}{N_{na}} = 1 - 3\left(\frac{u}{w}\right)^2 + 2\left(\frac{u}{w}\right)^3 \qquad \left(if\ \zeta < \frac{w + t'_n - \lambda}{\rho}\right) \qquad 4\text{-}45$$

$$\frac{N_n}{N_{na}} = 0; \qquad (otherwise)$$

(c) For $\lambda + 1 - w < t'_n < \lambda + 1$

$$\frac{N_n}{N_{na}} = 1; \qquad \left(if\ \zeta < \frac{t'_n - \lambda}{\rho}\right)$$

$$\frac{N_n}{N_{na}} = 1 - 3\left(\frac{u}{w}\right)^2 + 2\left(\frac{u}{w}\right)^3; \qquad \left(if\ \frac{t'_n - \lambda}{\rho} < \zeta < \frac{1}{\rho}\right) \qquad 4\text{-}46$$

$$\frac{N_n}{N_{na}} = 0; \qquad (otherwise)$$

(d) For $t'_n > \lambda + 1$

$$\frac{N_n}{N_{na}} = 1 \qquad 4\text{-}47$$

The shapes of these profiles are exemplified in Figure 4-2, for $w = 2.1$ and $\lambda = w/2$. The profile on the left is at time $t' = 0$ and on the right, at $t' = 19.6$. It is important to note that the time steps are not constant, causing the different spaces between the different profiles shown.

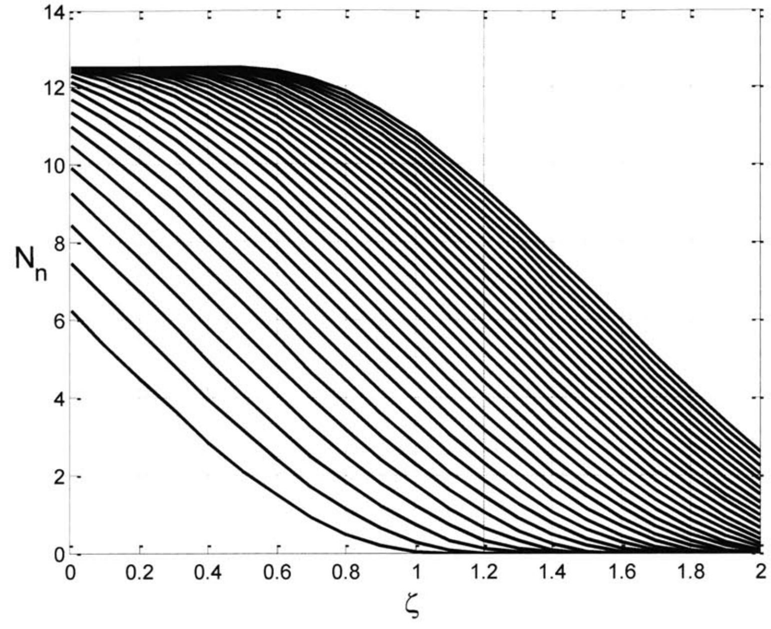

Figure 4-2: The un-depleted neutral profiles at various times

As required for Eq. 4-41, Eqs. 4-44 through 4-47 are spatially averaged according to Eq. 4-48. Care must be given while integrating the different sections of the spline as the integral is broken into separate integrals for the different section that are then summed. The results are given in Eqs. 4-49 to 4-52.

$$\frac{\langle N_n \rangle}{N_{na}} = \rho \int_0^{1/\rho} \frac{N_n}{N_{na}} d\zeta \qquad \text{4-48}$$

$$\frac{\langle N_n \rangle}{N_{na}} = 0; \qquad \text{(for } t_n' < -(w-\lambda)\text{)} \qquad \text{4-49}$$

$$\frac{\langle N_n \rangle}{N_{na}} = \frac{w}{2} - (\lambda - t_n') + \frac{1}{w^2}(\lambda - t_n')^3 - \frac{1}{2\,w^3}(\lambda - t_n')^4 \qquad \text{(for} -(w-\lambda) < t_n' < \lambda + 1 - w\text{)} \qquad \text{4-50}$$

$$\frac{\langle N_n \rangle}{N_{na}} = 1 - \frac{1}{w^2}(\lambda + 1 - t_n')^3 + \frac{1}{2\,w^3}(\lambda + 1 - t_n')^4 \qquad \text{(for } \lambda + 1 - w < t_n' < \lambda + 1\text{)} \qquad \text{4-51}$$

$$\frac{\langle N_n \rangle}{N_{na}} = 1 \qquad \text{(for } t_n' > \lambda + 1\text{)} \qquad \text{4-52}$$

Finally, Eqs. 4-49 through 4-52 are used to integrate in time Eq. 4-41. This integration, similar to the last, requires that the integral be broken up for the different segments in time due to the nature of the cubic spline. The results are shown below. Recall that $N_{na} M_n = 1$.

$$I_0 = \frac{\lambda(w^4 - w^3\lambda + w\lambda^3/2 - \lambda^4/5)}{2\,w^3} - \frac{(w-1)(w^3 + w(w-1)^3/2 - (w-1)^4/5)}{2\,w^3} \qquad \text{4-53}$$

For $t_n' < \lambda + 1 - w$

$$\int_0^{t'} I\,dt' = -\frac{1}{\delta}t' + \frac{1}{M_n}\left[\frac{w}{2}t_n' - \frac{\lambda^2 - (\lambda - t_n')^2}{2} + \frac{\lambda^4 - (\lambda - t_n')^4}{4\,w^2} - \frac{\lambda^5 - (\lambda - t_n')^5}{10\,w^3}\right] \qquad \text{4-54}$$

For $\lambda + 1 - w < t_n' < \lambda + 1$

$$\int_0^{t'} I\,dt' = -\frac{1}{\delta}t' + \frac{1}{M_n}\left[I_0 + w - 1 + t_n' - \lambda - \frac{w^4 - (\lambda + 1 - t_n')^4}{4\,w^2} + \frac{w^5 - (\lambda + 1 - t_n')^5}{10\,w^3}\right] \qquad \text{4-55}$$

For $t_n' > \lambda + 1$

$$\int_0^{t'} I\,dt' = -\frac{1}{\delta}t' + \frac{1}{M_n}\left[I_0 + w - 1 + t_n' - \lambda - \frac{3}{20}w^2\right] \qquad \text{4-56}$$

4.1.3. Sample Calculations

Results from these calculations for a particular case, with $w = 2.1$, $M_n = 0.08$, $\rho = 1$, $\delta = 2$, $\chi_0 = 2$, $\lambda = w/2$, $\zeta_a = -6$, and $b_{10} = 2/3$, are shown in Figure 4-3. It can be appreciated how in this case, the integral $\int_0^{t'} I\,dt'$, which accounts jointly for ionization and wall losses via Eq. 4-40, is initially negative (losses dominant), but it eventually recovers and grows strongly (ionization dominant). This indicates non-linear oscillations. For cases with smaller ρ (due to a lower T_e or higher density), the recovery may not occur, allowing the plasma to extinguish (but this has not really been explored so far).

The non-dimensional current $\chi(t')$ is also shown in Figure 4-3. It initially decays from the initial value of 2, due to the combination of plasma expansion and wall losses, but eventually it does recover, once the ionization/loss integral becomes positive for a long enough time. Once again, this may not happen for cases with a weak ionization parameter ρ.

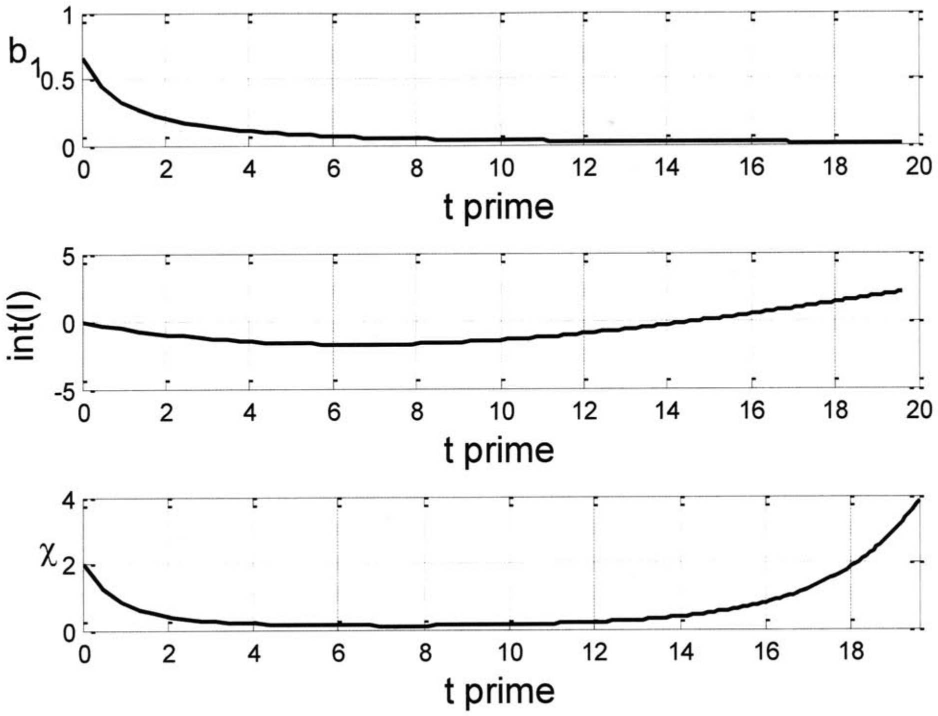

Figure 4-3: Calculations for one case. The quantity int(I) is the integral in Eqs. 4-54 to 4-56 and χ is $\chi(t')$, as calculated from Eq. 4-40.

Once the time-dependent parameters have been calculated, one can then compute the implied spatial profiles of ion Mach number and density with Eqs. 4-13 and 4-11, respectively. Figure 4-4 shows the ion Mach profiles for the sample case. The parameter b_{10} was chosen to ensure near-sonic velocity towards the exit of the ionization layer near $\zeta = 1/\rho$ at $t' = 0$. At later times, the Mach number is seen to decay rapidly as a consequence of the expansion of the initial plasmoid. Of course, the quadratic profile used here, and in general the series expansions in terms of distance, cannot be accurate downstream, but the behavior in the ionization layer (ζ less than roughly $1/\rho$, or unity in this case), is reasonable, showing the kind of curvature we found in the steady state profiles, see Figure 3-11.

The plasma density profiles are shown in Figure 4-5. The initial profile is seen to decrease across the ionization region, with a maximum near $\zeta = 0$, this profile is the one in the middle crossing many others. The density decays rapidly during the expansion phase up to $t' \approx 8$, when Figure 4-3 indicates a still decaying current. Later on, the density recovers everywhere at an accelerated rate, as ionization takes over. It must be kept in mind that the neutral density calculation resulting in this ionization is crude (averaged in space, non-depleting), but the behavior is at least physically sensible. It should be noted that the presented profiles go beyond when this model's assumptions break down. Later, only the profiles up to the ionization spike will be used.

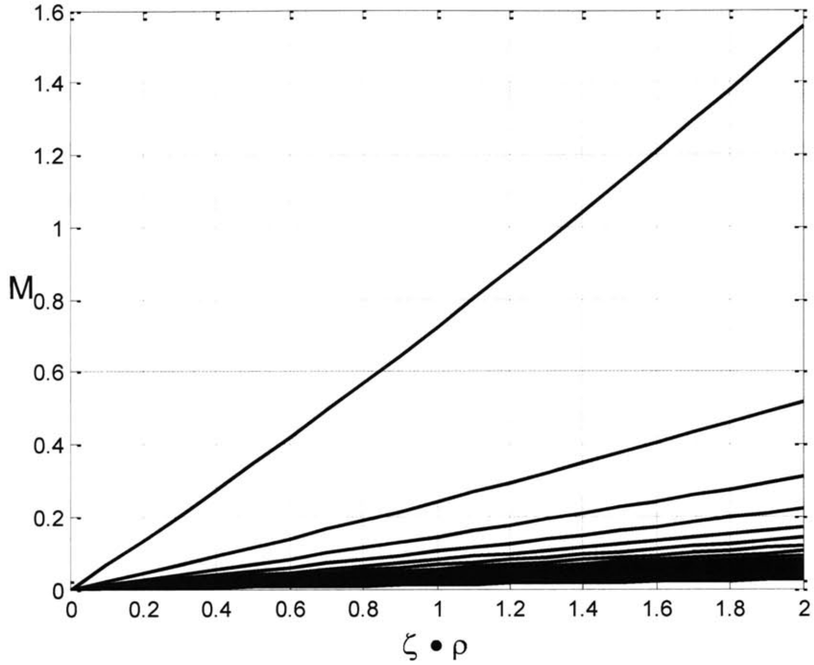

Figure 4-4: Ion Mach numbers vs. distance at various times. The top/fastest profile is at $t' = 0$.

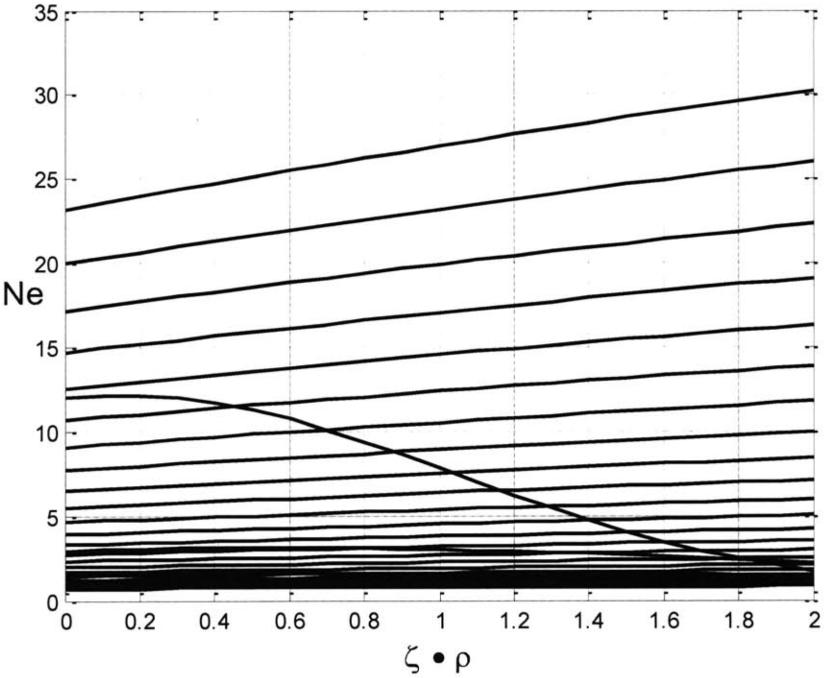

Figure 4-5: Plasma density vs. distance for various times. $t' = 0$ is the 'curvy' profile in the middle. The density dies off and then builds back up to the highest profile

4.2. Rapid Ionization Phase

At some time t^* (of the order of 16 for the example shown), ionization accelerates to the point of rendering the model as derived so far invalid, particularly by depleting the neutrals and stopping the ionization burst. The selection of t^* will be discussed later. At this point once an ionization burst takes off, it is reasonable to assume that the gradients cease to be dynamically significant, so that the governing equations reduce to Eqs. 4-57 and 4-58, which together imply the conservation law, Eq. 4-59.

$$\frac{\partial N_e}{\partial t'} = \left(\rho M_n N_n - \frac{1}{\delta}\right) N_e \tag{4-57}$$

$$\frac{\partial N_n}{\partial t'} = -\left(\rho M_n N_n - \frac{1}{\delta}\right) N_e \tag{4-58}$$

$$N_e(t',\zeta) + N_n(t',\zeta) = N_e(t^*,\zeta) + N_n(t^*,\zeta) = N_e^* + N_n^* \tag{4-59}$$

Here, the evolution is with time alone, and the distance ζ appears as a parameter only. Solving for N_e in Eq. 4-59 and substituting in Eq. 4-58 gives a separable ordinary differential equation for $N_n(t')$, which can easily be solved, and the result then substituted back to find $N_e(t')$. The result for N_n is:

$$N_n = \frac{N_e^* + N_n^* + N_e^* \dfrac{1/\delta}{\rho M_n N_n^* - 1/\delta} \exp[(\rho M_n(N_e^* + N_n^*) - 1/\delta)(t' - t^*)]}{1 + \dfrac{\rho M_n N_e^*}{\rho M_n N_n^* - 1/\delta} \exp[(\rho M_n(N_e^* + N_n^*) - 1/\delta)(t' - t^*)]} \tag{4-60}$$

N_e follows from Eq. 4-59. After a long time compared to the reference time, these formulae indicate the following limits. Eq. 4-61 and 4-62 are to be applied at all points (all values of ζ). It is interesting that, because of the wall losses, the ionization is incomplete at the end of the flash.

$$N_e(t' - t^* \to \infty) = N_e^* + N_n^* - \frac{1}{\delta\rho M_n} \tag{4-61}$$

$$N_n(t' - t^* \to \infty) = \frac{1}{\delta\rho M_n} \tag{4-62}$$

The result of Eq. 4-61 is shown in Figure 4-6, using $t^* = 16.2$ in the case presented in the previous figures. The value of t^* will be discussed in the next section.

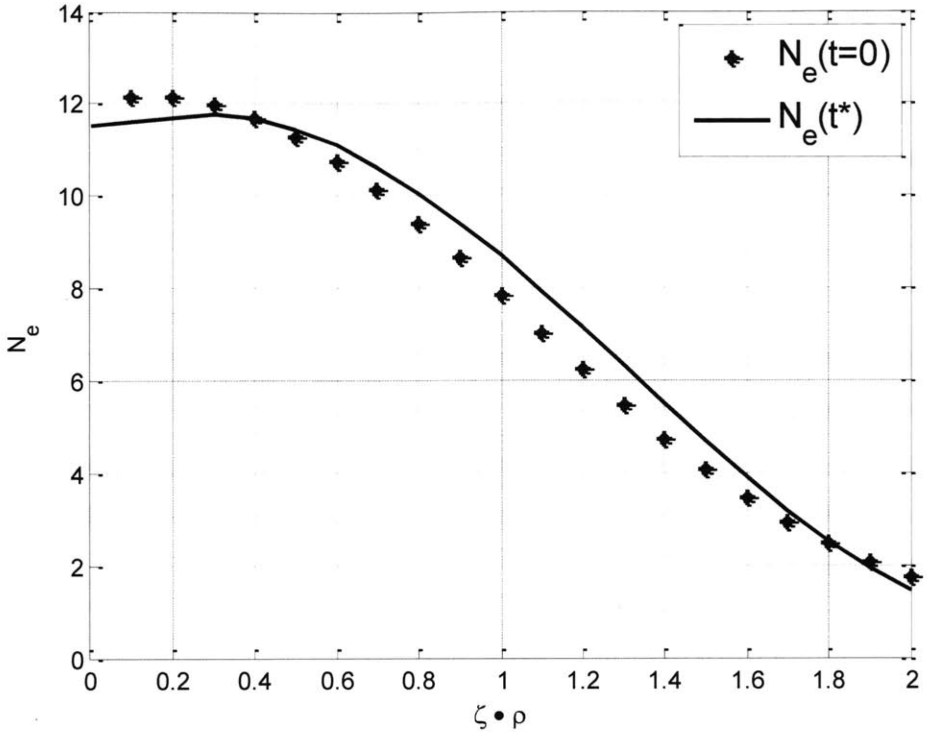

Figure 4-6: Comparison of density profiles after an ionization flash at $t^* = 16.2$ and at the initial time (which is also the start of the next period).

4.3. Selection of Parameters

There is a long list of parameters to be assigned numerical values for calculations. Of these, some are reasonably known a-priori, such as δ, ρ, ζ_a, and M_n. The initial leading edge location of the neutrals, λ, should be about $w/2$, but examination of several full solutions is needed to verify that this does represent the ionization "bite". Others, like χ_0 and b_{10}, that arise as integration constants in the derivation, require judicious choice. Finally, the time t^* at which rapid ionization occurs needs to be estimated as well.

4.3.1. Choice of b_{10}

Since b_1 is the initial slope of $M(\zeta)$, we select b_{10} from consideration of the ion Mach profile. At time $t' = 0$, we have Eq. 4-63 for the ion Mach number. Recall that $\zeta_a < 0$.

$$M_0 = b_{10}\left(1 + \frac{\zeta}{2\zeta_a}\right) \qquad \text{4-63}$$

A reasonable tentative choice is to make $M_0 = 1$ between $\zeta = 1/\rho$ and $\zeta = 2/\rho$, corresponding to one and two times the ionization distance. In the steady model example in Figure 3-11, it can be seen that $M = 1$ occurs near $\zeta = 1.1/\rho$. For now, we will choose $\zeta = 2/\rho$ to compute a reasonable value of b_{10}. This yields Eq. 4-64 which in turn yields $b_{10} = 0.6$ for the previous example ($\rho = 1$ and $\zeta_a = -6$). This is close to the value used, 2/3

$$b_{10} = \frac{\rho/2}{1 - \frac{1}{\rho(-\zeta_a)}} \qquad \text{4-64}$$

4.3.2. Choice of t^*, χ_0 and w

For periodicity, the end point of the rapid ionization phase should ideally reproduce the density profiles at $t = 0$. According to Eq. 4-61, this means

$$N_e^*(\zeta) + N_n^*(\zeta) - \frac{1}{\delta\rho M_n} = N_e(0,\zeta) \qquad \text{4-65}$$

Because of the approximations inherent in the theory, this will not be satisfied exactly, but we can at least aim for a good match of the density at the entry point $\zeta = 0$ and over the width of the plasmoid produced in the ionization flash. This approximate matching is shown in Figure 4-6. The width of the ionization flash will be mainly controlled directly by t^*, through the advancing neutral profile, since most of these neutrals will become ions in the flash. The density level at $\zeta = 0$ is also affected by t^*, because N_e is rapidly rising at some point, but it is affected also by the initial current level, χ_0. As shown before, χ_0 scales together with N_{e0}, so it tends to affect N_e^* directly, but because of the extra terms in Eq. 4-65, the effect on the match is not straightforward. Additionally, the width of the advancing neutral front, w, has a strong effect on the slope of the plasma density with respect to ζ throughout the width of the ionization region.

In the period when ionization starts to matter, two possible candidates suggest themselves for t^*:

a) The time t_1 at which the ionization/loss integral returns to positive values. In the sample calculation this is about $t_1 = 14.8$.
b) The time t_2 at which the current χ recovers to the initial value χ_0. In the example, this is about $t_2 = 18.16$.

The discussion above suggests a search in this interval for the best overall match. This can be done readily, and in the example we have been discussing, the best choice is found to be in the neighborhood of $t^* = 16.2$. The results are shown in Figure 4-6. The match is pretty good, although not perfect. Some observations could be made:

a) Changing the λ parameter, which shifts the initial position of the neutral front, has a strong effect, and the value of $w/2$ chosen appears to be nearly optimal.
b) The average current $\bar{\chi}$ can now be computed, and is found to be 0.342. This low value, together with the given ρ, does correspond, according to our steady state model, to the absence of a steady solution.

4.3.3. Choice of ζ_a

The parameter ζ_a is dependent on the diffusion region which is observed in Chapter 5. For the most part, this parameter mainly effects the resulting frequency of the oscillation because of the correlation between b_1 and t' in Eq. 4-35. This allows ζ_a to be loosely fit if the frequency of oscillation is not of interest. For now, the reader is referred to Chapter 5 for more details on the selection of this parameter.

4.4. Solution Method

The derivation of the transient model includes many equations which may make seeing how to get a solution confusing. In this section, a step by step procedure will be given for obtaining the solution.

1. We start by using ρ, δ, ζ_a and M_n corresponding to the operation point of a thruster we want to consider. The quantity ρ will include the effects of discharge voltage (T_e) and neutral flow rate.
2. The parameters χ_0, λ, w, and b_{10} will be tentatively selected for this solution and modified for subsequent solutions until $N_e(0,\zeta) \approx N_e(t^{*+},\zeta)$. b_{10} will have a strong influence on $M(t=0,\zeta)$ which should be set so $M_0 = 1$ between $\zeta = 1/\rho$ and $2/\rho$. λ will likely remain close

to $w/2$. To adjust the slope of the final plasma density profile, w can be adjusted. χ_0 has an effect on both the initial and final plasma density profiles.

3. Eq. 4-35 implicitly gives $b_1(t')$. Since approximately constant time steps are desirable, we start by using the approximate expression of Eq. 4-66 to select an appropriate grid of b_1 values. Eq. 4-35 is repeated here for convenience. Please note, that these equations are solved at discrete points.

$$b_1(t_{est}) = \frac{b_{10}}{1 + t_{est}} \qquad \text{4-66}$$

$$A \equiv \frac{\zeta_a^2}{3/2} \qquad r^+ = b_1 + \frac{1}{2} + \sqrt{\frac{1}{4} - \frac{1}{A}} \qquad r^- = b_1 + \frac{1}{2} - \sqrt{\frac{1}{4} - \frac{1}{A}}$$

$$t' = \frac{1 - \frac{A}{4}}{r^+ - r^-} \ln\left(\frac{r^+}{r^-}\frac{r_0^+}{r_0^-}\right) + \frac{A}{4}\ln\left(\frac{r^+ r^-}{b_1^2}\frac{b_{10}^2}{r_0^+ r_0^-}\right) \qquad \text{4-35}$$

4. Next, we take each discrete t' and perform the calculations indicated in Eqs. 4-53 through 4-56, repeated below. Recall $t_n' = \rho M_n t'$.

$$I_0 = \frac{\lambda(w^4 - w^3\lambda + w\lambda^3/2 - \lambda^4/5)}{2\,w^3} - \frac{(w-1)(w^3 + w(w-1)^3/2 - (w-1)^4/5)}{2\,w^3} \qquad \text{4-53}$$

For $t_n' < \lambda + 1 - w$

$$\int_0^{t'} I\,dt' = -\frac{1}{\delta}t' + \frac{1}{M_n}\left[\frac{w}{2}t_n' - \frac{\lambda^2 - (\lambda - t_n')^2}{2} + \frac{\lambda^4 - (\lambda - t_n')^4}{4\,w^2} - \frac{\lambda^5 - (\lambda - t_n')^5}{10\,w^3}\right] \qquad \text{4-54}$$

For $\lambda + 1 - w < t_n' < \lambda + 1$

$$\int_0^{t'} I\,dt' = -\frac{1}{\delta}t' + \frac{1}{M_n}\left[I_0 + w - 1 + t_n' - \lambda - \frac{w^4 - (\lambda + 1 - t_n')^4}{4\,w^2} + \frac{w^5 - (\lambda + 1 - t_n')^5}{10\,w^3}\right] \qquad \text{4-55}$$

For $t_n' > \lambda + 1$

$$\int_0^{t'} I\,dt' = -\frac{1}{\delta}t' + \frac{1}{M_n}\left[I_0 + w - 1 + t_n' - \lambda - \frac{3}{20}w^2\right] \qquad \text{4-56}$$

5. Now use Eq. 4-40 to compute $\ln(\chi/\chi_0)$. Computing N_{e0} is not necessary because the simple relationship of Eq. 4-30 can be used within equations later.

$$\ln\left(\frac{N_{e0}}{N_{e0,0}}\right)=\ln\left(\frac{\chi}{\chi_0}\right)=\int_0^{t'} I(t'')dt''+\ln\left(\frac{b_1^2+b_1+\frac{1}{A}}{b_{10}^2+b_{10}+\frac{1}{A}}\right) \qquad \text{4-40}$$

$$N_{e0}(t')=(-\zeta_a)\chi(t') \qquad \text{4-30}$$

6. Now b_2 is either computed at each time or Eq. 4-32 is plugged into the later equations.

$$b_2=\frac{-b_1}{2(-\zeta_a)} \qquad \text{4-32}$$

7. Now make a set of discrete values of ζ (probably from 0 to $2/\rho$) and use Eq. 4-13 to compute $M(t',\zeta)$.

$$M(t',\zeta)\approx b_1(t')\zeta+b_2(t')\zeta^2 \qquad \text{4-13}$$

8. Now solve Eq. 4-11 for across ζ at each t'. This equation is easily solved numerically. Adaptive quadrature methods work very well with the integral when the μ inside the integral is used as a function of the exponent of Eq. 4-15. For the μ outside the integral, use $\mu=\exp(\ln(\mu))$ evaluated at the discrete points. As an alternative to Eq. 4-11, Eq. 4-20 can be solved analytically. However, Eq. 4-20 varies from Eq. 4-11 by the time ζ reaches 2.

$$N_e=\frac{1}{\mu(\zeta)}\left[N_{e0}+\chi\int_0^{\zeta}\mu(\zeta')d\zeta'\right] \qquad \text{4-11}$$

$$\ln\mu(\zeta)\approx\frac{b_1}{2}(1+b_1)\zeta^2+\frac{b_2}{3}(1+3b_1)\zeta^3+\frac{1}{2}b_2^2\zeta^4 \qquad \text{4-15}$$

9. The neutral profiles are computed with Eqs. 4-44 through 4-47.
10. Now t^* is estimated as a weighted average of t_1 and t_2, the time when the $\exp(I)$ turns positive and the time when $\chi=\chi_0$ again. It is recommended to use 30 to 40 percent t_1 for most cases. Once t^* is estimated, the rapid ionization event occurs and Eq. 4-61 will be used to compute the final profile.

$$N_e(t' - t^* \rightarrow \infty) = N_e^* + N_n^* - \frac{1}{\delta \rho M_n} \quad 4\text{-}61$$

11. The final plasma density profile should now be compared to the initial plasma density profile. If the match is not good, this process should be repeated with different parameters. If an exhaustive search cannot produce a good match, it is hypothesized that this corresponds to thruster extinguishment.

4.5. Example of Transient Model Application

The transient model will be applied to some of the data points for the SPT-100 collected by Gascon et al. shown in section 3.5.1 and 3.5.2[3]. Table 4-1 shows data points from the varying discharge potential dataset. Table 4-2 shows the data points from the varying magnetic field dataset. Three data points will be used from each dataset, one point for when the steady model and experiment agree for steady cases, one for agreement with unsteady cases, and one for a disputed data point. The transient model cannot reproduce steady behavior, but steady data points will still be used to further explore the transient model.

The transient model is then solved to get a close match for the beginning and ending plasma density profiles. Due to the assumptions of this model, a perfect match of the beginning and ending plasma density profiles should not be expected. The profile match in Figure 4-6 was shown as what can be achieved in a good case. Figure 4-7 and Figure 4-8(a) show what was achieved for Cases 1 and 5, respectively. Note that the profile match in Case 1 is worse than normal, but is explained below due to the thruster's off-nominal conditions. The profile matches used are the best profile matches that have been found for each condition that still give a reasonable ion Mach number distribution.

After the transient model is solved, the time-averaged current, χ_{avg}, is found. It is interesting to note that although the transient model cannot reproduce steady behavior, it can still give solutions where χ_{avg} is very similar to the experimental χ in all cases. The match between χ_{avg} and the experimental χ is closer for cases where the experimental mode observed was periodic, but the match is still close for experimentally steady cases examined.

In some cases there are multiple fits that are close where one fit yields a time-averaged χ that corresponds to a steady-model-predicted steady solution and another corresponds to a steady-model-predicted periodic solution. In these cases, care was taken to use the case that was marginally better. One of these situations occurred with Case 5 in Table 4-2 and Figure 4-8. This case has a coil current of about 3.7 A. As can be seen in Figure 3-17, this data point is where the thruster transitions from a higher current oscillatory mode to a lower current steady mode. In this case, the lower current solution was a little better, Figure 4-8(a). The other solution, Figure 4-8(b) had a current similar to the higher current mode as seen in Figure 3-17.

In case 1, λ was adjusted greatly in order to produce a profile matching. In this case, the discharge potential is very low, not in the standard range of discharge potentials used for the SPT-100. Perhaps the thruster is operating in a different mode, requiring λ to be adjusted. Although the thruster is operating at a low voltage and the profile match shown in Figure 4-7 is not the best, the transient model, is still able to accurately predict a current and predict that the thruster is operating periodically.

Table 4-1: Transient Model Results for the SPT-100 Varying Discharge Potential Cases with $\beta = 16$.

	Case 1	Case 2	Case 3
Discharge Potential (V)	125	250	350
Steady Model Prediction using experimental χ	Unsteady	Steady	Steady
Experimental Result	Periodic	Steady	Periodic
Experimental χ	1.23	1.09	1.12
δ	0.835	0.58	0.495
ρ	1.53	9.82	18.18
M_n	0.12	0.0835	0.0709
ζ_a used	-6	-5	-5
w	2	2.2	2.3
λ	w/25	w/2	w/2
χ_0	1.8	3.6	3.2
b_{10}	0.893	8.838	18.18
χ_{avg}	1.22	1.28	1.13

Table 4-2: Transient Model Results for the SPT-100 Varying Magnetic Field Cases with $\beta = 65$.

	Case 4	Case 5	Case 6
Coil Current (A)	3.5	3.7	5.1
Steady Model Prediction using experimental χ	Unsteady	Steady	Unsteady
Experimental Result	Periodic	Steady	Steady
Experimental χ	1.35	1.17	1.12
δ	1.68	1.77	2.40
ρ	4.42	4.19	3.1
M_n	0.0758	0.0758	0.0758
ζ_a used	-6	-6	-6
w	2	2	2
λ	w/2	w/2	w/2
χ_0	3.1	2.9	2.9
b_{10}	3.315	3.492	2.583
χ_{avg}	1.36	1.20	1.21

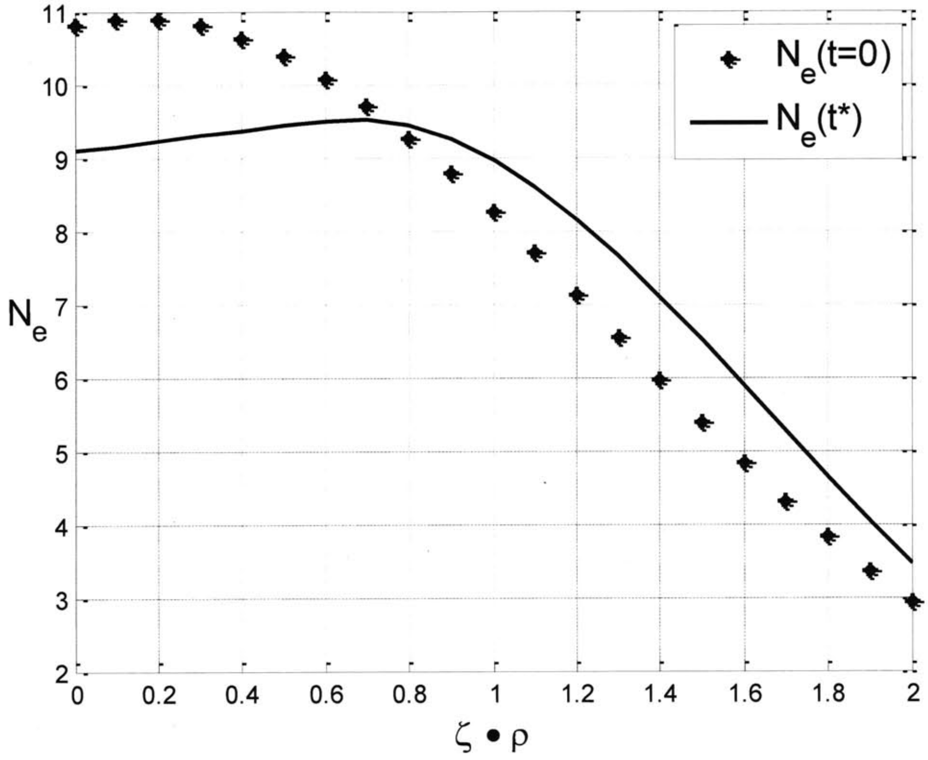

Figure 4-7: Plasma density profile match for case 1.

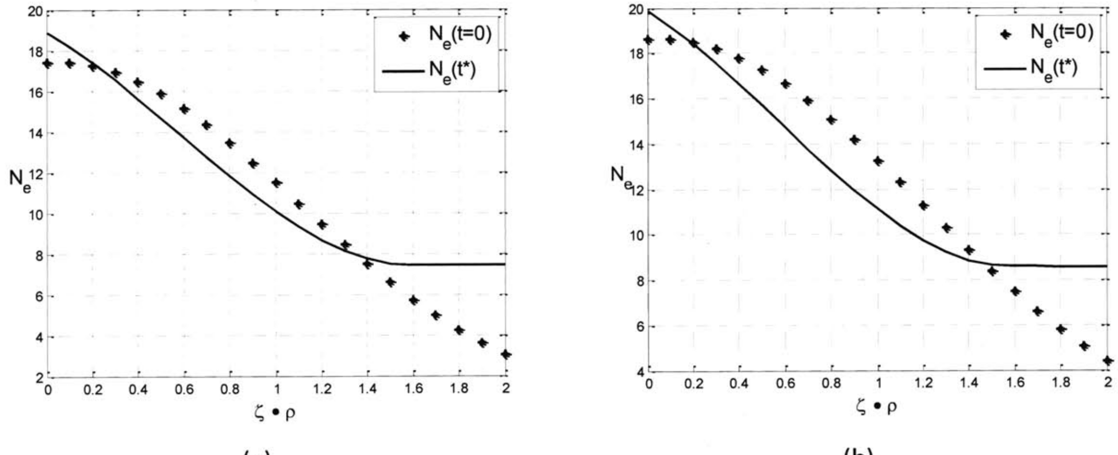

(a)

(b)

Figure 4-8: (a) Plasma density profile match for case 5 with χ_{avg} predicting a steady solution in steady model limits. (b) Marginally worse profile match for case 5 resulting in a χ_{avg} that predicts non-steady in the steady model limits.

4.6. Transient Model Discussion

As shown, the transient model is able to give insight into the periodic nature of an oscillating Hall thruster. It has shown that a periodic solution is possible for the several SPT-100 data points tested above and has shown that the current resulting from a transient solution actually corresponds to that of a steady solution for some of those data points. Finding the solution for the transient model, however, is currently time consuming, mostly due to the subjective nature of which solution is better.

The current method for determining if there is no periodic solution is to exhaustively search the parameters to prove that no solution can be found. If this was a feasible task, it would suggest that such conditions result in thruster extinguishment. More work is needed on this model because a better method for determining if no periodic solution exists is needed.

Similar to the steady model, the transient model also requires a user to input the electron temperature in the ionization region. Experienced users can make good guesses about this temperature in well-known thrusters, but another model will be necessary to estimate this temperature for new thrusters and thrusters still in the design phase.

Chapter 5

Anode Depletion Model

If the anode is starved of electrons, the thruster will extinguish. This gives a limit on thruster operation which will be explored. The region between the anode and the ionization region is important in this chapter. This region is called the diffusion region. Here, the magnetic field and electron temperature cannot be considered constant. It is unknown how and if the effective hall parameter varies throughout this region, so it will be formulated to allow variation.

Allowing the new variable quantities creates changes in the non-dimensionalized steady equations from before with the addition of the energy equation, resulting in the following. In this section, these equations are non-dimensionalized with the conditions where the electron density is maximum.

$$\frac{\partial(N_e M_e)}{\partial\zeta} = \tilde{R}\rho M_n N_n N_e - \frac{N_e}{\delta}\tilde{T}_e^{1/2} \tag{5-1}$$

$$\frac{\partial(N_e M)}{\partial\zeta} = \tilde{R}\rho M_n N_n N_e - \frac{N_e}{\delta}\tilde{T}_e^{1/2} \tag{5-2}$$

$$M_n\frac{\partial(N_n)}{\partial\zeta} = -\tilde{R}\rho M_n N_n N_e + \frac{N_e}{\delta}\tilde{T}_e^{1/2} \tag{5-3}$$

$$M_e = -\frac{1}{\tilde{\beta}\tilde{B}}\left(\hat{E}_z + \frac{1}{N_e}\frac{\partial\left(N_e\tilde{T}_e\right)}{\partial\zeta}\right) \tag{5-4}$$

$$\frac{d}{d\zeta}\left(N_e M_e \frac{5}{2}\tilde{T}_e\right) = -N_e M_e \hat{E}_z - \tilde{R}\rho M_n N_n N_e \tilde{\varepsilon}_i - \frac{N_e}{\delta}\tilde{T}_e^{3/2}\tilde{\varepsilon}_w \tag{5-5}$$

The following non-dimensionalized quantities were used where the subscript *i* refers to values at the the maximum electron density.

$$\tilde{R} = \frac{R_i(T_e)}{R_i(T_{ei})} \qquad \tilde{T}_e = \frac{T_e}{T_{ei}} \tag{5-6}$$

$$\tilde{\beta} = \frac{\beta}{\beta_i} \qquad \tilde{B} = \frac{B}{B_i} \tag{5-7}$$

$$\tilde{\varepsilon}_i = \frac{\varepsilon_i \alpha_i}{T_{ei}} \qquad \tilde{\varepsilon}_w = \frac{\varepsilon_w}{T_e} = \frac{\varepsilon_w}{T_{ei}\tilde{T}_e} \tag{5-8}$$

Current conservation remains valid.

$$N_e(M - M_e) = \chi(t') \tag{5-9}$$

An additional relation used in this chapter is a relation between the beam current and the maximum plasma density. It is shown below and then non-dimensionalized. η_c is the current efficiency which normally ranges between 0.6 and 0.9.

$$\frac{j}{e} = \frac{I_a}{I_B}\frac{I_B}{eA} \approx \frac{1}{\eta_c} n_{e,max} v_{B,ion} \exp\left(-\frac{1}{2}\right) \tag{5-10}$$

$$\chi \approx \frac{1}{\eta_c} N_{e,max} \exp\left(-\frac{1}{2}\right) \qquad N_{e,max} \approx \frac{\chi \eta_c}{\exp(-1/2)} \tag{5-11}$$

5.1. Simple Diffusion Model

First, a very simple diffusion model will be formulated. Big assumptions are made here to achieve a very simple model. In the diffusion region, the current is assumed to be entirely made up by the electron flux and the electric field is assumed small. This reduces the above system of equations down to one equation resulting from Eqs. 5-4 and 5-11.

$$\chi = \frac{1}{\tilde{\beta}\tilde{B}} \frac{\partial\left(N_e \tilde{T}_e\right)}{\partial \zeta} \tag{5-12}$$

This is integrated from the anode to the point of maximum electron density. The point of maximum electron density might be a good approximation for the start of the ionization region, but a relation between the two points may be required to find more exact values for ζ_a (a quantity from the transient model in Chapter 4). The integration yields the following where f_0 is a shape factor and ζ_{ia} is the distance between the anode and the point of maximum electron density. The subscript *i* refers to the point of maximum electron density which is roughly the point where ionization starts to matter. The subscript *a* refers to the anode.

$$\left(N_e\tilde{T}_e\right)_i - \left(N_e\tilde{T}_e\right)_a = \chi f_0 \zeta_{ia} \tag{5-13}$$

$$f_0 \equiv \int_0^1 \tilde{\beta}\tilde{B}\, d\left(\frac{\zeta}{\zeta_{ia}}\right) \tag{5-14}$$

The limiting case of this expression is when the electron density at the anode goes to zero. To operate, the density has to be greater than zero, resulting in the following limit. Note that $\tilde{T}_{ei} = 1$.

$$\chi f_0 \zeta_{ia} < N_{e,max} \tag{5-15}$$

Eq. 5-11 is then used and the equation is rearranged.

$$\zeta_{ia} < \frac{1}{f_0} \frac{\eta_c}{\exp(-1/2)} \tag{5-16}$$

This gives a limit for avoiding anode depletion. Big assumptions were made to obtain this results. Next, another model will be formulated, but with a few less assumptions.

5.2. Diffusion Region Model

In this model, we neglect ionization and only consider the part of the diffusion region in which ionization is not important, the region between the anode and the point of maximum electron density. The ion flux is considered small, allowing the assumption that the current is made up of mostly the electron flux. This results in a constant electron flux. The low flux of ions implies that the potential is relatively constant throughout the diffusion region, allowing the electric field to be neglected. Additionally, the pre-sheath is neglected. This reduces the governing equations to the following.

$$\chi = \frac{1}{\tilde{\beta}\tilde{B}}\frac{\partial\left(N_e\tilde{T}_e\right)}{\partial\zeta} \qquad \text{5-17}$$

$$\frac{d}{d\zeta}\left(\chi\frac{5}{2}\tilde{T}_e\right) = \frac{N_e}{\delta}\tilde{T}_e^{3/2}\tilde{\varepsilon}_w \qquad \text{5-18}$$

The first equation is integrated from *a* to ζ, the anode to a generic point. In this analysis, the anode is taken to be zero. The second equation is rearranged. The $2N_{ea}$ is used to make up for neglecting the pre-sheath.

$$N_e\tilde{T}_e = 2N_{ea}\tilde{T}_{ea} + \chi\int_0^\zeta \tilde{\beta}\tilde{B}\,d\zeta \qquad \text{5-19}$$

$$N_e = \frac{5}{2}\frac{\chi\delta}{\tilde{\varepsilon}_w}\frac{1}{\tilde{T}_e^{3/2}}\frac{d\tilde{T}_e}{d\zeta} \qquad \text{5-20}$$

These equations are combined to give:

$$\frac{5}{2}\frac{\chi\delta}{\tilde{\varepsilon}_w}\frac{1}{\tilde{T}_e^{1/2}}\frac{d\tilde{T}_e}{d\zeta} = 2N_{ea}\tilde{T}_{ea} + \chi\int_0^\zeta \tilde{\beta}\tilde{B}\,d\zeta \qquad \text{5-21}$$

This equation is integrated from *a* to ζ.

$$5\frac{\chi\delta}{\tilde{\varepsilon}_w}\left(\tilde{T}_e^{1/2} - \tilde{T}_{ea}^{1/2}\right) = 2N_{ea}\tilde{T}_{ea}\zeta + \chi\int_0^\zeta (\zeta-\zeta')\left(\tilde{\beta}\tilde{B}\right)_{\zeta'} d\zeta' \qquad \text{5-22}$$

Eqs. 5-19 and 5-22 are then evaluated at *i*, the point of maximum electron density.

$$N_{e,max} = \frac{\chi\eta_c}{\exp(-1/2)} = 2N_{ea}\tilde{T}_{ea} + \chi\zeta_{ia}f_0 \qquad \text{5-23}$$

$$5\frac{\chi\delta}{\tilde{\varepsilon}_w}\left(1 - \tilde{T}_{ea}^{1/2}\right) = 2N_{ea}\tilde{T}_{ea}\zeta_{ia} + \chi\zeta_{ia}^2[f_0 - f_1] \qquad \text{5-24}$$

$$f_0 \equiv \int_0^1 \tilde{\beta}\tilde{B}\,d\left(\frac{\zeta}{\zeta_{ia}}\right) \qquad f_1 \equiv \int_0^1 \left(\frac{\zeta}{\zeta_{ia}}\right)\tilde{\beta}\tilde{B}\,d\left(\frac{\zeta}{\zeta_{ia}}\right) \qquad \text{5-25}$$

Now, Eqs. 5-11 and 5-23 are combined to give:

$$\frac{2N_{ea}}{N_{e,max}} = \frac{1 - \frac{\exp(-1/2)}{\eta_c} f_0 \zeta_{ia}}{\tilde{T}_{ea}} \tag{5-26}$$

Eq. 5-24 is now added in for T_{ea} and Eq. 5-23 is added back in for $N_{ea}T_{ea}$:

$$\frac{2N_{ea}}{N_{e,max}} = \frac{1 - \frac{\exp(-1/2)}{\eta_c} f_0 \zeta_{ia}}{\left[1 - \frac{\tilde{\varepsilon}_w}{5}\left(\frac{\eta_c}{\exp(-1/2)} \frac{\zeta_{ia}}{\delta} - f_1 \frac{\zeta_{ia}^2}{\delta}\right)\right]^2} \tag{5-27}$$

This equation can be re-dimensionalized to reveal that it depends on combinations of different characteristic lengths; the channel width, the characteristic diffusion length, and the distance between the anode and the maximum electron density.

$$\frac{2n_{ea}}{n_{e,max}} = \frac{1 - \frac{\exp(-1/2)}{\eta_c} f_0 \left(\frac{l_{ia}}{l_{diff}}\right)}{\left[1 - \frac{(\varepsilon_w/T_e)}{5}\left(\frac{2\eta_c}{\exp(-1/2)} \frac{l_{ia}}{h} - f_1 \frac{l_{ia}^2}{h\, l_{diff}}\right)\right]^2} \tag{5-28}$$

The limiting case is when the density at the anode is zero. This gives the limit where the right hand side must be greater than zero which requires the numerator to be greater than zero. This results in the same limiting case as the simple diffusion model in the previous section.

$$\zeta_{ia} < \frac{1}{f_0} \frac{\eta_c}{\exp(-1/2)} \tag{5-29}$$

If this limit is violated, the thruster should extinguish because no plasma will reach the anode. It is important to remember that a few large assumptions were made to achieve this result, however, an initial comparison to numeric data on the relations between $n_{ea}/n_{e,max}$ given in Eq. 5-27 and the characteristic lengths shows promising results. The results predict a $n_{ea}/n_{e,max}$ that is close to what is observed numerically. Additional comparison is needed to determine if Eq. 5-29 is accurate.

Chapter 6

Boron Nitride Depth Markers

Erosion measurements of the Boron Nitride ceramic channel walls within Hall thrusters has historically been expensive. Such measurements are important as a way to experimentally determine the erosion rate of Boron Nitride under different circumstances and different locations in different Hall thrusters. If these measurements can be made at any location, the lifetime of the thruster will be able to be better predicted without full-life testing and better design decisions may be made.

6.1. Background

In a conjunction between MIT's Plasma Science and Fusion Center (PSFC) and MIT's Space Propulsion Laboratory (SPL), a new method of measuring erosion within Boron Nitride (and other materials) has been developed. For a more detailed description of the technique, see Ref. 26. The method is implanting a layer of Lithium within the Boron Nitride. The depth of the Lithium can be measured before and after an erosion event to find the total erosion. The author contributed to this work by eroding Boron Nitride samples placed in a plume of a Hall thruster while the researchers at PSFC implanted and measured the depth of the Lithium.

To implant the Lithium, a mono-energetic Lithium ion beam is fired at the Boron Nitride. The Lithium ions penetrate to a depth corresponding to their energy and then get trapped within the Boron Nitride. The beam is fired at the Boron Nitride for a time to give a desired Lithium concentration. Tests have confirmed that the position of the peak in Lithium concentration does not move even when the Boron Nitride is heated.

To measure the concentration of Lithium at a given depth a nuclear reaction analysis (NRA) is performed. A mono-energetic Hydrogen ion beam is fired at the Boron Nitride. The energy of the beam is set to allow the beam to penetrate to the desired depth. If there is Lithium at this depth, there is a chance that a proton from the beam will collide and fuse with the Lithium, causing an alpha decay. The alpha particle can then be detected if it flies off in the direction of a sensor. As this is repeated at different depths (beam energies) the different alpha particle counts give the Lithium concentration profile. Additionally, a Rutherford backscattering spectrometry is performed to detect any impurities in the surface. Taking the impurities into account allows the true depth of the Lithium to be determined. The NRA and RBS are repeated before and after erosion to determine the amount of erosion.

6.2. Sample Testing

As an initial test, 1 cm diameter cylindrical samples were implanted with Lithium and eroded in the plume of a BHT-200. The author contributed to this by eroding the samples after PSFC implanted them and then returning them to PSFC for analysis. The tests were conducted in SPL's 1.6m diameter x 2.8m vacuum chamber, Astrovac. Two cryopumps provide about 7500 L/s of pumping capacity to the chamber. Background pressures during the tests were about 45 to 50 microtorr with a IGM-401 Hornet hot cathode vacuum gauge. Grade 5 (99.999% pure) Xenon was used during for testing and two OMEGA FMA-6502-ST-XE regulated the flow of Xenon.

The BHT-200 was operated with an anode flow of 8.6 sccm, cathode flow of 1.0 sccm, anode potential of 250 V, keeper current of 0.5 A, magnet current of 1.0 A, and a heater current of 3.0 A. Figure 8(a) from a paper by Nakles et al. gave us the expected ion current flux at different positions in the plume[27]. During tests, the thruster was allowed to heat up for at least 30 minutes before moving the sample into the plume.

The samples were moved on the rotary stage described in section 4.2.3 of Boulanger's Thesis[28]. This stage allows movement of samples and/or sensor in the theta and radial directions. To mount the samples to the stage, a Boron Nitride cylinder was mounted to the stage and the sample was mounted to the Boron Nitride cylinder. This kept the conductive aluminum a little further from the sample to disrupt the plume less. A thermocouple was attached to the Boron Nitride cylinder to give the temperature of the sample. Due to Boron Nitride's relatively high thermal conductivity, it was assumed that the Boron Nitride cylinder would be close in temperature to the sample. Figure 6-2 shows the rotary stage and BHT-200 inside Astrovac. Figure 6-3 shows a sample mounted. Figure 6-4 shows a close up of a Lithium implanted Boron Nitride Sample. As a side note: when Lithium is implanted into the Boron Nitride, the color of the Boron Nitride changes to a black color where the Boron Nitride was implanted. This is not yet fully understood, but can be seen in Figure 6-4. The white spot on the otherwise black face of the sample is where mounting clips covered the face during Lithium implantation.

6.3. Results

The preliminary findings of the erosion of two samples will be presented. Both samples had Lithium implanted to a depth of 5.5 micrometers and were both placed on axis, 15.7 cm from the exit of the BHT-200. At this position, an ion current flux of 100 A/m^2 is expected[27]. The first sample was eroded for 15 minutes and the second sample was eroded for 120 minutes. Both samples started at room temperature and saw an increasing temperature throughout the test. The temperature peaked at 387 K and 443 for the first and second test, respectively. Figure 6-1 shows the temperature vs. time for the two tests. Figure 6-5 shows the sample in the plume of the BHT-200.

The NRA and RBS on the two samples, performed by the PSFC team, revealed that the first sample eroded 0.23 micrometers over its 15 minute exposure and the second sample eroded 1.38 micrometers over its 120 minute exposure. Additionally, both samples were found to have been contaminated with Tungsten. Tungsten is a common material in electric propulsion. In this test setup, it was found in the neutralizing cathode, the Busek BHT-1500, a Barium Oxide impregnated cathode that contain porous Tungsten. The first sample had a 0.3% Tungsten concentration at the surface that diffused about 1.1 micrometers into the surface. The second sample had about a 1.2% Tungsten concentration at the surface that diffused about 2.8 micrometers into the surface.

As noted, the results shown are preliminary. There is interest in performing X-ray photoelectron spectroscopy (XPS) on the samples to obtain a better measurement of the tungsten contamination on the surface. This would likely change the reported erosion measurements because a different tungsten contamination profile would change the penetration depth of the hydrogen ion beam.

These tests show promising results for this method of measurement. Since Boron Nitride erosion has historically been hard to measure, it is not easy to find other experimental Boron Nitride erosion data to compare the data too, but there are some facts known about Boron Nitride erosion. One of these facts is that the surface of Boron Nitride gets damaged by absorbing moisture in the atmosphere. This damaged layer should erode faster than the rest of the sample. This may explain why the measured erosion for the 120 minute is not 8 times larger than that of the 15 minute exposure. However, it is not known how thick this layer is or how much faster it erodes.

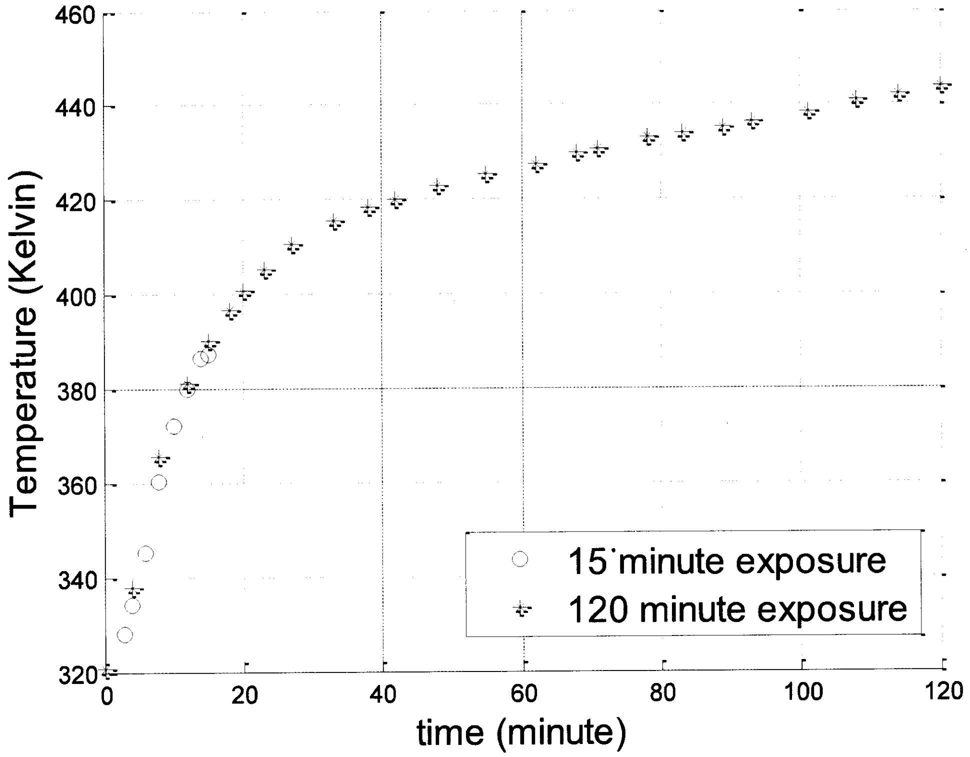

Figure 6-1: Temperature of Lithium implanted Boron Nitride during exposures

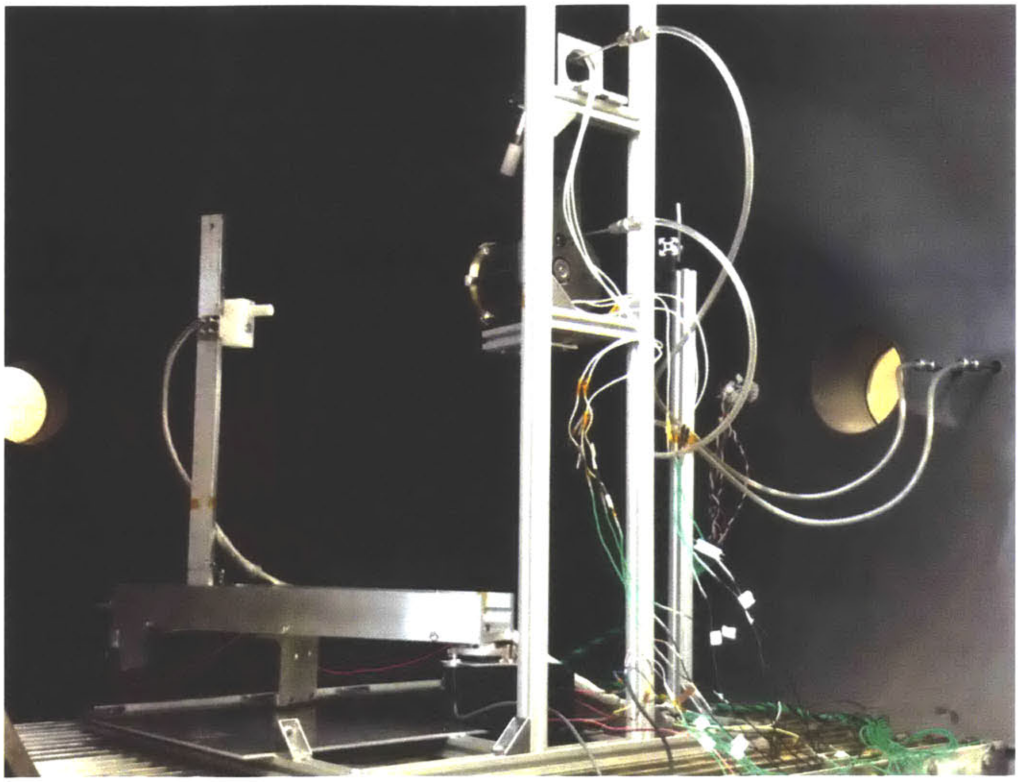

Figure 6-2: BHT-200 and rotary stage in Astrovac. No sample mounted

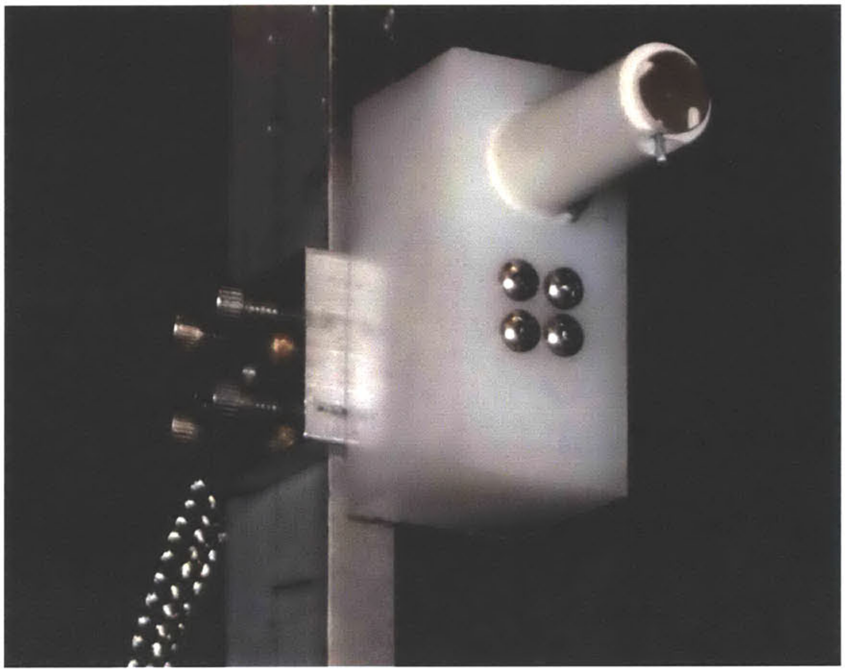

Figure 6-3: Lithium implanted Boron Nitride sample mounted

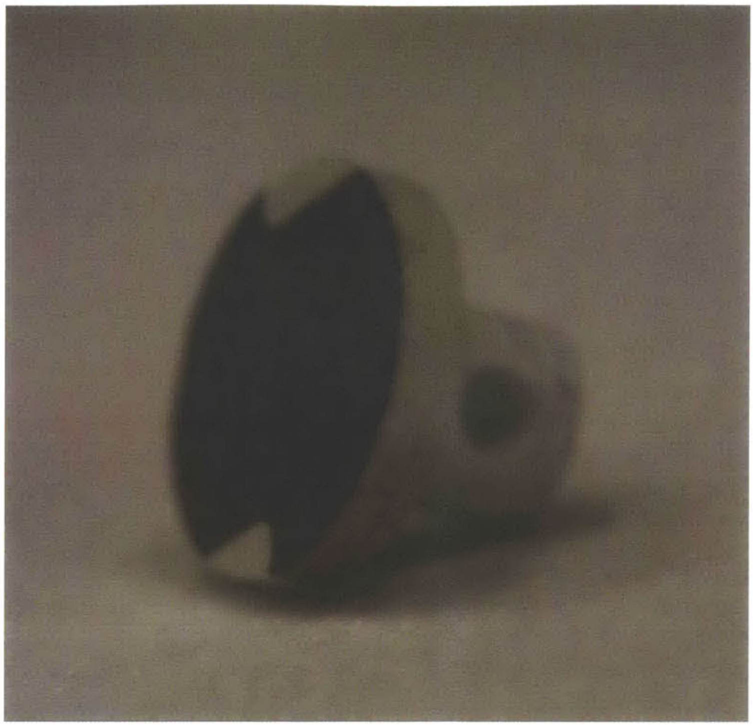

Figure 6-4: Lithium implanted Boron Nitride sample close-up

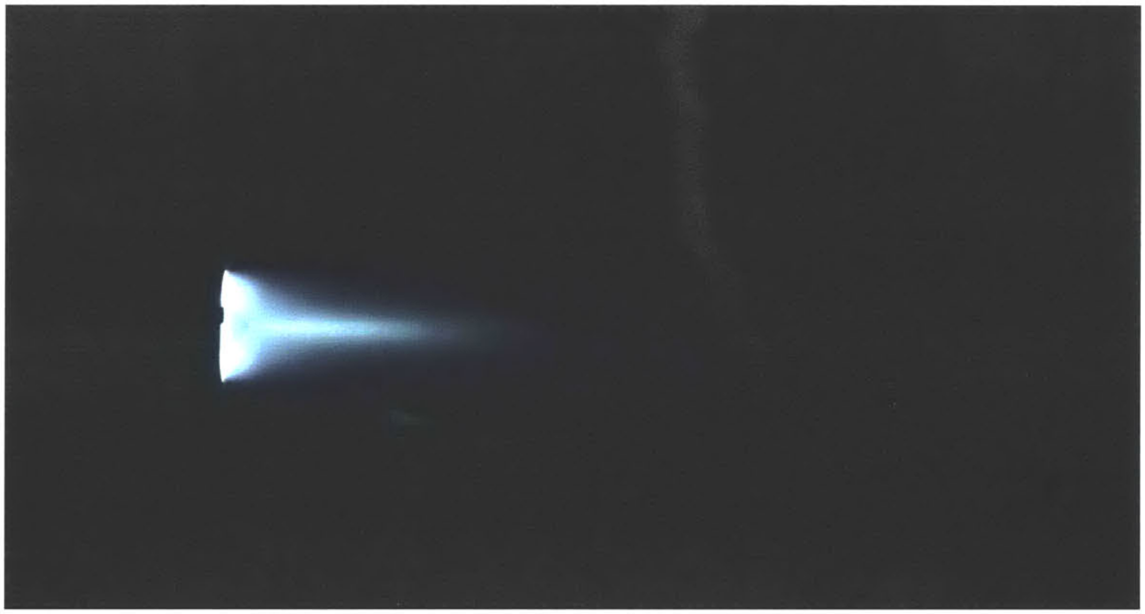

Figure 6-5: Lithium implanted Boron Nitride sample (right) in BHT-200 (left) plume

Chapter 7

Recommendations for Future Work

In this section the author's recommendations for future work will be presented.

7.1. Temperature Model

The steady model and transient model presented, both require the user to select the temperature in the ionization region. The development of a simple model that approximates this temperature would help the model account for off nominal voltages where the electron temperature is not well known. Complex models already exist that can completely solve the thruster, but a simple model is desired to facilitate investigation of limits of steady and periodic behavior. In such a model the wall losses will probably need to be included because in more complex models without wall losses the electron temperature is over-estimated[29].

7.2. Conceptual Difficulties of the Transient Model

Further exploration of the transient model should be performed to search for limits of the periodic solution. The current transient model assumes the oscillations are very strong. Weaker oscillations have not yet been explored.

As is, the transient model is conceptually difficult. The presence of two distinct phases makes finding limits difficult. Work should be performed to simplify the model into a single phase, if possible. The original intent of the model was to explore what happens outside of the smooth sonic passage limits. A possible way forward is to examine the behavior of the thruster within a numeric solution to the transient equations of motion. The transient equations of motion can probably be simplified with some of the results of the current transient equation to create a simpler numeric code. One such simplification is given in Eq. 7-1 where the derivative is evaluated at the entrance to the ionization region, where ions of zero velocity. Within the smooth sonic passage limits, it is predicted that perturbations to such a model would decay back to the steady model. Outside of the limits, it is of interest to learn what the behavior is. Examining the numeric behavior like this may reveal different behavioral regimes that correspond to the different limits found in the steady model.

$$\chi(t') = \frac{\partial N_e}{\partial \zeta}(t', \zeta = 0) \tag{7-1}$$

A numeric transient model is conceptually easier to understand and also allows verification of the steady. Additionally, a numeric transient model, when simplified and coupled with the understanding of the steady model offers a way forward to create a thruster controller.

7.3. Thruster Controller

An interesting use of the steady model is using it to create a thruster controller that will modify the thruster conditions to keep it in the steady regime. Such a controller would know the trends revealed by the steady model. As the thruster erodes through its life, the controller would be able to make adjustments if it noticed thruster conditions drifting into the unsteady regime. Alternatively, if oscillations occurred the controller would detect them and adjust the conditions to move back within the steady limits.

Due to limited knowledge of some plasma phenomena, the controller would likely need to be programmed with the trends of the model and be able to make educated decisions as it learns where the actual limits to steady behavior are.

As mentioned above, if a new numeric transient model is created, this offers a new way forward for a thruster controller allowing faster responses than a controller based on the steady model. A controller using a new numeric transient model would likely implement control through varying the discharge potential because any other modifications have long time delays associated with them (i.e. magnetic field and mass flow rate modification). Varying the discharge potential effects the electron temperature which modifies ρ, hopefully allowing a controller to quickly move the conditions into a steady regime.

References

1. Gildea, S. R. Development of the Plasma Thruster Particle-in-Cell Simulator to Complement Empirical Studies of a Low-Power Cusped-Field Thruste. (2012).

2. Gildea, S. R., Matlock, T. S. & Martinez-Sanchez, M. Erosion Measurements in a Diverging Cusped-Field Thruster. 1–20 (2011).

3. Gascon, N., Dudeck, M. & Barral, S. Wall material effects in stationary plasma thrusters. I. Parametric studies of an SPT-100. *Phys. Plasmas* **10,** 4123 (2003).

4. Yamamoto, N., Nakagawa, T., Komurasaki, K. & Arakawa, Y. Observation of Plasma Fluctuations in Hall Accelerators.

5. Matlock, T. S. & Martinez-Sanchez, M. An Exploration of Prominent Cusped-Field Thruster Phenomena : The Hollow Conical Plume and Anode Current Bifurcation. (2012).

6. Fife, J., Martinez-sanchez, M. & Szabo, J. A numerical study of low-frequency discharge oscillations in Hall thrusters. in *AIAA/ASME/SAE/ASEE Jt. Propuls. Conf. Exhib. 33rd* AIAA–1997–3052 (1997). at <http://arc.aiaa.org/doi/pdf/10.2514/6.1997-3052>

7. Barral, S. *et al.* On the Origin of Low Frequency Oscillations in Hall Thrusters. *AIP Conf. Proc.* **993,** 439–442 (2008).

8. Fife, J. Hybrid-PIC Modeling and Electrostatic Probe Survey of Hall Thrusters. (1998).

9. Barral, S. & Ahedo, E. Low-frequency model of breathing oscillations in Hall discharges. *Phys. Rev. E* **79,** 046401 (2009).

10. Barral, S. Theoretical Study of the Breathing Mode in Hall Thrusters. 1–12 (2006).

11. Barral, S. & Peradzyński, Z. Ionization oscillations in Hall accelerators. *Phys. Plasmas* **17,** 014505 (2010).

12. Yamamoto, N., Komurasaki, K. & Arakawa, Y. Discharge Current Oscillation in Hall Thrusters. *J. Propuls. Power* **21,** 870–876 (2005).

13. Barral, S., Kaczmarczyk, J., Kurzyna, J. & Dudeck, M. Active Control and Excitation of Breathing Oscillations in a Hall Thruster with a Fast Digital Signal Processor. in *33rd IEPC* (2013).

14. Barral, S., Kaczmarczyk, J., Kurzyna, J. & Dudeck, M. Active Control of a Hall Thruster Discharge. in *32nd IEPC* (2011).

15. Barral, S., Kaczmarczyk, J., Kurzyna, J. & Dudeck, M. Closed-loop control of ionization oscillations in Hall accelerators. *Phys. Plasmas* **18,** 083504 (2011).

16. Barral, S., Miedzik, J. & Ahedo, E. A model for the active control of low frequency oscillations in Hall thrusters. *Proc. 44th Jt. Propuls. ...* (2008). at <http://arc.aiaa.org/doi/pdf/10.2514/6.2008-4632>

17. Hara, K., Sekerak, M. J., Boyd, I. D. & Gallimore, A. D. Mode transition of a Hall thruster discharge plasma. **203304,** (2014).

18. Goebel, D. M. & Katz, I. Fundamentals of Electric Propulsion: Ion and Hall Thrusters. *Fundam. Electr. Propuls. Ion Hall Thrusters* 1–507 (2008). doi:10.1002/9780470436448

19. Raitses, Y., Griswold, M., Ellison, L., Parker, J. & Fisch, N. J. Studies of Rotating Spoke Oscillations in Cylindrical Hall Thrusters. 1–6 (2012).

20. Griswold, M. E., Ellison, C. L., Raitses, Y. & Fisch, N. J. Feedback control of an azimuthal oscillation in the E × B discharge of Hall thrusters. *Phys. Plasmas* **19,** 053506 (2012).

21. Escobar, D. & Ahedo, E. Ionization-induced azimuthal oscillation in Hall Effect. in *IEPC-2011-196* (2011).

22. Liqiu, W. *et al.* Study on breathing mode oscillation suppression of self-excited Hall thrusters. *J. Vac. Sci. Technol. A Vacuum, Surfaces, Film.* **30,** 061304 (2012).

23. Barral, S. A new breath for the breathing mode. 1–8 (2009).

24. Freidberg, J. P. *Plasma Physics and Fusion Energy*. (2007). doi:10.1017/CBO9780511755705

25. Ahedo, E., Gallardo, J. M. & Martínez-Sánchez, M. Effects of the radial plasma-wall interaction on the Hall thruster discharge. *Phys. Plasmas* **10,** 3397 (2003).

26. Sullivan, R. M., Pang, a., Martinez-Sanchez, M. & Whyte, D. G. A lithium depth-marker technique for rapid erosion and deposition measurements. *Nucl. Instruments Methods Phys. Res. Sect. B Beam Interact. with Mater. Atoms* **319,** 79–86 (2014).

27. Nakles, M. R., Brieda, L., Reed, G. D., Hargus Jr, W. a & Spicer, R. L. Experimental and numerical examination of the BHT-200 hall thruster plume. *43rd AIAA/ASME/SAE/ASEE Jt. Propuls. Conf. Exhib.* **3,** 3041–3058 (2007).

28. Boulanger, L. Improvements to a Fully Kinetic Hall Thruster Simulation Code and Characterization of the Cylindrical Cusped Field Thruster. (2014).

29. Ahedo, E., Martínez-Cerezo, P. & Martínez-Sánchez, M. One-dimensional model of the plasma flow in a Hall thruster. *Phys. Plasmas* **8,** 3058 (2001).